# The Vertical Distribution of Atmospheric BrO from Ground-Based Measurements

Robyn Schofield

A thesis submitted in partial fulfilment
of the requirements for the degree of
Doctor of Philosophy in Environmental Science,
The University of Auckland, 2003

# The University of Auckland

## Thesis Consent Form

This thesis may be consulted for the purpose of research or private study provided that due acknowledgement is made where appropriate and that the author's permission is obtained before any material from the thesis is published.

I agree that the University of Auckland Library may make a copy of this thesis for supply to the collection of another prescribed library on request from that Library; and

1. I agree that this thesis may be photocopied for supply to any person in accordance with the provisions of Section 56 of the Copyright Act 1994

Or

2. This thesis may not be photocopied other than to supply a copy for the collection of another prescribed library

(Strike out 1 or 2)

Signed:…….

Date:……

Created: 5 July 2001
Last updated: 9 August 2001

# Abstract

Ground-based UV-Visible measurements targeting BrO were made at Lauder, New Zealand (45.0°S, 169.7°E) and Arrival Heights, Antarctica (77.8°S, 166.7°E). Differential Optical Absorption Spectroscopy (DOAS) was used to determine differential slant column densities (DSCDs) from the radiance measurements. UV-Visible measurements have been made in the two complementary viewing geometries of direct-sun and zenith-sky.

A spherical curved earth single scattering radiative transfer model was developed. The effects of refraction, molecular absorption, Rayleigh and Mie scattering were included. Singularity at the tangent point was avoided and a complete intensity calculation performed. The DSCDs for both the direct-sun and zenith-sky viewing measurements were calculated with this forward model.

A general optimal estimation retrieval algorithm was developed to retrieve altitude information by combining DSCDs from the direct-sun and zenith-sky viewing geometries. A complete retrieval characterisation and error analysis was performed. The characterisation illustrated that tropospheric sensitivity was obtained from the direct-sun viewing measurements, while the zenith-sky measurements were essential for stratospheric sensitivity.

Stratospheric and tropospheric BrO columns were retrieved for the diurnal stages of 80°, 84° and 87° SZA for Lauder. The diurnal and seasonal variation of the stratospheric column was successfully retrieved from the measurements. The stratospheric columns were consistent with a stratospheric $Br_y$ loading of 20 ppt. The tropospheric BrO column retrieved over Lauder was less than 0.9 ppt if a uniform distribution throughout the troposphere is assumed. This is consistent with, though lower than, previous estimates of BrO in the free troposphere of 0.5-2.0 ppt (*Richter et al.*, 2002).

The results of a ten week measurement campaign at Arrival Heights for the spring 2002 are presented. Stratospheric and tropospheric BrO columns were retrieved at 80°, 84° and 88° SZA. A high variability was observed for the retrieved stratospheric columns, due in part to the unusual stratospheric warming in the Antarctic spring 2002 (*Allen et al.*, 2003). A mean ubiquitous tropospheric background of 0.3 ppt was retrieved. Also a 'bromine explosion' event was observed, corresponding to a BrO mixing ratio of 7 ppt for a uniformly mixed boundary layer.

# Acknowledgements

I wish to thank Karin Kreher and Brian Connor for their invaluable supervision, and making this such a great experience for me.

I would also like to thank David Shooter for his guidance and supervision.

I would like to thank all of the staff at the National Institute of Water and Atmospheric research at Lauder. Thanks for all your help. In particular: Paul Johnston and Alan Thomas developed the direct-sun viewing instrument and I owe them many thanks for their patience and helpful guidance. Greg Bodeker for much guidance, help with the radiative transfer and for ozonesonde data over Lauder. Ben Liley for many helpful discussions and for the aerosol extinction profiles over Lauder. Hamish Struthers for the UMETRAC model runs. Jill Scott for all of the computer and technical support. Andrew Matthews for making this possible.

I wish to thank Antarctica NZ and staff at Scott Base for Winfly 2002 for all their support. Sam Oltmans for the surface ozone measurements at Arrival Heights. Thanks also to the Network for the Detection of Stratospheric Change for the Antarctic aerosol and ozonesonde data.

Clive Rodgers for many great discussions and help with retrieval theory.

Udo Frieß, Andreas Richter and François Hendrick for the many useful discussions and data.

I wish to thank the Foundation for Research Science and Technology Bright Future Top Achiever Doctoral Fellowship scheme for providing my funding.

My family and friends (new and old) for their unwavering support.

# Contents

# Figures

# Tables

## Chapter 1

# Introduction

Approximately half of the stratospheric bromine loading is attributable to human activities (*Schauffler et al.*, 1999). Bromine in the radical form bromine monoxide (BrO) plays a key role in stratospheric ozone depletion processes both at mid- and polar latitudes. In the troposphere, very high levels of BrO have been observed in both the polar boundary layer and above salt plains. These high bromine levels in the troposphere have been linked to the biogeochemical cycling of mercury (*Schroeder and Munthe*, 1998). Quantifying the altitude distribution of BrO is important due to the very different implications that this species has for the troposphere relative to the stratosphere.

Retrieval of the altitude distribution of trace gas species from UV-visible spectroscopic measurements was first attempted by *Brewer et al.* (1973) for $NO_2$. *Brewer et al.*, and later *Noxon* (1975) performed simple analyses to infer stratospheric and tropospheric $NO_2$ concentrations from measurements of the differential slant column density (DSCD - defined in section 5.6.1). *McKenzie et al.* (1991) performed a formal retrieval of $O_3$ and $NO_2$ profiles using zenith-sky DSCDs with no error treatment or characterisation in terms of resolution or information content. *Preston et al.* (1997) implemented *Rodgers* (1990) optimal estimation technique to retrieve $NO_x$ ($NO_2$+NO) profiles (and subsequently $NO_2$ profiles using a chemical box model) from zenith-sky $NO_2$ DSCD measurements with a complete error and sensitivity analysis. By retrieving $NO_x$ profiles *Preston* (1995) avoided a state vector that varied with time ($NO_2$ profiles have a strong diurnal variation).

The variation of trace gas profiles with time, typical of diurnally varying species, causes complication in the 'profile' retrieval from DSCDs. The complication arises due to the measurements being made over an extended time period during which the trace gas profile is changing. The highest sensitivity to altitude is obtained using twilight spectra. However, this is also when the photochemistry is changing most rapidly. *Livesey and Read* (2000) detail the use of the optimal estimation technique in retrieving temperature and composition profiles along the line of sight of limb sounding satellite measurements. More recently, the concept of retrieving the 'horizontal gradient' has been developed by *Kemnitzer et al.* (2002), also for the retrieval from limb sounding satellite measurements. A similar concept is applied here to retrieve a set of profiles at different diurnal stages concurrently from the DSCD measurements.

The concept of combining complementary measurements in a formal retrieval was developed for ozone using the Huggins bands by *Jiang et al.* (1997) in a theoretical study. Jiang *et al.*, found combining direct and diffuse measurements had the potential to be an effective technique to retrieve the tropospheric and stratospheric ozone column amounts. In this study, the advantages of combining the two spectroscopic viewing geometries of 'direct-sun' and 'zenith-sky', to give tropospheric and stratospheric sensitivity, are investigated.

The retrieval of DSCDs from the radiance measurements using Differential Optical Absorption Spectroscopy (DOAS - defined in section 4.3) is decoupled from the subsequent retrieval of the altitude distribution. It is this latter retrieval that is explored in this thesis to illustrate how different measurement platforms can be combined to provide altitude distribution on a temporal scale for BrO trace gas concentrations. This retrieval method can be adapted to use any spectroscopically derived quantity (SCD or DSCD) or the radiance measurements directly. This retrieval method has the advantage that it may be extended to include many measurement platforms.

## Chapter 2

# Stratospheric Chemistry

This Chapter discusses the chemistry of the stratosphere with a focus on ozone depletion. Catalytic ozone depletion cycles of hydrogen, nitrogen, chlorine and bromine are outlined in the homogeneous chemistry section. The role of polar stratospheric clouds and sulfate aerosols are discussed. These provide the surfaces for the heterogeneous processes that lead to ozone losses at polar and mid-latitudes. At polar latitudes chlorine heterogeneous processes recycle chlorine from its reservoir forms, leading to severe ozone losses via homogeneous reactions. At mid-latitudes the heterogeneous processes of bromine and nitrogen have consequences for ozone. Homogeneous reactions involving chlorine and bromine are responsible for most of the polar, and about half of the mid-latitude ozone depletion. Stratospheric sources and loadings of inorganic bromine are also discussed.

## 2.1 Stratospheric Ozone

Ozone was discovered by Schönbein in 1839. Ozone, so named for its pungent smell (ozien is Greek for 'to smell'), is the characteristic smell around photocopying equipment and is probably the youngest gaseous member of the natural atmosphere. The primitive atmosphere (more than four billion years ago) consisted only of carbon dioxide ($CO_2$), nitrogen ($N_2$) and water ($H_2O$) due to out-gassing of the earth's mantle. The emergence of green plant photosynthesis two billion years later in the oceans led to oxygen ($O_2$) production and hence ozone ($O_3$) in our atmosphere. It is the ability of ozone to filter damaging ultraviolet (UV) radiation that enabled the evolution of higher forms of cellular life (*Fraser*, 1997).

UV radiation at wavelengths ($\lambda$) less than 290 nanometers (nm) is detrimental to protein and nucleic acid molecules. Major components of the atmosphere, primarily $O_2$, absorb wavelengths less than 230 nm. Ozone is the only atmospheric species able to attenuate UV at wavelengths greater than 230 nm. It does so with such efficiency that at 250 nm only 1 part in 1030 of the incident UV is transmitted (*Wayne*, 1991). Ozone is responsible for the attenuation of UV not only in the vital UV-C range between 230 - 280 nm but also, to a lesser degree, UV-B (radiation in the range 280 - 315 nm). Increased UV-B radiation is associated with an increased incidence and morbidity due to skin cancer, eye and infectious diseases as well as impeding growth of plants in both terrestrial and

aquatic environments (*Van der Leun et al.*, 1995).

The majority of ozone is located in the stratosphere (∼90 %) in a layer ∼20 km thick with peak mixing ratios at an altitude of 10 - 30 km of 6 (polar) and 10 (equatorial) parts per million (ppm) (*Fraser*, 1997). The total column ozone amounts vary from 250 (equatorial) to 450 (polar) Dobson Units ($1\,\mathrm{DU} = 2.7 \times 10^{16}\,\mathrm{molecules.cm^{-2}}$). This is due to the peak mixing ratios in the polar regions occurring at lower altitudes where the increased pressure corresponds to increased molecule numbers.

It is the residence of ozone in the stratosphere that is primarily responsible for the dynamic stability of the stratosphere. The ozone absorption of UV radiation generates heat resulting in a positive temperature gradient throughout the stratosphere with a maximum temperature at an altitude of ∼50 km (*Fraser*, 1997).

Ozone measurements have been made since the beginning of the 20th century (*Dobson*, 1968; *Staehelin et al.*, 1998a,b, and references therein). These long observation records have shown that global ozone has decreased significantly since 1980 (*Solomon*, 1999b; *Bodeker et al.*, 2001), more than is expected due to seasonal, annual and latitudinal variability.

### 2.1.1 The Antarctic Ozone Hole

The discovery of severe springtime ozone depletion over Antarctica, coined as the 'ozone hole', was made in 1985 at Halley Bay by *Farman et al.* (1985). These large polar ozone losses were unexpected given the current understanding of stratospheric chemistry. At the time chlorine chemistry was predicted to produce significant ozone depletion between 35 - 45 km at low to mid-latitudes (*Fraser*, 1997).

Essentially no photodissociation of molecular oxygen occurs in the winter polar stratosphere due to the low UV intensities during this time. Catalytic ozone depletion cycles involving atomic oxygen, such as the cycles involving nitrogen, become insignificant. However, radical ozone destruction cycles involving halogen species that occur without atomic oxygen dominate. Homogeneous chemistry alone cannot explain the severe ozone losses seen in the polar regions. It is now widely accepted that significant ozone polar losses are sustained by the regeneration of active chlorine and to a lesser extent, bromine radicals, from their reservoir species. Heterogeneous reactions on the surface of polar stratospheric clouds (PSCs) and aerosols facilitate the large ozone losses in the polar spring stratosphere (*Solomon*, 1999a).

## 2.2 Stratospheric Bromine Source

A variety of organic bromine-containing trace gases of both anthropogenic and natural origin contribute to the stratospheric bromine budget. About 52 % of the current

bromine loading of the stratosphere is attributable to human activities (*Schauffler et al.*, 1999; *Wamsley et al.*, 1998). Methyl bromide is the primary source of bromine to the stratosphere (55 - 60 %) (*Schauffler et al.*, 1998) and has both natural and anthropogenic sources. Methyl bromide is produced industrially for use in produce, space and soil fumigation (*Kourtidis et al.*, 1998). Other anthropogenic sources include burning of leaded gasoline and biomass burning. Natural sources include biomass emissions from the oceans of algae, phytoplankton and macroalgae (*Schauffler et al.*, 1999, and references therein).

The halons are the second largest source of stratospheric bromine (comprising **∼38 % of the organic bromine** at the tropopause (*Schauffler et al.*, 1999)). The halon nomenclature is $C_aF_bCl_cBr_d$ where abcd is the number assigned to the identification of the halon (i.e. halon-1211 describes the molecule $CF_2ClBr$) (*O'Sullivan*, 1989). Halons are used as fire extinguishing material where water is inappropriate, such as for electrical fires. Halon production has been prohibited in developed countries since 1994 (*WMO*, 2003). In developing countries the continued manufacture of halons is permitted but is to be held at 1995 - 1997 production levels after 2002. Halons will continue to be an important source of stratospheric bromine over the next few decades (*Butler et al.*, 1998).

A discrepancy was highlighted by *Wamsley et al.* (1998) that the reactive bromine ($Br_y$) derived from long-lived organic tropospheric sources fell short of the reactive bromine concentration inferred from inorganic BrO measurements of the lower stratosphere. The combined input of halons and methyl bromide was found to account for only $16 \pm 2$ ppt at 20 - 25 km with the total reactive bromine mixing ratio inferred from BrO measurements at this altitude range being reported to be $20 \pm 2.5$ ppt (*Harder et al.*, 2000). While the errors do overlap, there is a significant difference in the implications of bromine loadings of 16 ppt compared to 20 ppt, for ozone losses. Dibromomethane ($CH_2Br_2$) and bromoform ($CHBr_3$) are now considered to contribute up to 3 ppt to the total stratospheric bromine loading (*Wamsley et al.*, 1998; *Sturges et al.*, 2000; *Pfeilsticker et al.*, 2000). The additional source required to explain the remaining difference of ∼1 ppt is as yet unknown (*WMO*, 2003).

## 2.3 Stratospheric Homogeneous Chemistry

The steady-state ozone concentration in the stratosphere was proposed to be maintained by the oxygen-only reactions described by Sir Sydney Chapman (*Chapman*, 1930). Odd-oxygen $O_x$ describes the reactive oxygen species, where $O_x = O_3 + O$. Throughout most of the stratosphere ozone completely dominates the odd-oxygen species such that $O_x = O_3$ (*Lee et al.*, 2002).

$O_x$ Reactions:

$$O_2 \xrightarrow{h\nu} 2O \quad (\lambda < 242\,\text{nm}) \tag{2.1}$$

$$O_2 + O \xrightarrow{M} O_3 \tag{2.2}$$

$$O_3 \xrightarrow{h\nu} O + O_2 \tag{2.3}$$

$$O + O \xrightarrow{M} O_2 \tag{2.4}$$

$$O + O_3 \longrightarrow 2O_2 \tag{2.5}$$

Reactions 2.2 - 2.3 rapidly interconvert the odd-oxygen species O and $O_3$. The loss reactions of O and $O_3$ (given by reactions 2.4 and 2.5) as longer lived $O_2$ occur at slower rates.

Kinetic experiments conducted in the 1960s by *Schiff* (1969) demonstrated that observed levels of $O_3$ were inconsistent with levels predicted from reactions 2.1 - 2.5. Since then, the catalytic ozone destruction cycles involving hydrogen, nitrogen, and the halogen species of chlorine and bromine have been proposed to explain observed ozone levels. The other halogens, fluorine and iodine, are not considered to have important roles in stratospheric ozone losses. Fluorine is removed rapidly from its radical form. The fluorine reservoir HF is a strongly bound, unreactive molecule, unable to participate in ozone loss mechanisms. Iodine, though thought to be quite reactive towards ozone (*Solomon et al.*, 1994), occurs in the stratosphere with such low abundances that it is not considered to contribute to stratospheric ozone depletion.

### 2.3.1 Homogeneous Hydrogen Chemistry

*Bates and Nicolet* (1950) proposed the involvement of hydrogen in catalytic ozone depletion cycles to explain observed ozone levels. The reactive hydrogen species of H, $H_2O_2$, OH and $HO_2$ are denoted with the generic term $HO_x$. Catalytic ozone destruction cycles involving $HO_x$ dominate ozone losses below 20 km. Above this altitude their role decreases and at 30 km they are considered only minor stratospheric ozone loss processes (*Fraser*, 1997). Heterogeneous reactions of nitrogen and bromine at mid-latitudes cause increased $HO_x$ levels. Of the total ozone losses in the lower stratosphere at southern mid-latitudes 30 % result from the following reaction cycle (*Lee et al.*, 2002).

$HO_x$ Cycle:

$$\begin{aligned} OH + O &\longrightarrow HO_2 && (2.6)\\ HO_2 + O &\longrightarrow OH + O_2 && (2.7)\\ OH + O_3 &\longrightarrow HO_2 + O_2 && (2.8)\\ HO_2 + O_3 &\longrightarrow OH + 2O_2 && (2.9)\\ \hline \text{Net :}\quad 2O + 2O_3 &\longrightarrow 4O_2 \end{aligned}$$

The reaction of atomic oxygen with water and methane is the major source of the hydroxyl radical (OH) in the stratosphere. As approximately half of the water in the upper stratosphere is due to the multi-step oxidation of methane, methane levels in the stratosphere are vital in the determination of hydroxyl radical levels (*Fraser*, 1997). Maximum methane levels are observed in the tropical stratosphere due to strong convection processes occurring at the tropics (*Jones and Pyle*, 1984).

The major sink processes for the hydroxyl radical are the reaction with $HO_2$ and with nitric ($HNO_3$) and hydrochloric (HCl) acids:

$$\begin{aligned} OH + HO_2 &\longrightarrow O_2 + H_2O && (2.10)\\ OH + HNO_3 &\longrightarrow NO_3 + H_2O && (2.11)\\ OH + HCl &\longrightarrow Cl + H_2O && (2.12) \end{aligned}$$

### 2.3.2 Homogeneous Nitrogen Chemistry

The role of nitrogen in stratospheric ozone depletion was proposed by *Crutzen* (1970, 1971). Catalytic ozone destruction cycles involving reactive nitrogen ($NO_x$=$NO_2$+NO) dominate ozone depletion in the upper stratosphere:

$NO_x$ Cycle 1:

$$\begin{aligned} NO + O_3 &\longrightarrow NO_2 + O_2 && (2.13)\\ NO_2 + O &\longrightarrow NO + O_2 && (2.14)\\ \hline \text{Net :}\quad O_3 + O &\longrightarrow 2O_2 \end{aligned}$$

$NO_x$ Cycle 2:

$$\begin{aligned} NO + O_3 &\longrightarrow NO_2 + O_2 \\ NO_2 + O_3 &\longrightarrow NO_3 + O_2 \quad (2.15) \\ NO_3 &\xrightarrow{h\nu} NO + O_2 \quad (2.16) \\ \hline \text{Net :} \quad 2O_3 &\longrightarrow 3O_2 \end{aligned}$$

$NO_3$ combines with $NO_2$ to form $N_2O_5$, which has consequences for heterogeneous chemistry (see equation 2.50). $N_2O_5$ undergoes photolysis regenerating the $NO_x$ species:

$$NO_2 + NO_3 \longrightarrow N_2O_5 \quad (2.17)$$

$$N_2O_5 \xrightarrow{h\nu} NO_2 + NO_3 \quad (2.18)$$

Nitrous oxide ($N_2O$) is the major source of reactive nitrogen in the stratosphere. Tropospheric $N_2O$ is produced by denitrifying and nitrifying soil bacteria (*Fraser*, 1997). $N_2O$ is delivered to the stratosphere from the troposphere via tropical convection. Stratospheric nitric oxide (NO) is formed primarily via the reaction of atomic oxygen with $N_2O$:

$$O + N_2O \longrightarrow 2NO \quad (2.19)$$

Other sources contributing to the stratospheric $NO_x$ budget include tropospheric lightning induced NO, and cosmic ray and proton production (*WMO*, 2003).

The major removal process for stratospheric $NO_x$ is via the formation of nitric acid:

$$NO_2 + OH \longrightarrow HNO_3 \quad (2.20)$$

Nitric acid is the longest-lived stratospheric nitrogen species. Sedimentation processes in the polar regions are a major sink for stratospheric nitrogen (see section 2.4.1). The OH radical is involved in both the formation of $HNO_3$, as well as its destruction (see reaction 2.11). $HNO_3$ concentrations are largely dependent on OH concentrations. Photolysis of $HNO_3$ is slow with an atmospheric lifetime of ∼1 month in the lower stratosphere.

$$HNO_3 \xrightarrow{h\nu} NO_2 + OH \quad (2.21)$$

### 2.3.3 Homogeneous Chlorine Chemistry

Around 85 % of stratospheric inorganic chlorine burden ($Cl_y$) in 1992 was attributable to human activities (*Montzka et al.*, 1996; *Schauffler et al.*, 1993). Chlorofluorocarbons (CFCs) are responsible for the release of radical chlorine species ($ClO_x$) into the strato-

sphere via photodissociation as identified by *Molina and Rowland* (1974). ClO has a peak abundance at ∼40 km at mid-latitudes in unperturbed conditions. This led to the prediction that the effect of CFCs on ozone concentrations would be most evident at this altitude (*Molina and Rowland*, 1974) due to the following catalytic cycles:

$ClO_x$ Cycle 1:

$$\begin{aligned} Cl + O_3 &\longrightarrow ClO + O_2 \quad (2.22)\\ ClO + O &\longrightarrow Cl + O_2 \quad (2.23)\\ \hline \text{Net :}\quad O_3 + O &\longrightarrow 2O_2 \end{aligned}$$

$ClO_x$ Cycle 2:

$$\begin{aligned} ClO + HO_2 &\longrightarrow HOCl + O_2 \quad (2.24)\\ HOCl &\xrightarrow{h\nu} OH + Cl \quad (2.25)\\ Cl + O_3 &\longrightarrow ClO + O_2\\ OH + O_3 &\longrightarrow HO_2 + O_2\\ \hline \text{Net :}\quad 2O_3 &\longrightarrow 3O_2 \end{aligned}$$

$ClO_x$ cycles 1 and 2 are responsible respectively for about 11 % and 8 % of southern mid-latitude ozone losses (*Lee et al.*, 2002). Heterogeneous chemistry (see section 2.4.4) in the polar springtime causes perturbations in the ClO profile and an additional, more significant, peak abundance is observed at 20 km. In the perturbed polar springtime stratosphere, the $ClO_x$ cycles 1 and 2 are thought to be each responsible for ∼5 % of the observed ozone losses (*Anderson et al.*, 1991; *Finlayson-Pitts and Pitts*, 1999; *Lee et al.*, 2002).

Under perturbed polar conditions the dimerisation of ClO facilitates the large ozone losses observed in the formation of the ozone hole. The dimerisation of ClO is important for the regeneration of Cl in environments where UV levels and thus O concentrations are very small (*Molina et al.*, 1987; *Wahner et al.*, 1989; *Solomon et al.*, 1989):

$ClO_x$ Cycle 3:

$$
\begin{aligned}
2 \times (Cl + O_3 &\longrightarrow ClO + O_2) \\
ClO + ClO &\xrightarrow{M} (ClO)_2 && (2.26)\\
(ClO)_2 &\xrightarrow{h\nu} Cl + ClOO && (2.27)\\
ClOO &\xrightarrow{M} Cl + O_2 && (2.28)\\
\hline
\text{Net :} \quad 2O_3 &\longrightarrow 3O_2
\end{aligned}
$$

It is this termolecular ClO dimer reaction cycle that is responsible for about 40 % of the ozone losses between 13 - 18 km in the Antarctic springtime contributing to the 'ozone hole' formation (*Lee et al.*, 2002). Other pathways for the dimer reaction exist, producing $Cl_2$ and OClO. However, due to large activation barriers, these pathways are considered insignificant (*Nickolaisen et al.*, 1994; *Finlayson-Pitts and Pitts*, 1999).

The major stratospheric reservoir species for chlorine are $ClONO_2$ and HCl. $ClONO_2$ and HCl are produced by the reaction of nitrogen dioxide and methane with ClO **and Cl respectively**. Due to the stability of these reservoir species they dominate the reactive stratospheric chlorine budget:

$$
\begin{aligned}
ClO + NO_2 &\longrightarrow ClONO_2 && (2.29)\\
Cl + CH_4 &\longrightarrow HCl + CH_3 && (2.30)
\end{aligned}
$$

Radical regeneration from the reservoir species is necessary to maintain the catalytic ozone destruction. This $ClO_x$ regeneration is slow in the gas phase:

$$
\begin{aligned}
ClONO_2 &\xrightarrow{h\nu} ClO + NO_2 && (2.31)\\
HCl + OH &\longrightarrow Cl + H_2O
\end{aligned}
$$

The partitioning of $HCl/Cl_y$ and $ClONO_2/Cl_y$ strongly influences the effectiveness of one chlorine atom to destroy ozone via catalytic cycles (*Solomon*, 1999b). HCl is the longest lived chlorine species typically with a lifetime of over a week, and constitutes the largest fraction of $Cl_y$ in the lower stratosphere. The $Cl_y$ loss process from the stratosphere is slow, with chlorine being lost to the troposphere primarily as HCl.

### 2.3.4 Homogeneous Bromine Chemistry

Bromine is more reactive towards ozone than chlorine though its abundance is 200 times less (*Schauffler et al.*, 1993; *Wamsley et al.*, 1998). The efficiency of a bromine atom in destroying ozone is estimated to be 45 times that of a chlorine atom (*Danilin et al.*, 1996;

*Daniel et al.*, 1999). This higher reactivity is attributable to bromine forming weaker bonds than chlorine. The resultant partitioning between radical ($BrO_x$) and reservoir species favours the reactive radical forms of Br and BrO. In the mid-latitude lower stratosphere ∼50 % of the reactive bromine ($Br_y$) resides as BrO and ∼50 % as $BrONO_2$ during the day (*Fish et al.*, 1995; *Sinnhuber et al.*, 2002).

The following ozone depletion cycles involving bromine were proposed by *Wofsy et al.* (1975) and *Yung et al.* (1980). The ozone depletion cycle of BrO with odd-oxygen is less significant than its chlorine analogue (*Lary*, 1997):

$BrO_x$ Cycle 1:

$$\begin{aligned} Br + O_3 &\longrightarrow BrO + O_2 \quad (2.32)\\ BrO + O &\longrightarrow Br + O_2 \quad (2.33)\\ \hline \text{Net :}\quad O_3 + O &\longrightarrow 2O_2 \end{aligned}$$

The most important ozone destruction catalytic cycle for bromine in the lower stratosphere is that which involves coupling with the chlorine cycle (*Lary and Toumi*, 1997). At southern mid-latitudes this reaction is the most important halogen ozone loss cycle. At polar latitudes this reaction cycle equals the ozone losses seen with the chlorine dimer reaction cycle. Together these cycles account for 80 % of the ozone losses that lead to the formation of the Antarctic ozone hole (*Lee et al.*, 2002). The ClO+BrO catalytic cycle involves the formation of ClOO or BrCl:

$BrO_x$ Cycle 2:

$$\begin{aligned} BrO + ClO &\longrightarrow Br + ClOO \quad (2.34)\\ ClOO &\xrightarrow{M} Cl + O_2\\ Cl + O_3 &\longrightarrow ClO + O_2\\ Br + O_3 &\longrightarrow BrO + O_2\\ \hline \text{Net :}\quad 2O_3 &\longrightarrow 3O_2 \end{aligned}$$

This cycle occurs with an rate of $2.3 \times 10^{-12} e^{\frac{260}{T}}$ (*Sander et al.*, 2000) giving a yield of (34%) for the BrO+ClO reaction at 200 K. Two other possible reaction pathways with their respective yields and rates are:

$$BrO + ClO \longrightarrow Br + OClO \quad \left(k = 9.5 \times 10^{-13} e^{\frac{550}{T}}\right) (59\%) \quad (2.35)$$

$$BrO + ClO \longrightarrow BrCl + O_2 \quad \left(k = 4.1 \times 10^{-13} e^{\frac{290}{T}}\right) (7\%) \quad (2.36)$$

The formation of OClO, though the pathway giving the largest yield, is a null reaction as its photolytic products are ClO+O, thus regenerating odd oxygen. Reaction 2.35 is the only significant formation process for OClO (though one of the minor pathways of the ClO self reaction also forms OClO) and this is used as an qualitative indicator species for chlorine activation (*Miller et al.*, 1999). The reaction 2.35 pathway becomes most significant at low temperatures. BrCl photolyses readily to give Br and Cl, which then participate in further catalytic cycles.

$$\mathrm{BrCl} \xrightarrow{h\nu} \mathrm{Br} + \mathrm{Cl} \tag{2.37}$$

$$\tag{2.38}$$

In analogy to the chlorine dimerisation (see reactions 2.26 - 2.28), bromine is capable of undergoing similar reactions:

$$\begin{aligned} \mathrm{BrO} + \mathrm{BrO} &\xrightarrow{M} (\mathrm{BrO})_2 && (2.39)\\ &\longrightarrow \mathrm{Br}_2 + \mathrm{O}_2 && (2.40)\\ &\longrightarrow 2\mathrm{Br} + \mathrm{O}_2 && (2.41) \end{aligned}$$

Due to the relatively small BrO concentrations, the BrO self-reaction is not considered to be of importance.

Coupling of the $BrO_x$ and $HO_x$ cycles provides another important ozone depletion cycle (*Lary*, 1997). The BrO+$HO_2$ is most important at mid-latiudes accounting for 5 % of ozone losses in the lower stratosphere, slightly lower than its chlorine analogue (*Lee et al.*, 2002).

$BrO_x$ Cycle 3:

$$\begin{aligned} \mathrm{BrO} + \mathrm{HO}_2 &\longrightarrow \mathrm{HOBr} + \mathrm{O}_2 && (2.42)\\ \mathrm{HOBr} &\xrightarrow{h\nu} \mathrm{OH} + \mathrm{Br} && (2.43)\\ \mathrm{Br} + \mathrm{O}_3 &\longrightarrow \mathrm{BrO} + \mathrm{O}_2 \\ \mathrm{OH} + \mathrm{O}_3 &\longrightarrow \mathrm{HO}_2 + \mathrm{O}_2 \\ \hline \text{Net :} \quad 2\mathrm{O}_3 &\longrightarrow 3\mathrm{O}_2 \end{aligned}$$

Bromine can react with nitrogen in a catalytic ozone depletion cycle. Unlike the tightly bound analogous chlorine reservoir species, $BrONO_2$ is more rapidly photolyzed (*Lary*, 1996). The following ozone destroying catalytic cycle involving BrO and $NO_2$ is only a minor lower stratospheric ozone loss process:

$BrO_x$ Cycle 4:

$$BrO + NO_2 \xrightarrow{M} BrONO_2 \quad (2.44)$$

$$BrONO_2 \xrightarrow{h\nu} Br + NO_3 \quad (2.45)$$

$$NO_3 \xrightarrow{h\nu} NO + O_2$$

$$NO + O_3 \longrightarrow NO_2 + O_2$$

$$Br + O_3 \longrightarrow BrO + O_2$$

$$\text{Net :} \quad 2O_3 \longrightarrow 3O_2$$

$BrONO_2$ is the major daytime reservoir species constituting about half of total stratospheric $Br_y$. At twilight BrO is converted to $BrONO_2$, BrOH and to BrCl (this species dominates at low temperatures), which form the main nighttime reservoir species for bromine.

Stratospheric bromine is formed via the reaction of the tropospheric sources (see section 2.2) with either the hydroxyl radical or excited atomic oxygen, i.e. for methyl bromide:

$$CH_3Br + OH \xrightarrow{M} BrOH \quad (2.46)$$

$$CH_3Br + O \xrightarrow{h\nu} BrO \quad (2.47)$$

HBr is the longest-lived bromine species with a lifetime of ∼1 day at mid-latitudes in the lower stratosphere (*Lary et al.*, 1996). HBr is only a weakly bound molecule and not a stable reservoir species (compare with the chlorine analogue HCl lifetime of ∼1 week). HBr is formed via reactions of Br with $HO_2$ and formaldehyde (HCHO):

$$Br + HO_2 \longrightarrow HBr + O_2 \quad (2.48)$$

$$Br + HCHO \longrightarrow HBr + CHO \quad (2.49)$$

The abundance of HBr is low due to the reaction of Br with $HO_2$ being largely negligible throughout the stratosphere (*Mellouki et al.*, 1994; *Fish and Jones*, 1995). The removal of bromine from the stratosphere is as yet not well established but expected to be via mixing at the tropopause, thus the most abundant bromine species will make the largest contribution to reactive bromine losses.

OBrO has recently been tentatively observed as a nighttime reservoir for bromine (*Renard et al.*, 1998). This is inconsistent with the current chemical understanding with the only known gas-phase formation reaction of OBrO having a very slow rate (*Erle et al.*, 2000; *Chipperfield et al.*, 1998).

## 2.4 Stratospheric Heterogeneous Chemistry

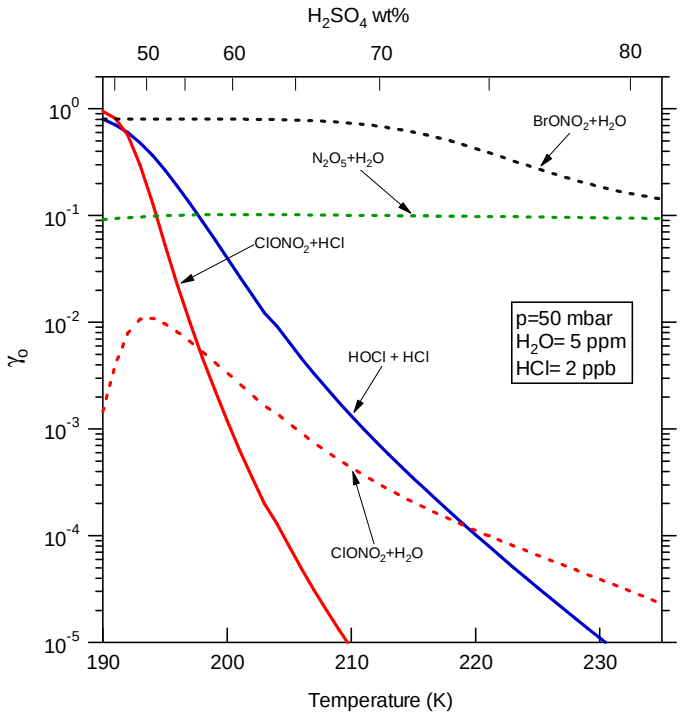


**Figure 2.1**: Recommended reactive uptake coefficients as a function of temperature for key stratospheric heterogeneous reactions on sulfuric acid aerosols. Taken from *Sander et al.* (2000).

It is the reactions occurring on the surfaces of polar stratospheric clouds and sulfate aerosols that are primarily linked to the dramatic ozone losses seen in the lower stratosphere. Figure 2.1 illustrates clearly the importance of the hydrolysis of both $N_2O_5$ and $BrONO_2$ at all temperatures. The reactions involving chlorine are notably more significant at lower temperatures. Heterogeneous reactions of nitrogen and bromine elevate $HO_x$ levels and thus contribute to the $HO_x$ homogeneous reactions which dominate mid-latitude ozone losses. $ClO_x$ and $BrO_x$ homogeneous reactions dominate polar ozone losses as a result of the heterogeneous reactions of chlorine.

### 2.4.1 Polar Stratospheric Clouds (PSCs)

Iridescent or nacreous clouds that form in the winter stratosphere of the polar regions play a critical role in the severe springtime ozone depletion observed over Antarctica (*Solomon*, 1999b; *Tie and Brasseur*, 1995, 1996). PSCs form at cold temperatures below ~195 K, at altitudes between ~12 - 25 km and persist in the Antarctic stratosphere from June - September (*McCormick et al.*, 1982). There are essentially two types of PSC, Type II being usually associated with the colder, more stable polar vortex of Antarctic winters (discussed in more detail below).

Sulfate aerosols provide nuclei for the formation of PSCs. As the stratosphere cools in the polar regions, the stratospheric sulfate aerosols (SSA) absorb both gaseous water and nitric acid, forming ternary $H_2SO_4 - H_2O - HNO_3$ solutions. Continued water and nitric acid absorption from additional cooling can dilute the $H_2SO_4$ concentration to the extent that essentially the solution is a $HNO_3 - H_2O$ mixture. Freezing out of nitric acid trihydrate (NAT) (*Molina et al.*, 1993; *Iraci et al.*, 1994, 1995) and/or nitric acid dihydrate (NAD) (*Tisdale et al.*, 1997) ensues. These PSCs that contain large amounts of $HNO_3$ and water, are known as Type I PSCs. Type Ia refers to the PSCs containing solid hydrates of nitric acid, while in type Ib the nitric acid is in the liquid ternary solution with water and sulfuric acid (*Anthony et al.*, 1997). Type I PSCs form below ∼195 K (*WMO*, 2003). There is still research continuing in this area with the possibility that Type Ia PSCs only form below the ice frost point (*Anthony et al.*, 1997). The ice frost point is ∼188 K for stratospheric temperatures and pressures.

Type II PSCs are formed when the temperature reaches and falls below the ice frost point. The condensed water (ice) forms large particles which due to their size have a large settling rate of $\sim 1\,\mathrm{km\,day^{-1}}$. These PSCs are mainly composed of ice, though an appreciable amount of $HNO_3$ is also contained within them, and thus is also removed via sedimentation to lower altitudes (lower stratosphere and troposphere) (*Finlayson-Pitts and Pitts*, 1999). Denitrification and dehydration of the stratosphere results (*Hintsa et al.*, 1998). Water is more than 100 times more abundant than reactive nitrogen. The reactive nitrogen ($NO_y$) will preferentially condense, thus denitrification has been observed with little dehydration, though this is an area of some debate (*Solomon*, 1999b). Denitrification is dependent on particle size and occurs through sedimentation of large NAT particles (Type Ia or Type II). Denitrification is observed in the Antarctic allowing the reactive chlorine to be partitioned in the radical forms instead of the reservoir species $ClONO_2$. *This has serious implications for ozone as total nitrogen removal via Type II PSC formation and sedimentation alters the partitioning between active and reservoir halogen species.*

### 2.4.2 Aerosols

Sulfate forms a layer in the stratosphere known as the Junge layer (*Junge et al.*, 1961). The maximum sulfate density coincides with the maximum ozone density between 15 - 20 km (*Fraser*, 1997). Stratospheric sulfate aerosols (SSAs) provide a surface for important heterogeneous reactions at both mid-latitudes and polar regions. The major source of sulfur to the stratosphere is carbonyl sulfide (COS) in unperturbed conditions, which undergoes oxidation to sulfuric acid (*Crutzen*, 1976; *Kourtidis et al.*, 1995). Large volcanic eruptions inject huge quantities of $SO_2$ into the stratosphere, increasing the number

density of SSAs by 1 - 2 orders of magnitude (*Russell et al.*, 1996; *Solomon*, 1999b). Under volcanically perturbed aerosol loadings the effects of heterogeneous nitrogen and bromine reactions have detrimental consequences for ozone at all latitudes and all seasons (*Danilin and McConnell*, 1995; *Tie and Brasseur*, 1995, 1996; *Fahey et al.*, 1993; *Chartrand and McConnell*, 1999).

### 2.4.3 Heterogeneous Nitrogen Chemistry

The hydrolysis of $N_2O_5$ is instrumental in denoxifying the lower stratosphere. Denoxifying is the removal of reactive $NO_x$ species, and a temporary process compared to denitrification, which is the permanent removal of reactive nitrogen ($NO_y$) species (*Chartrand and McConnell*, 1999; *Danilin and McConnell*, 1995; *Hendricks et al.*, 1999). The removal of $NO_x$ by this heterogeneous nitrogen reaction alters the partitioning of chlorine species between radical and reservoir species. Lower $NO_x$ levels result in increased $ClO_x$ levels (refer to equations 2.29 and 2.31). This heterogeneous reaction is essentially independent of temperature. Thus, it is considered to be important at all latitudes:

$$N_2O_5 + H_2O_{(l)} \longrightarrow 2HNO_3 \tag{2.50}$$

The subscripts (l) and (s) (below) refer respectively to the liquid and solid phases of the chemical species. No subscript means the species is in the gaseous phase. nitric acid/nitrous acid???

### 2.4.4 Heterogeneous Chlorine Chemistry

The relative stability of the chlorine reservoir species with respect to the active chlorine species Cl and ClO means that most of the stratospheric inorganic chlorine exists as HCl and $ClONO_2$. HCl is effectively absorbed on ice (Type II PSC) and NAT (Type Ib PSCs) solid phase surfaces, the efficiency being determined by various factors including temperature and the partial pressure of HCl (*Finlayson-Pitts and Pitts*, 1999). A possible mechanism is the efficient ionisation of HCl onto the ice surface. The following heterogeneous processes have the greatest consequences for ozone depletion in the springtime polar regions (*Solomon*, 1999b).

$$ClONO_2 + HCl_{(s)} \longrightarrow Cl_2 + HNO_{3(s)} \tag{2.51}$$

$$N_2O_5 + HCl_{(s)} \longrightarrow ClNO_2 + HNO_{3(s)} \tag{2.52}$$

The photoactive species $Cl_2$ and $ClNO_2$ are formed, which photolyse to produce active Cl with the polar sunrise. The second process is a null reaction. When $ClNO_2$ undergoes photolysis $NO_2$ is released, which is able to recombine with ClO to reform the reservoir

species $ClONO_2$. The low atomic oxygen concentrations associated with low UV levels in the polar winter/spring force changes in the gas-phase chlorine chemistry relative to mid-latitudes. Cl is only able to be reformed from ClO via dimerisation ($ClO_x$ cycle 3 reactions 2.26 - 2.28) (*Molina et al.*, 1987).

The severe denitrification of the polar stratosphere occurs due to Type II PSC formation (refer to section 2.4.1 above). Denitrification enables chlorine radicals to complete many catalytic ozone destruction cycles without being converted into the reservoir species $ClONO_2$. It is the heterogeneous chlorine chemistry and following gas-phase destruction cycles that are fundamentally responsible for large ozone losses seen over Antarctica in springtime. The dimerisation of ClO and the ClO+BrO reactions (refer to $ClO_x$ cycle 3 and $BrO_x$ cycle 2 respectively) account for 80 % of the Antarctic lower stratospheric ozone losses (*Lee et al.*, 2002).

### 2.4.5 Heterogeneous Bromine Chemistry

Unlike the chlorine chemistry, the partitioning of bromine ($Br_y$) in the stratosphere favours the active bromine forms, BrO and Br; thus $BrO_x$ species are relatively abundant even in the absence of heterogeneous chemistry (*Hendricks et al.*, 1999). The most important heterogeneous bromine reactions on PSCs are those, which are mixed halogen in nature (*Lary et al.*, 1996):

$$HOBr + HCl_{(s)} \longrightarrow BrCl + H_2O_{(s)} \quad (2.53)$$

$$BrONO_2 + HCl_{(s)} \longrightarrow BrCl + HNO_{3(s)} \quad (2.54)$$

$$HOCl + HBr_{(s)} \longrightarrow BrCl + H_2O_{(s)} \quad (2.55)$$

$$ClONO_2 + HBr_{(s)} \longrightarrow BrCl + HNO_{3(s)} \quad (2.56)$$

The solubility of HCl in SSA is strongly temperature dependent, increasing as the temperature approaches from above the threshold for NAT formation (*Fish and Jones*, 1995). BrCl becomes the important nighttime reservoir under cold stratospheric conditions. Thus the reaction 2.54 has the greatest implication for the polar regions when PSCs are no longer present. BrCl undergoes photolysis readily (reaction 2.37). These reactions are important because they regenerate active Cl from reservoir species. $BrO_x$ concentrations are relatively unchanged by these and indeed all of the heterogeneous reactions (*Hendricks et al.*, 1999).

It is the heterogeneous bromine reactions on cold SSAs that have the greatest implications for ozone for all latitudes, and all seasons. $NO_x$ concentrations are suppressed, while $ClO_x$ concentrations are elevated by the reaction of bromine species on the surface of aerosols. The hydrolysis of $BrONO_2$ has been shown to be significant even in the presence

of background aerosol loading. The hydrolysis of $BrONO_2$ is found to increase the $BrO_x$, $ClO_x$ and $HO_x$ concentrations by ∼20 % (*Lary et al.*, 1996). apparent contradiction.

The hydrolysis of $BrONO_2$ is represented by the following cycle (*Lary et al.*, 1996):

$$\begin{aligned}
BrONO_2 + H_2O_{(l)} &\longrightarrow HOBr + HNO_3 \\
HNO_3 &\xrightarrow{h\nu} NO_2 + OH \\
HOBr &\xrightarrow{h\nu} Br + OH \\
2\times(OH + O_3 &\longrightarrow HO_2 + O_2) \\
Br + O_3 &\longrightarrow BrO + O_2 \\
BrO + NO_2 &\xrightarrow{M} BrONO_2 \\
\hline
\text{Net :} \qquad 3O_3 + H_2O_{(l)} &\longrightarrow 2HO_2 + 3O_2
\end{aligned} \tag{2.57}$$

The increase in OH concentration results in a change in the chlorine partitioning, by decreasing the lifetime of HCl (*Lary et al.*, 1996; *Hendricks et al.*, 1999). The nitric acid concentration is affected also by changes in the OH levels. However, increasing OH concentration results in enhanced production of this reservoir species. The decrease in the $NO_x$ concentration reinforces the increase in the $ClO/ClONO_2$ partitioning ratio. The hydrolysis of $BrONO_2$, the dominant species due to twilight homogeneous reactions, converts essentially all of the reactive bromine during the night to HOBr at mid-latitudes (*Fish and Jones*, 1995). It is HOBr that produces the dramatic increase of OH at sunrise (*Salawitch et al.*, 1988). HOONO2???

At low temperatures, but above the PSC threshold, typical of those in the polar regions when PSC processing is not occurring, HOBr can react with HCl in sulfate aerosols and directly release active Cl (*Lary et al.*, 1996; *Wagner*, 1999):

$$\begin{aligned}
BrONO_2 + H_2O_{(l)} &\longrightarrow HOBr + HNO_3 \\
HNO_3 &\xrightarrow{h\nu} NO_2 + OH \\
HOBr + HCl_{(l)} &\longrightarrow BrCl + H_2O_{(l)} \\
BrCl &\xrightarrow{h\nu} Br + Cl \\
OH + O_3 &\longrightarrow HO_2 + O_2 \\
Br + O_3 &\longrightarrow BrO + O_2 \\
Cl + O_3 &\longrightarrow ClO + O_2 \\
BrO + NO_2 &\xrightarrow{M} BrONO_2 \\
\hline
\text{Net :} \qquad HCl_{(l)} + 3O_3 &\longrightarrow HO_2 + ClO + 3O_2
\end{aligned}$$

This cycle provides a means for continued halogen processing of ozone after PSCs are no longer present but temperatures are still low, and after $NO_x$ begins to return to the denitrified polar stratosphere.

## Chapter 3

# Tropospheric Chemistry of Bromine

This Chapter discusses the role that bromine plays in tropospheric chemistry. Similar to its role in the stratosphere bromine is active in catalytic ozone depletion. High levels of BrO have been observed at mid-latitudes in close proximity to coastal regions, salt lakes and salt pans. BrO is also thought to play a role in the remote marine boundary layer. BrO has been observed in the free troposphere at high latitudes and inferences from observations of BrO at mid-latitudes indicate a free tropospheric background concentration of 0.5 - 2 ppt. In the polar regions large quantities of BrO have been observed in the boundary layer over the sea-ice. The mechanism driving these events is discussed. Bromine ions from the sea salt build up and the subsequent autocatalytic release transfers large quantities of bromine to the atmosphere. These 'bromine explosion' events result in large ozone losses in the boundary layer. During these events gaseous mercury is also oxidised and this has consequences for enhanced mercury deposition in these regions.

## 3.1 Tropospheric Ozone

Ozone is a toxic gas that causes a number of respiratory problems with prolonged exposure. Pre-industrial ozone concentrations at the surface were between 10 - 15 ppb, now even in clean air remote sites concentrations of 30 - 40 ppb are found (*Oltmans and Levy*, 1994; *Oltmans et al.*, 1998). Increases in $NO_x$ and volatile organic carbon (VOC) due to increased fossil fuel combustion are the major causes of this increase in tropospheric ozone. Photolysis of $NO_2$ and photochemical production from VOC are the major sources of anthropogenic tropospheric ozone. Injections of stratospheric ozone into the troposphere is another mechanism for the occurrence of tropospheric ozone. The international guidelines for 8 hours of safe exposure to ozone typically should not exceed 55 - 80 ppb. Levels of ozone as high as 500 ppb can be found in some densely populated urban areas (*Finlayson-Pitts and Pitts*, 1999). (example...)

When is max and min for tropospheric ozone???

## 3.2 Extra-Polar Boundary Layer

BrO has been measured at mid-latitudes from salt pans at the Dead-sea, Israel (*Hebestreit et al.*, 1999), and both BrO and ClO have been observed at Great Salt Lake, United States (*Stutz et al.*, 2002). IO has been observed in the remote marine boundary layer (*Alicke et al.*, 1999; *Allan et al.*, 2000). Measurements of these halogen radicals have shown strong anti-correlations with measurements of in-situ ozone.

Significant diurnal variations of ozone within the the remote tropical marine boundary layer have been observed along a cruise course of a ship (*Dickerson et al.*, 1999). Photolysis of $O_3$ and $HO_x$ chemistry can account for only half of the variation seen. Chemical cycles involving BrO have been suggested to explain the magnitude of the ozone diurnal variation in the remote marine boundary layer. Attempts to measure BrO above the remote marine boundary have been largely unsuccessful (*Platt*, 2000), though recent work by *Leser et al.* (2003) has successfully observed BrO in the remote marine boundary layer at 35°N.

## 3.3 Polar Boundary Layer

The phenomenon of almost complete depletion of surface ozone was first reported at Alert in the Canadian Arctic by *Bottenheim and Gallant* (1986). Since then several reports of low ozone episodes (LOE) during the polar springtime have been made for the Arctic sites of Alert (*Barrie et al.*, 1988), Barrow, Alaska (*Sturges et al.*, 1993; *Bottenheim et al.*, 1990), Ny-Ålesund, Spitsbergen (*Solberg et al.*, 1996; *Tuckermann et al.*, 1997), and Kangerlussuaq, Greenland (*Miller et al.*, 1997). LOEs have also been observed in the Antarctic springtime at Arrival Heights (*Kreher et al.*, 1997), Neumayer (*Friess*, 2001) and Syowa (*Murayama et al.*, 1992). During LOEs, ozone levels drop from normal (30 - 40 ppb) to unmeasurable (<2 ppb) (*Tuckermann et al.*, 1997). *Barrie et al.* (1988) observed a strong anti-correlation between particulate Br and ozone. The bromine has been unequivocally verified experimentally to be in the form of BrO. During LOEs BrO mixing ratios of between 20 - 60 ppt have been observed in the polar regions, this has led to these events being referred to as 'bromine explosions'. Measurements of $SO_x$, Br, Cl, I and $NO_x$ during the Polar Sunrise Experiment 1992 found bromine to be the only species to display a strong correlation of any sort with surface ozone concentrations (*Barrie et al.*, 1994).

Images of the BrO column from GOME indicate that enhanced levels are frequent and episodic above the sea ice in the springtime polar regions (*Wagner and Platt*, 1998; *Richter et al.*, 1998).

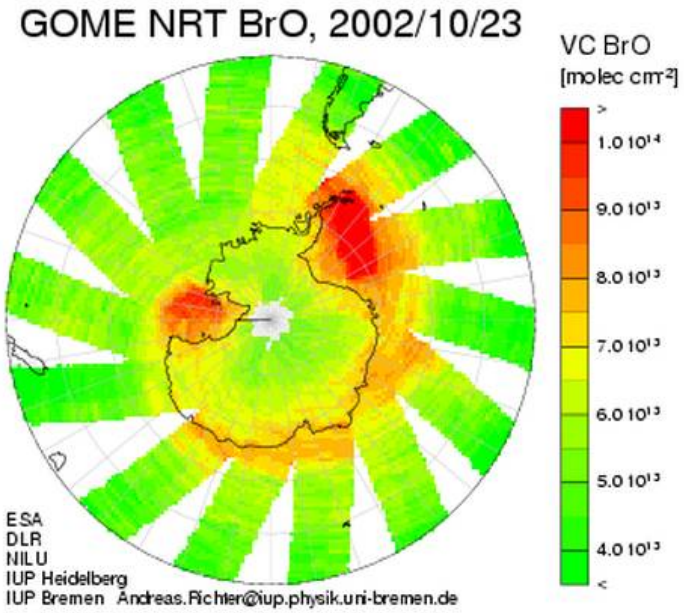


**Figure 3.1**: The GOME satellite experiment BrO map of the southern hemisphere on 23rd October 2002. Areas of enhanced BrO columns are clearly evident around the Antarctic continent. Image is courtesy of Andreas Richter, it is preliminary and obtained from the website http://www.iup.physik.uni-bremen.de/gomenrt/

### 3.3.1 The Mechanism Driving BrO Explosion Events

The source of the bromine driving the 'bromine explosion' events was disputed. Methyl bromide ($CH_3Br$) is the most abundant tropospheric bromine containing gas, having both natural and anthropogenic origins (*Finlayson-Pitts and Pitts*, 1999; *Sturges et al.*, 2000). Bromoform ($CHBr_3$), though less abundant than methyl bromide due to its short tropospheric lifetime, has the higher reactivity. For these reasons $CHBr_3$ was suggested to explain the high levels of BrO observed during LOEs (*Sturges et al.*, 1993; *Barrie et al.*, 1988). The photodissociation of $CHBr_3$, however, is too slow, and the $CHBr_3$ levels too low, to account for the BrO levels observed (*Tang and McConnell*, 1996). Similarly, the proposal of $N_2O_5$ on air-borne sea-salt forming $BrNO_2$ and ultimately producing BrO (*Finlayson-Pitts et al.*, 1990) was considered insufficient to be the primary source of the BrO driving LOEs (*Tang and McConnell*, 1996; *McConnell et al.*, 1992). Autocatalytic release of bromine from the snow pack during the polar spring is suggested by *Tang and McConnell* (1996) to account for the high levels of BrO observed during LOEs. Wind borne sea-salt (bromine and chlorine ions) is suggested to accumulate on the snow pack

during the polar night (*Tang and McConnell*, 1996; *McConnell et al.*, 1992). The autocatalytic cycle proposed is activated by a bromine seed, such as one formed from photolysis of $CHBr_3$ .

$$CHBr_3 \xrightarrow{h\nu} CHBr_2 + Br \tag{3.1}$$

The Br radical then reacts via heterogeneous reactions to produce BrO then BrOH, which rapidly reacts with $Br^-$ ions from the sea salt accumulation in the snow pack resulting in the production of two Br radicals to start the cycle again (see reaction 3.9). While the photolysis of $CHBr_3$ is slow, the rapid autocatalytic release of the $Br^-$ ions from the snow pack to the atmosphere is rapid, occurring over only a few hours. The BrO self reaction and the reaction with $HO_2$ are the dominating catalytic cycles that lead to boundary layer ozone depletion (*Vogt et al.*, 1996; *Honninger and Platt*, 2002):

$$2\times(Br + O_3 \longrightarrow BrO + O_2) \tag{3.2}$$
$$BrO + BrO \longrightarrow 2Br + O_2 \tag{3.3}$$
$$\text{Net :} \quad 2O_3 \longrightarrow 3O_2$$

$$BrO + HO_2 \longrightarrow HOBr + O_2$$
$$HOBr \xrightarrow{h\nu} OH + Br$$
$$Br + O_3 \longrightarrow BrO + O_2$$
$$OH + O_3 \longrightarrow HO_2 + O_2$$
$$\text{Net :} \quad 2O_3 \longrightarrow 3O_2$$

The efficiencies of these reactions can be increased when IO or ClO replaces BrO in the above cycles. In the troposphere, like the stratosphere the catalytic cycles are stopped by the formation of reservoir species. The following reservoir forms of reactive bromine are favoured in the troposphere (*Fitzenberger et al.*, 2000):

$$BrO + HO_2 \longrightarrow HOBr + O_2 \tag{3.4}$$
$$Br + RH \longrightarrow HBr + R \tag{3.5}$$
$$BrO + NO_2 \xrightarrow{M} BrONO_2 \tag{3.6}$$

where R is an organic radical. The formation of HBr, HOBr and $BrONO_2$ ends the catalytic ozone destruction cycles. An activation mechanism is required for the regeneration of BrO and Br from the non-radical species of HBr, HOBr and $BrONO_2$. Heterogeneous reactions on the surface of ice and aerosol particles provide such a mechanism (*Fitzen-*

*berger et al.*, 2000):

$$BrONO_2 + H_2O \longrightarrow HOBr + HNO_3 \quad (3.7)$$

$$HOBr + Cl^- + H^+ \longrightarrow BrCl + H_2O \quad (3.8)$$

$$BrCl + Br^- \longrightarrow Br_2 + Cl^- \quad (3.9)$$

LOEs are observed with (and perhaps because of) the existence of strong surface temperature inversions which stabilize the boundary layer, which extends from the surface up to ∼2 km. A negative temperature gradient is seen within the boundary layer, this is 'capped' by a thermally stable layer (positive temperature gradient), which inhibits convection and thus suppresses vertical mixing of the boundary layer with the free troposphere above (*Solberg et al.*, 1996). The stability of the boundary layer breaks down in summer allowing vertical mixing with the free troposphere (*Kreher et al.*, 1997). It cannot be discounted that ozone depletion due to these halogen reactions may be more widespread and frequent, but only detectable within the confines of the stable boundary layer (*Solberg et al.*, 1996).

A study of historical ozonesonde records from Arctic and Antarctic sites indicates an increased frequency of bromine explosion events in recent times (*Tarasick and Bottenheim*, 2002). This increased frequency has been postulated to explain the increased mercury levels found in Arctic biota in recent years, as described in the next section.

### 3.3.2 Mercury

Unlike other heavy metals, which reside as particulates, mercury exists in the atmosphere in its gaseous phase. Mercury is extremely toxic and bioaccumulative. Increased levels of mercury are observed in Arctic food supplies and the inhabitants of circumpolar countries. Elemental vapour phase mercury $Hg^0$ has a long atmospheric residence time (∼1 year) and undergoes long-range transport on a global scale. Anthropogenic sources are equal to, or in excess of, natural sources of gaseous mercury. Mercury is converted to methyl mercury by biological processes and a million-fold concentration is observed in aquatic food chains. Methyl mercury is able to cross the blood-brain barrier, hence there are major health concerns with being exposed to high levels of mercury (*Schroeder and Munthe*, 1998).

It is hypothesized that increased levels of bromine associated with the LOEs facilitates the oxidation of vapour phase $Hg^0$ in the atmosphere (*Lu et al.*, 2001). Oxidation of $Hg^0$ produces $Hg^{2+}$ which has a higher reactivity, thus increasing levels of mercury deposition in the Arctic (*Schroeder et al.*, 1998). High mercury deposition levels have also been observed at the coastal Antarctic station of Terra Nova (*Sprovieri et al.*, 2002) and at Neumayer (*Ebinghaus et al.*, 2002). The correlation of high BrO with low surface

ozone and high deposition of mercury indicates that some interesting chemistry could be occurring in the polar boundary layer. The effects of increasing mercury deposition are far reaching within the fragile polar biosphere.

## 3.4 Free Troposphere

Studies are accumulating that indicate that BrO is present in the free troposphere. A tropospheric BrO profile has been observed from a balloon platform (*Fitzenberger et al.*, 2000) at Kiruna, 67°N. *McElroy et al.* (1999) have also observed BrO in the free troposphere in the Arctic and suggest transport over ice leads as a mechanism for the transport of boundary layer BrO into the free troposphere.

At mid-latitudes a tropospheric background of 1 - 2 ppt has been inferred from ground-based zenith-sky, balloon observations and satellite measurements of BrO (*Harder et al.*, 1998; *Van Roozendael et al.*, 2000, 2002; *Mueller et al.*, 2002). BrO tropospheric columns derived from the Global Ozone Monitoring Experiment (GOME) indicate that a ubiquitous BrO background concentration of 0.5 - 2 ppt is present in the free troposphere above the remote Pacific ocean (*Richter et al.*, 2002).

## Chapter 4

# Measurements

In this chapter, the remote sensing ground-based UV-Visible spectroscopic techniques employed in this work to sample the atmosphere for BrO are detailed. The viewing geometries of direct-sun and zenith-sky are used to obtain complementary sensitivities to different parts of the atmosphere. The spectral fitting procedure of Differential Optical Absorption Spectroscopy (DOAS) is detailed. The determination of Differential Slant Column Densities (DSCD) from the spectral measurements is outlined. It is the DSCDs that are used to construct the measurement vector $\mathbf{y}$. A retrieval (see Chapter 6) can then be performed so that $\mathbf{y}$ is fitted using the forward model (see Chapter 5). A description of the Langley plots and Air Mass Factors (AMFs) is also provided.

## 4.1 Spectroscopy

Spectroscopy is the study of electromagnetic radiation and its interaction with atoms and molecules. In the Earth's atmosphere electronic transitions involve the largest amount of energy transfer (photons absorbed or emitted), and occur in the visible and ultraviolet wavelength region ($\lambda < 700\,\text{nm}$). When an electron changes its electronic state this generally leads to changes in the vibrational state of the molecule, so an electronic transition usually has an associated vibrational structure. Vibrational transitions of the ground electronic state are much less energetic and are generally associated with spectroscopy in the infrared (IR) region ($\lambda > 1000\,\text{nm}$). The third and very low energy transition is the rotational transition. Pure rotational transitions occur in the microwave wavelength region of the spectrum. Vibrational transitions have an associated rotational structure (*Atkins*, 1994). Providing spectral parameters (i.e. absorption cross-sections) are known the electronic spectral bands occurring at UV and visible wavelengths can be exploited to study atmospheric composition.

Spectroscopy in the UV-Visible allows the detection of species with distinct absorption features ($\sim$5 nm in width or less) on a background that contains broadband absorbers, Mie and Rayleigh scattering features. There are a vast number of trace gas species detectable; for example, HONO, OH, BrO, ClO, OClO, NO, $NH_3$, IO, $NO_2$, $NO_3$, $O_3$, $SO_2$, $CS_2$, HCHO, $O_4$, and $H_2O$.

Fluorescence spectroscopy has been successfully applied to the study the radical NO

and OH species in the atmosphere, however it is not used to study BrO and ClO as these species do not fluoresce. For the spectroscopic study of BrO in the atmosphere in this work the vibrational transitions of the electronic transition A $^2\Pi_{3/2} \leftarrow$ X $^2\Pi_{3/2}$ is used.

## 4.2 Viewing Geometries.

Spectroscopic observations can be made from a number of viewing platforms. Direct-sun spectroscopic measurements can be ground-based or made from a balloon platform (*Ferlemann et al.*, 1998). Spectroscopic observations of scattered light can be made at a number of angles: zenith viewing elevation angle is 90° (*Solomon et al.*, 1987), or multi-axis with smaller elevation angles as well as 90° (*Sanders et al.*, 1993). UV-visible spectroscopy has also been successfully implemented in the satellite experiments of GOME (*Burrows et al.*, 1999) and SCIAMACHY (*Noel et al.*, 1999).

The Solar Zenith Angle (SZA) (refer to figure 4.1) gives the angle of the sun in the sky with respect to the observer. It is expressed from the zenith, thus high SZAs are associated with the sun close to the horizon. The direct-sun geometry samples a single light path through the atmosphere. The slant path enhancement over the vertical for the troposphere is up to 20 times for the direct-sun geometry at high SZAs.

Zenith-sky spectroscopy samples light that has traversed a number of paths before being scattered into the detector. The density of air, aerosols and the wavelength region determine the altitude at which most of the detected light has been scattered. Very generally at $\lambda = 350$ nm for SZAs between 60° and 70° this maximum scattering altitude is $\sim 5$ - 10 km. Below this altitude the light has traversed a vertical path into the detector. For larger SZAs; between 80° and 90°, this maximum scattering altitude is higher, $\sim 15$ - 30 km. The light path enhancement for the stratosphere can be up to 20 times that of the vertical path. However, in contrast to the direct-sun geometry, the light has only traversed a vertical path through the troposphere into the detector.

Multi-axis viewing geometry at elevation angles of 10°, 15° and 20° measures long pathlengths through the troposphere at all SZAs. This method is very sensitive to tropospheric trace gas absorption. The light scattered from the troposphere has a high probability of being multiply scattered. Thus, the quantitative interpretation of multi-axis measurements necessitates the use of a multiple scattering model.

The different atmospheric sampling with varying SZAs allows ground-based measurements to provide altitude information about the atmospheric absorbers. The twilight periods are important for obtaining enhanced pathlengths for all these ground-based viewing geometries. The atmospheric sensitivities of the direct-sun and zenith-sky viewing geometries are quite different, because of the different altitudes of path enhancement. The direct-sun measurements are most sensitive to tropospheric absorbers, while the zenith-

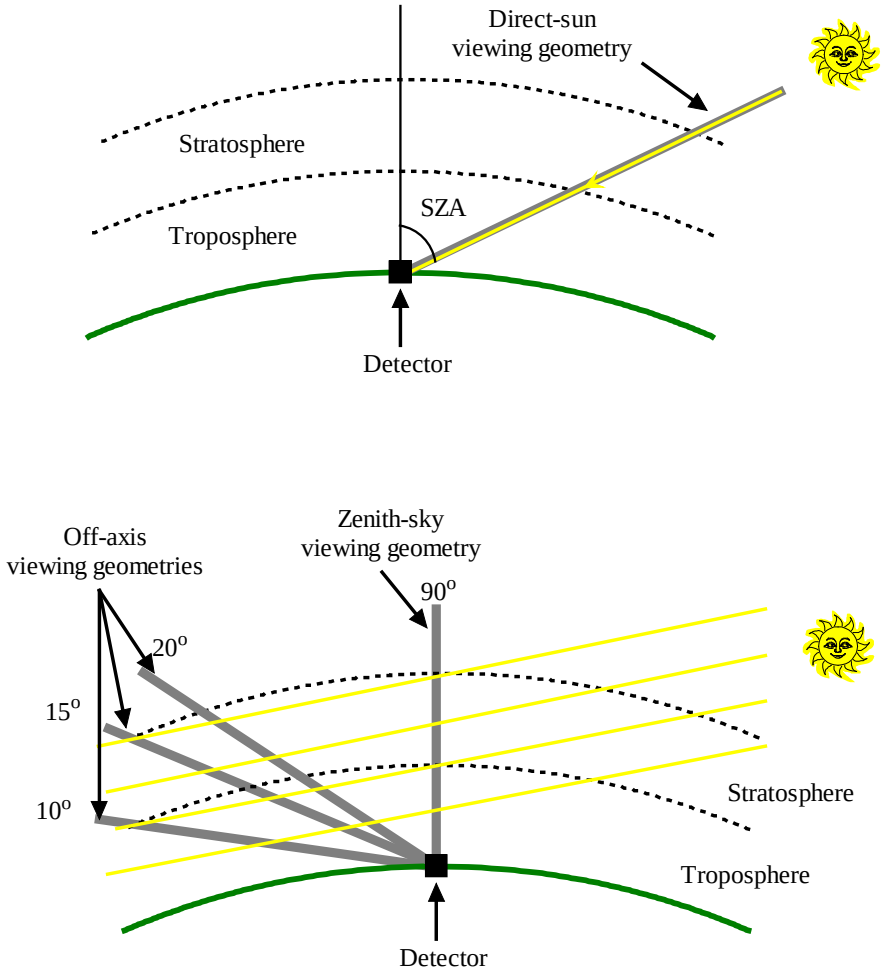


**Figure 4.1**: Schematic diagrams of the direct-sun viewing geometry (top) and zenith-sky and multi-axis (bottom). The grey lines from the detector indicate the viewing geometries of the detector. The Solar Zenith Angle (SZA) is the angle that the sun makes with the zenith. With changing elevation of the sun the different viewing geometries sample different paths through the troposphere and stratosphere.

sky observations are more sensitive to the stratospheric component.

### 4.2.1 Direct-sun Instrument

A 'direct-sun' viewing instrument designed at NIWA, Lauder is used to obtain BrO DSCDs. Figure 4.2 illustrates the instrumental set up for the direct-sun viewing geometry.The direct-sun spectrometer at Lauder was an Acton 275 (a Czerny Turner spectrometer with spherical mirrors). The detector was a Hamamatsu back tinned charge coupled device (CCD) module with 1044 3.2 mm×0.024 mm pixels. The detector was cooled to -20 °C. The 1200 g/mm grating provides a wavelength coverage of 324 – 395 nm at a resolution of 0.5 nm. The sunlight was directed into the instrument using a solar tracker. A telescope lens focuses the incident light on a dichroic filter, which reflects light

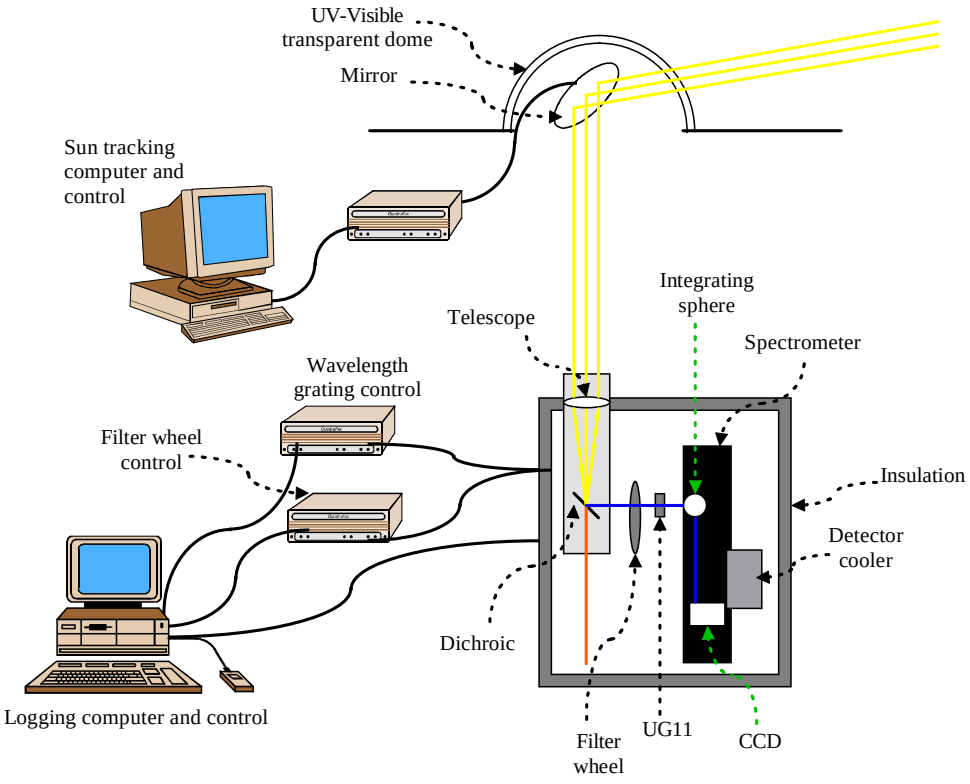


**Figure 4.2**: Schematic diagram of the instrument set-up for the direct-sun viewing geometry.

between 325 – 475 nm into the instrument. This light was then filtered using switchable neutral density filters on a filter wheel (providing factors of 0, 10, and 100 times attenuation) to extend the dynamic range over which measurements were made. A UG11 Schott filter attenuated light between 400 – 670 nm to reduce stray light within the instrument. An integrating sphere was used at the entrance slit to ensure that the intensity across the field of view was homogenized. A field of view of 1° towards the sun ensured the full sun was always sampled despite small tracking errors. A National Instruments interface card together with a Lab View program was used to collect, integrate and file spectra at 3 minute intervals.

### Multiple-scattering in Direct sunlight

To investigate the contribution of scattered light in the direct sun intensity received by the detector an intensity test was performed. This was done to ensure that the detected intensity from the direct beam had a negligible multiple scattering component. On the morning of day 137, 2002 the focused image of the direct sun beam was moved off the entrance optics by 1° (twice the width of the sun's image), referred to as 'off-sun'. Figure 4.3 shows the result of this test.

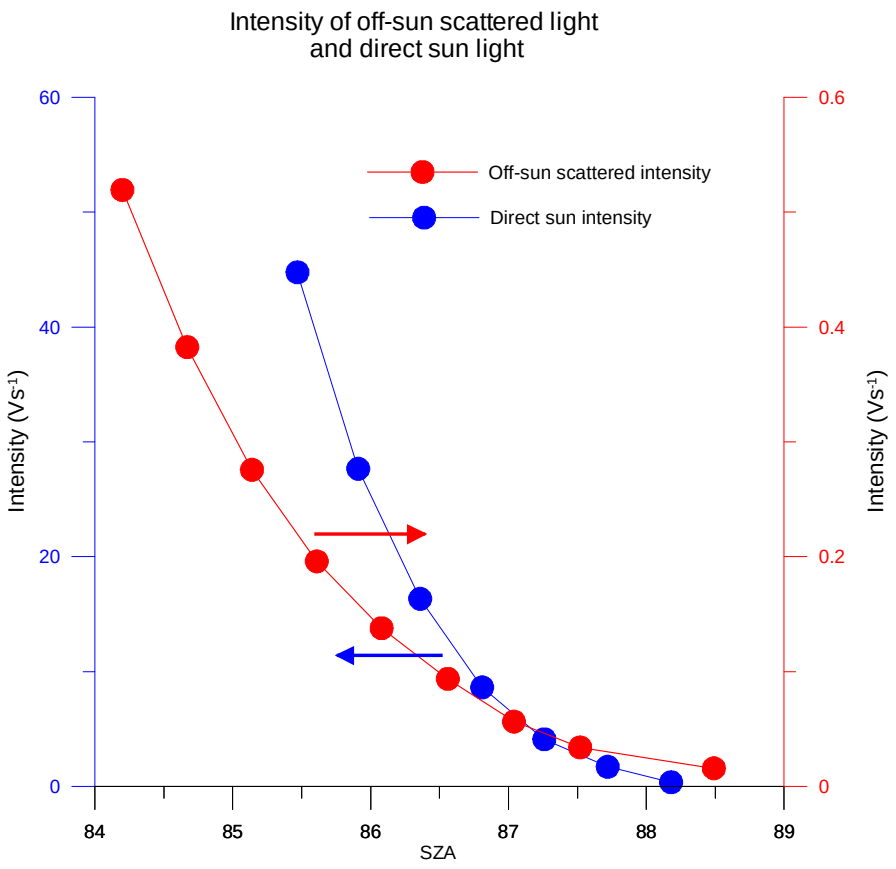


**Figure 4.3**: The intensity of the direct sun intensity is compared with the off-sun intensity. This is a quality assurance test to ensure that the 'direct-sun' measurements contain only a negligible contribution of light that has been multiple scattered. The red line is the off-sun intensity and is associated with the right axis. The blue line is the direct sun intensity and is associated with the left axis. Where the lines intersect the off-sun intensity is 1 % of the direct sun light, this is at 87°.

The resultant intensity (signal volts per second at each angle) is compared with the intensity of the direct sun light measured on the morning of day 138. Up until a SZA of 87° the off-sun intensity is less than 1 % of the direct sun intensity. At 88° the off-sun intensity made up 4 % of the direct sun light intensity. Multiple scattering in the direct sun light only becomes an issue for measurements above 88°.

### 4.2.2 Zenith-sky Instrument

BrO zenith-sky measurements have been conducted at Arrival Heights since 1993. For a complete instrument description refer to *Kreher et al.* (1996). Zenith scattered light is directed into the entrance slit of the Czerny-Turner Acton 500 spectrograph. The 1200 g/mm grating provides a wavelength coverage of 324 - 600 nm at a resolution of 0.5 nm. A f/6.9 lens focuses the scattered light into the entrance slit of the spectrometer (field of view of 8°). The detector is a photodiode array detector consisting of 1024

independent silicon diodes. The detector is cooled to -50°C.

The zenith-sky instrument conducting measurements at Lauder is a polarised Czerny-Turner spectrometer. Zenith scattered light is observed with a field of view of 14°. The 1200 g/mm grating provides a wavelength coverage of 331 - 390 nm at a resolution of 0.6 nm. The Reticon 1024 photodiode array detector (*Mount et al.*, 1992) is cooled to -80°C.

## 4.3 Spectral Fitting

Differential Optical Absorption Spectroscopy (DOAS) is associated with a large number of definitions. The 'differential' originated from the fitting of an absorption feature above the spectral background baseline (not the true baseline). It has now come to mean the whole spectral fitting procedure by which a SCD or DSCD is determined from a spectral measurement. It is not the only means of determining a line of sight measurement from radiance measurements, in fact optimal estimation can be and is used for this purpose (*Rodgers*, 2000). DOAS is the spectral fitting technique employed here to determine the DSCDs from the radiance measurements (for DOAS reviews see *Noxon* (1975), and *Platt* (1994)). DOAS targets the detection of species with distinct absorption features ($\sim$5 nm in width or less) on a background that contains broadband absorbers, Mie and Rayleigh scattering features.

To eliminate solar spectral Fraunhofer features from the spectral measurements, the twilight spectra are ratioed with a noon spectrum. The DOAS procedure is then applied to this difference spectra to evaluate a differential SCD (differential with respect to the reference spectrum). When it is possible to measure a background with no absorber present, such as satellite measurements, then SCDs can be determined using DOAS (*Richter et al.*, 2002).

Low order polynomials are fitted to approximate the Rayleigh, Mie and broadband absorption features that vary slowly with wavelength. High pass filtering is used to determine the background baseline. The differential cross-section of each absorber expected to be present is fitted. A non-linear least squares fitting procedure (*Aliwell et al.*, 2002) is used to fit the cross-sections and to determine the absorption for each of the absorbers. Figure 4.4 displays the BrO differential absorbance fits arising from twilight spectra over Lauder.

### 4.3.1 Combining Instruments

The introduction of additional errors into the retrieval due to using the spectral measurements from two different instruments was considered. Deriving DSCDs from the zenith-sky and direct-sun viewing modes with the same instrument may avoid some of

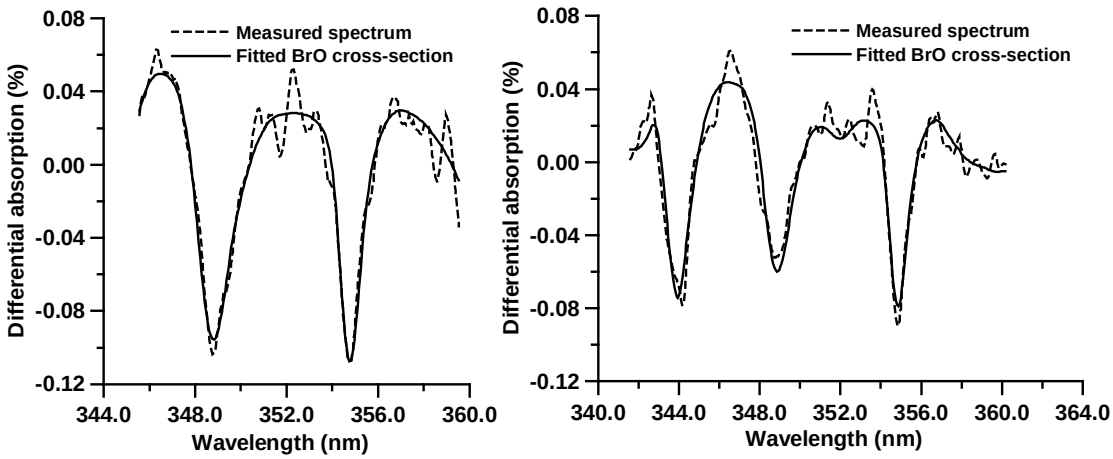


**Figure 4.4**: The typical spectral fits for BrO at 87.3° SZA for the direct-sun (left) and 88.1° SZA for the zenith-sky (right) measurements made on day 254, 2001, sunset at Lauder. The small scale features are remnants of Ring fitting procedure.

the instrumental unknowns, such as the instrument functions, field of view, spectral resolution and grating differences. However, for one instrument to measure in both zenith-sky and direct-sun viewing modes requires that quite different optics and spectral fitting are used for the two different modes. In observing the direct-sun the attenuation of the light intensity is necessary, which is not required in the zenith-sky mode. Zenith-sky observations contain a high Ring component (see section 4.3.3) and the wavelength range considered is wider than in the direct-sun case. Direct-sun observations have only a low Ring contribution as the direct-sun is not measuring scattered light. However, the direct-sun measurements do contain strong absorption features from tropospheric species such as $O_4$ and HCHO that are absent in the zenith-sky spectra. A shorter wavelength range is appropriate for the direct-sun DSCD derivations due to $O_4$ absorption (refer to figure 4.4 for the spectral fitting windows). Two different instruments with instrumental differences optimized for each particular geometry is not a disadvantage over one instrument measuring in two modes due to the very different requirements of the two modes.

### 4.3.2 Absorption Cross-Sections

The absorption cross-sections and their dependence on temperature lead to the greatest uncertainties in the DSCD determination. The difference between experimentally determined cross-sections gives some indication of this uncertainty. Temperature dependence of absorption cross-sections is another problem when measuring atmospheric trace gases. Stratospheric absorbers are experiencing temperatures in the range of 230 - 250 K but tropospheric absorbers have a temperature range of 230 - 298 K. When spectra are fitted with a cross-section typical of one temperature, an error is introduced to the derived spectral

quantity.

Two cross-sections are fitted for ozone (for the temperatures of 202 K and 241 K). For $NO_2$ cross-sections at both 227 K and at 294 K are fitted. For BrO a cross-section at 228 K is used (*Wilmouth et al.* (1999) see figure 4.5). The cross-sections for BrO at 298 K and an older 228 K cross-section are also displayed to illustrate the variation for BrO.

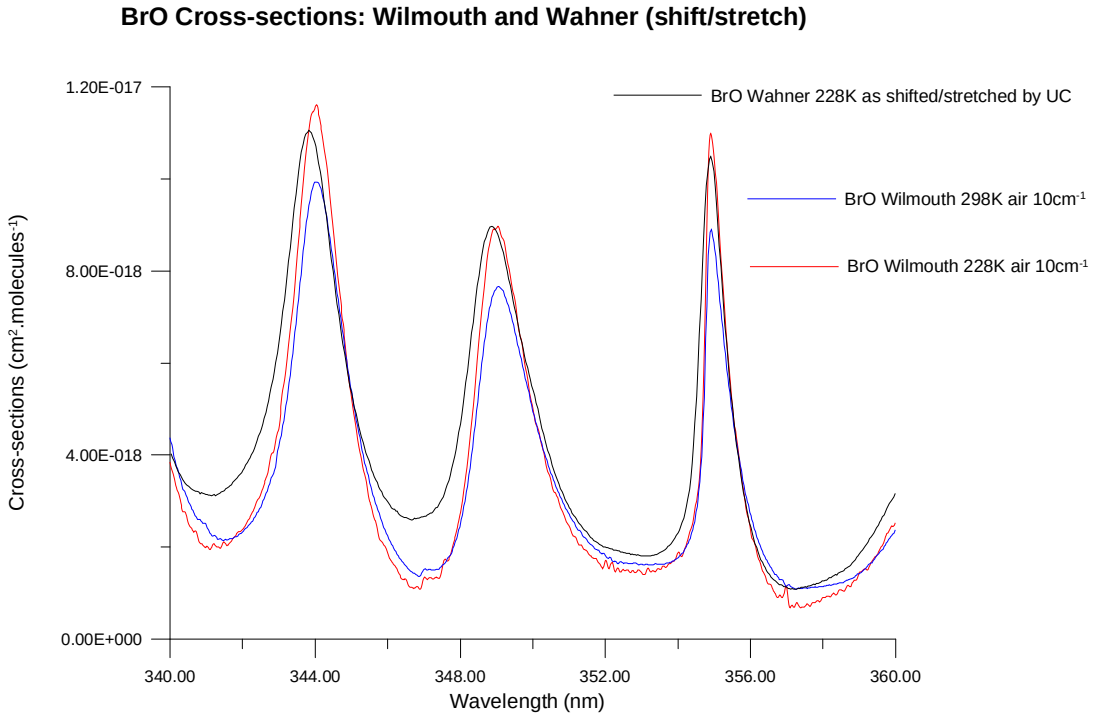


**Figure 4.5**: The cross-section for BrO from *Wahner et al.* (1988) at 228 K shifted and stretched, and the more recently measured cross-sections at 228 K and 298 K of *Wilmouth et al.* (1999).

### 4.3.3 Rotational Raman Scattering - Ring Effect

When electromagnetic radiation interacts with a molecule such that the transmitted radiation is of a different wavelength than the incident radiation, Raman scattering has occurred. If the molecule absorbs some of the photon's energy this is then known as Stokes scattering. Conversely, if the molecule is initially excited and it can add to the energy of the transmitted photon this is known as Anti-Stokes scattering. Rotational Raman scattering requires that the molecule be anisotropically polarizable. This means the alignment of the molecule parallel or perpendicular to the electric field results in different induced dipoles. Different polarizations occur with respect to the molecule's orientation (thus rotation) in an electric field. Diatoms ($H_2$, $N_2$, $O_2$ etc) therefore have rotational Raman activity; in fact only rotationally symmetric molecules aren't active (*Atkins*, 1994).

The Fraunhofer lines in the spectra recorded for scattered sunlight have reduced intensities relative to the spectra recorded for direct sun-light. This effect is termed the 'Ring effect' after (*Grainger and Ring*, 1962). A number of causes for this effect were proposed such as airglow and aerosol fluorescence, but it is widely accepted that rotational Raman scattering by $O_2$ and $N_2$ is the cause of this infilling of the Fraunhofer lines (*Fish and Jones*, 1995).

The Fraunhofer lines are eliminated by ratioing spectra with respect to a reference spectrum. The magnitude of the infilling of the Fraunhofer lines due to Raman scattering ('Ring effect') changes over the twilight period. Thus, when DSCDs are being determined for the zenith-sky viewing geometry by ratioing a twilight with a noon spectrum not all of the solar spectral effects are eliminated. The 'Ring effect' introduces structure in the ratio spectra at the Fraunhofer lines, similar in magnitude to absorption features of $NO_2$, BrO and OClO.

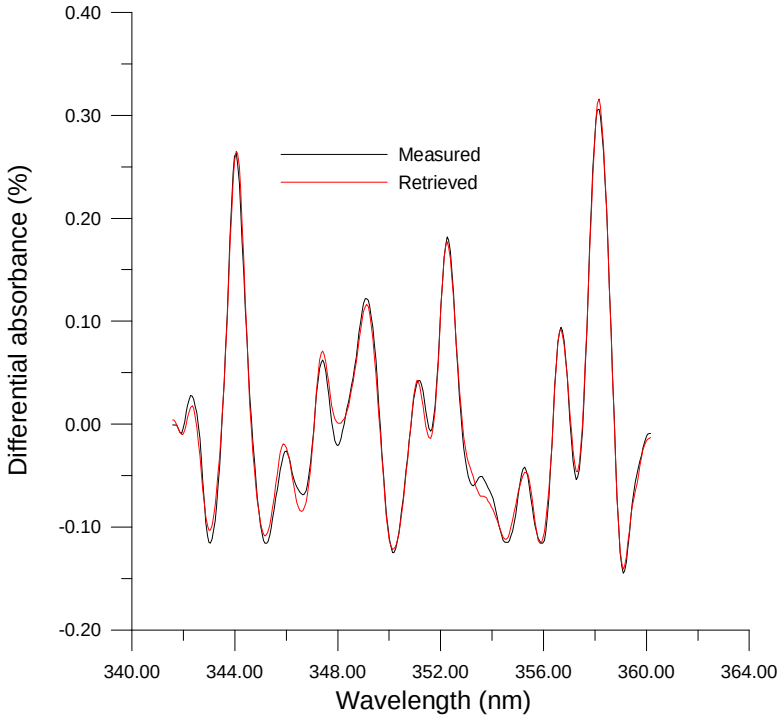


**Figure 4.6**: The spectral fit for ring at 88.1° SZA for the zenith-sky measurements made on day 254, Lauder 2001, sunset.

To account for this 'Ring effect' an absorber-like differential cross-section is determined. The two most commonly used methods are; the determination from polarized measurements (*Solomon et al.*, 1987) or direct calculation from rotational Raman scattering by $O_2$ and $N_2$ (*Fish and Jones*, 1995). Another method for determination of the 'Ring' cross-section is to approximate it using the reciprocal of the 'Fraunhofer spectrum' (*Noxon*, 1975). The 'Ring' cross-section is then fitted to eliminate the Ring effect structure

in the ratio spectra.

Rotational Raman Scattering also reduces the intensities of absorption lines, (especially those features which have structures that are finer than 6 nm) and thus can lead to an underestimation of the DSCDs. $NO_2$ SCDs are underestimated by $\sim 8\,\%$ at 90° and up to 12 % at 95° SZA (*Fish and Jones*, 1995). The effect of rotational Raman scattering on BrO and OClO SCDs is expected to be similar to that of $NO_2$. $NO_2$ is typically observed at 450 nm, OClO and BrO are at shorter wavelengths of 420 nm and 350 nm respectively. The effect of rotational Raman scattering scales with the number of multiple scattering events, and since the Rayleigh scattering cross-section is larger at shorter wavelengths this could mean that Raman scattering may be more important for BrO and OClO zenith-sky SCDs.

### 4.3.4 Polarization

Light is termed to be polarized if the light intensity is a function of the orientation of the observation plane. Stokes parameters are used to parameterize polarization. Direct sun-light is unpolarized; but when light undergoes either molecular scattering or reflection the light becomes polarized. Light that undergoes Rayleigh scattering is highly polarized if viewed perpendicular to the incident light direction.

Light that has undergone Raman scattering is largely (though not entirely) unpolarized (*Aben et al.*, 2001; *Stam et al.*, 2002). It is on this premise that a cross-section for the 'Ring effect' can be measured using the ratio between the intensity of light of parallel ($I_\parallel$) and perpendicular ($I_\perp$) orientations (*Fish*, 1994).

$$\frac{I_\parallel}{I_\perp} = \frac{\sigma_\parallel + \sigma_{Ring}}{\sigma_\perp + \sigma_{Ring}} \tag{4.1}$$

which rearranged gives

$$\sigma_{Ring} = \frac{\sigma_\parallel - \sigma_\perp \frac{I_\parallel}{I_\perp}}{\frac{I_\parallel}{I_\perp} - 1} \tag{4.2}$$

### 4.3.5 Instrumental Resolution Function

The instrumental resolution function (or transmission) with respect to wavelength is commonly referred to as the slit function. The instrumental resolution function is required to describe the properties of the instrument. The resolution of the instrument and its optical properties contribute to each instrument having unique properties. The instrument resolution function is measured using a mercury lamp emission light source, and is important for the interpretation of all spectra. It is essential that the instrument is stable with respect to the instrument resolution function. This function should not change during

the measurement of solar spectra.

### 4.3.6 Dark Current

Dark current, as the name suggests, is the current that is present in the detector in the absence of light. Thermal energy is largely responsible for this current. Only when the detector is cooled to temperatures less than -80°C can the contribution of this dark current to the detector signal be considered negligible.

A constant temperature is essential to ensure that the background current does not change during the measurement. The contribution of the dark current to each spectral measurement must be subtracted. A linear subtraction is not adequate to account for the dark current. The amount of dark current depends upon detector intensity saturation levels, thus it is actually more complicated than a simple subtraction. The dark current dependence on signal intensity levels is taken into account (for detailed descriptions on this refer to (*Stutz and Platt*, 1996; *Kreher*, 1996)).

## 4.4 Langley Plots and Air Mass Factors

'Air mass factor' (AMF) calculations are a commonly used method of approximating the vertical column densities (VCD) from the slant column amounts. AMFs give the enhancement of the absorber light path over the vertical. It is a means of simplifying the interpretation of the measurements. This approximation can introduce large errors if the actual trace gas distribution differs from the assumed distribution. A vertical distribution (shape and diurnal change) is required to be assumed in the determination of AMFs. The AMFs are then used to determine vertical columns. The solution is biased by the pre-determined vertical distribution (a fixed *a priori* if you like). It is a crude inversion, but can be used effectively in the simple interpretation of the measurements.

$$\mathrm{AMF} = \frac{\mathrm{SCD}}{\mathrm{VCD}} \tag{4.3}$$

In the removal of the Fraunhofer features (see section 4.3) any absorber present in the reference spectrum is also subtracted from all of the spectra. To account for this approximately the use of a Langley plot is common. A Langley plot is a linear fit of the DSCDs with AMFs. A rearrangement of the previous equation and the substitution of SCD=DSCD+$\mathrm{SCD_R}$ where $\mathrm{SCD_R}$ is the slant column density of the reference angle, gives the following linear expression:

$$\mathrm{DSCD} = \mathrm{VCD}\times\mathrm{AMF} - \mathrm{SCD_R} \tag{4.4}$$

This technique relies on a linear dependence of AMFs with SZA. Any diurnal variation in the trace gas species is not dealt with using this method. When using the Langley plot for BrO only those measurements made when no diurnal change is occurring are useful in the determination of the amount of absorber present in the reference spectrum. This reference amount once determined, is then added to all of the DSCDs to give the SCDs. An example of a Langley plot is given in figure 4.7.

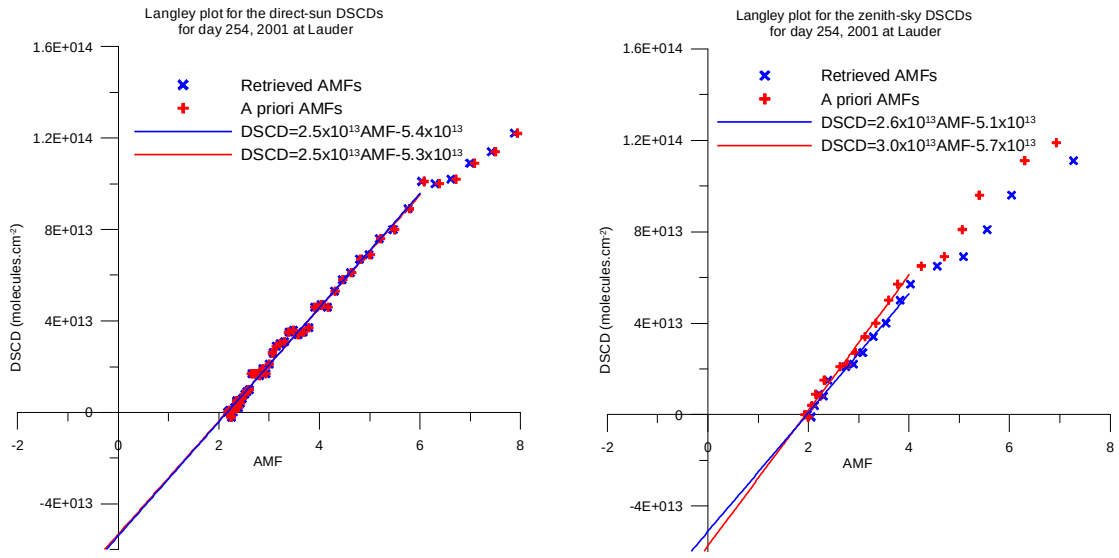


**Figure 4.7**: The Langley plot for the direct-sun DSCDs for day 254, 2001 at Lauder is displayed on the left. The Langley plot for the zenith-sky measurements is shown on the right.

| | Direct-sun | Zenith-sky |
|---|---|---|
| Retrieved | $6.2\times10^{13}$ molecules.cm$^{-2}$ | $5.8\times10^{13}$molecules.cm$^{-2}$ |
| Langley plot - *a priori* AMFs | $5.3\times10^{13}$molecules.cm$^{-2}$ | $5.7\times10^{13}$molecules.cm$^{-2}$ |
| Langley plot - retrieved AMFs | $5.4\times10^{13}$molecules.cm$^{-2}$ | $5.1\times10^{13}$molecules.cm$^{-2}$ |

**Table 4.1**: The values for the reference column amount derived using the Langley plot method for direct-sun and zenith-sky measurements. For comparison the values are given using AMFs determined for the *a priori* and retrieved vertical distributions of BrO. The reference column amount determined using the optimal estimation retrieval for day 254, 2001 is also provided for comparison.

Table 4.1 displays the amount of absorber present in the reference column for day 254, 2001 Lauder derived using the Langley plot method. For comparison the AMFs derived using the vertical distribution of BrO *a priori* and 'retrieved' are used. The 'retrieved' vertical distribution is obtained using the retrieval method outlined in Chapter 6. The reference column amount derived using the retrieval method described in the subsequent chapters is also provided. The difference between the two methods arises because the diurnal variation is fully treated over all measurements in the 'retrieved' case.

## Chapter 5

# Forward Model - Radiative Transfer

The inversion of the BrO DSCD measurements to provide desired altitude information requires a means of calculating the DSCDs from a vertical distribution of BrO. The forward model provides this and is an approximation to the complete description of the physics of the DSCD measurements and is related to these measurements by

$$\mathbf{y} = F(\mathbf{x}, \mathbf{b}) + \epsilon \tag{5.1}$$

where $\mathbf{y}$ is the measurement vector (DSCDs), and $F$ is the forward model. Here, the forward model is the radiative transfer determination of the DSCDs. The forward model requires a description of the state ($\mathbf{x}$), the quantity that is being retrieved, and the forward model parameters ($\mathbf{b}$), which affect the DSCDs but are not retrieved. $\epsilon$ is the error in the measurement.

The radiative transfer describes the ray tracing, scattering and absorption of the light path through the atmosphere. Thus, it enables the light received by the instrument to be modelled. The radiative transfer algorithms for the direct-sun and zenith-sky case contain essentially the same core equations. A spherical curved earth divided into discrete atmospheric shells is used in the model. Radiative descriptions for the two different viewing geometries of direct-sun and zenith-sky include the effects of refraction, Rayleigh scattering, Mie scattering and molecular absorption.

This chapter discusses how the DSCDs are determined. A single-scattering approximation is made in the zenith-sky DSCD determination and the implications of neglecting multiple scattering are discussed. The sensitivity curves or weighting functions describing how the forward model responds to changes in the state are derived. A validation of the radiative transfer algorithm is also described. The forward model algorithm developed in this work was written in Fortran90©.

## 5.1 Ray Tracing

The optical path(s) through the atmosphere must be determined to describe how the measurement samples the atmosphere. A common assumption in early radiative models was to assume a linear light path (*Solomon et al.*, 1987; *Sarkissian et al.*, 1995a). Refrac-

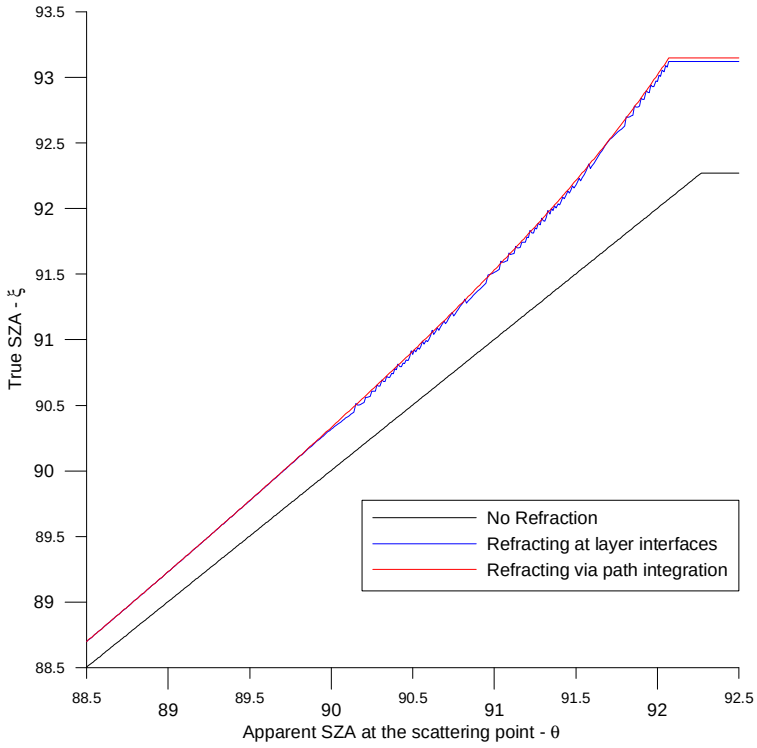


**Figure 5.1**: The effect of refraction on the true SZA calculation for a single light ray at 5 km using a model layer width of 20 m. Even with such fine layering the effects of the refraction equation singularity at the tangent point is evident for the case where refraction occurs at the layer interface. The apparent angle is the angle that the light ray is scattered into the field of view of the detector - $\theta$ and the true angle is the local SZA $\xi$ (see figure 5.6 to see how these quantities are determined).

tion is the optical property whereby the light bends due to the changing densities of the atmosphere. Refraction allows us to still see the sun (which is 0.5° in diameter) when it is actually below the horizon, and explains why the sun appears 'squashed' when on the horizon. Refraction is most important for the long tangential light paths associated with SZAs greater than 90°. To include the effects of refraction in a linear path model, such as that described by *Solomon et al.* (1987) refraction at the layer interface is necessary (*Fish*, 1994; *Preston*, 1995). Formulae for refraction at a layer interface (where $n$ is the refractive index, $\theta$ is the apparent angle and $dz$ is the layer width) are as follows:

$$\frac{n_1}{n_2} = \frac{\sin\theta_2}{\sin\theta_1} \tag{5.2}$$

or alternatively

$$d\theta = \frac{(n-1)}{H} dz \tan\theta_1 \tag{5.3}$$

Either way both these formulae are singular for the case where $\theta = 90°$, so are inadequate for describing a tangential light path. Figure 5.1 shows how using a linear path integration

and dealing with refraction at each atmospheric layer interface leads to noisy 'shark tooth' like features when describing the overall affect of refraction on the apparent versus actual SZAs. A very fine layering of 20 m is used and these features are still visible. Path and hence SCD calculations also have these characteristics when refraction is implemented in this manner and thus should be avoided by using the integrals described in the following section.

### 5.1.1 The Refracted Path

The extent to which a light path is refracted is controlled by the wavelength dependent refractive index $(n_s - 1)$. Under standard temperature and pressure conditions ($T_s = 288.15\,\mathrm{K}$, $P_s = 101325\,\mathrm{Pa}$) the refractive index is given by the following expression derived from experimental data (*Bucholtz*, 1995):

$$(n_s - 1) = \left( \frac{5791817}{238.0185 - (\frac{1}{\lambda})^2} + \frac{167909}{57.362 - (\frac{1}{\lambda})^2} \right) \times 10^{-8} \quad \lambda > 0.23\mu m \tag{5.4}$$

A more general expression for the refractive index $(n_{t,p} - 1)$ for a given altitude $(z)$ is obtained by temperature $(T(z))$ and pressure $(P(z))$ weighting the standard refractive index $(n_s - 1)$:

$$(n_{t,p} - 1) = (n_s - 1)\frac{T_s}{T(z)}\frac{P(z)}{P_s} \tag{5.5}$$

These formulae neglect the contribution of water vapour in the calculation of $n$, though this has only a very small affect ($\sim$0.3 %) (*Bucholtz*, 1995).

Snell's law in circular symmetry gives the following refractive index formula:

$$r_g = n(r) r \sin\theta \tag{5.6}$$

$r_g$ is a constant, known as the geometric tangent point or impact parameter. $r_g$ can be evaluated at the scattering point as $n$, $r$ and $\theta$ are all defined. Once $r_g$ is defined then the apparent angle $\theta$ can be calculated at all points along the ray for any altitude $r$ ($r = R_e + z$, the Earth centric radius), and $n$, which is defined for a given $r$ (equations 5.4 - 5.5). Including refraction requires that the model is run to determine the true SZA that corresponds to each apparent angle. The apparent angle is then able to be determined for the calculation of each true SZA. Figure 5.2 illustrates the terms used and the relevant geometries in the context of a layered atmosphere.

To avoid the singularity when including refraction in the ray tracing description, the variable for integration becomes $x = r\cos\theta = n^{-1}(n^2 r^2 - r_g^2)^{\frac{1}{2}}$ leading to the following

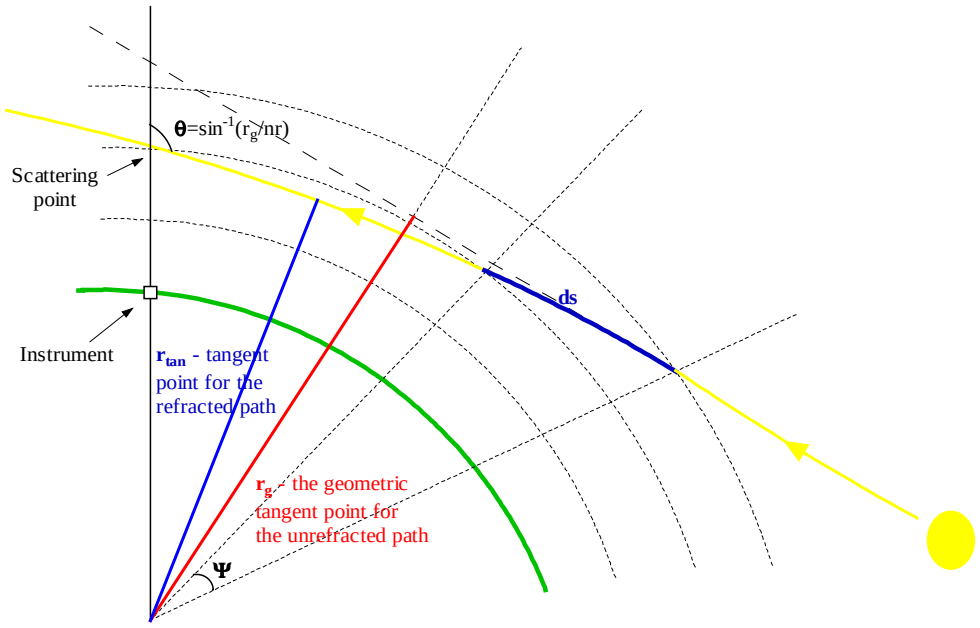


**Figure 5.2**: Schematic diagram displaying the refracted light path through a modelled layered atmosphere defined in spherical coordinates

integrals (*Kneizys et al.*, 1983; *Rodgers*, 2000):

$$\int ds = \int \frac{dx}{1-\gamma(r)\sin^2\theta} = \int \frac{n^2r^2dx}{n^2r^2-\gamma(r)r_g^2} \tag{5.7}$$

$$\int d\psi = \int \frac{nr_g dx}{n^2r^2-\gamma(r)r_g^2} \tag{5.8}$$

where

$$\gamma(r) = -\left(\frac{r}{n}\right)\frac{dn}{dr} \tag{5.9}$$

A hydrostatic atmosphere is assumed, thus the temperature and pressure profiles are related via the hydrostatic equation:

$$\frac{dP}{dz} = -\left(\frac{g_0 P}{RT}\right) = -\left(\frac{g_0 P}{R_d T_v}\right) = -\left(\frac{P}{H}\right) \tag{5.10}$$

$R_d$ is the gas constant for dry air ($R_d = 287 JK^{-1}kg^{-1}$), $g_\circ$ is the acceleration due to gravity ($g_\circ = 9.8ms^{-2}$). $T_v$ is a **humidity weighted temperature**, though even at extremely moist, warm conditions $T_v$ exceeds $T$ only by a few degrees (*Wallace and Hobbs*, 1977), thus for most purposes the approximation $T_v = T$ can be made. For a given temperature profile a pressure profile can be determined using an accurate measure

of the surface pressure only:

$$P_2 = P_1 \exp\left(\frac{-\triangle z}{\overline{H}}\right) \tag{5.11}$$

$\overline{H}$ is the mean scale height for the atmospheric layer.

The following numerical integrations for the path and earth centric angle can be written with the trapezium rule:

$$s(l) = \frac{(x_l - x_{l-1})}{2}\left(\frac{n_l^2 r_l^2}{n_l^2 r_l^2 - \gamma_l(r) r_g^2} + \frac{n_{l-1}^2 r_{l-1}^2}{n_{l-1}^2 r_{l-1}^2 - \gamma_{l-1}(r) r_g^2}\right) \tag{5.12}$$

$$\psi(l) = \frac{(x_l - x_{l-1})}{2}\left(\frac{n_l r_g}{n_l^2 r_l^2 - \gamma_l(r) r_g^2} + \frac{n_{l-1} r_g}{n_{l-1}^2 r_{l-1}^2 - \gamma_{l-1}(r) r_g^2}\right) \tag{5.13}$$

These formulae avoid the singularity problems that are associated with the light path passing through a tangent point, and produce a smooth curve for the change in true SZA with apparent SZA (see figure 5.1). These integrations are the basis of the path calculation subroutines.

## 5.2 Rayleigh Scattering

Rayleigh scattering was initially proposed by *Rayleigh* (1871) to explain the blue colour of the sky. Rayleigh scattering describes light elastically scattered by particles, (usually, but not restricted to, molecules) with radii much less than the wavelength of the incident light. In the case where the particles are comparable in size or larger than the incident wavelength Mie theory must be used (see section 5.3). The intensity of Rayleigh scattered light varies with wavelength as $\lambda^{-4}$. Blue skies result from the fact that blue light ($\lambda \simeq 450\,\text{nm}$) is 4.4 times more likely to scatter relative to red light ($\lambda \simeq 650\,\text{nm}$) (*Wayne*, 1991). At twilight the long light paths cause most of the blue light to be preferentially scattered out of the rays with only the longer wavelength red light being left to scatter by the over-head sky.

Rayleigh cross-sections and Rayleigh phase functions from *Bucholtz* (1995) are used to account for the Rayleigh scattering out of the calculated light path and the single scattering into the detector for the zenith-sky geometry. The total Rayleigh scattering cross-section per molecule $\sigma$ is calculated using equation 5.14 where $\lambda$ is expressed in $\mu$m and the values for the parameters are given in table 5.1 (taken from *Bucholtz* (1995)).

$$\sigma_{Ray} = A\lambda^{-(B + C\lambda + \frac{D}{\lambda})} \tag{5.14}$$

The Rayleigh cross-section is multiplied by the number density of air ($N_{air}$) to calculate

| | $\lambda$ | |
|---|---|---|
| Coefficients | 0.2 - 0.5 $\mu$m | $> 0.5$ $\mu$m |
| A | $3.01577 \times 10^{-28}$ | $4.01061 \times 10^{-28}$ |
| B | 3.55212 | 3.99668 |
| C | 1.35579 | $1.10298 \times 10^{-3}$ |
| D | 0.11563 | $2.71393 \times 10^{-2}$ |

**Table 5.1**: Rayleigh Scattering cross-section parameters for the calculation (taken from *Bucholtz* (1995)).

the volume-scattering coefficient (or extinction coefficient):

$$\beta_{Ray}(\lambda, z) = \sigma_{Ray} N_{air} \tag{5.15}$$

The Rayleigh phase function gives the angular distribution of the scattered light which includes the effects of molecular anisotropy (physical properties that vary in a directional fashion) (*Bucholtz*, 1995):

$$P_{Ray}(\theta, \lambda) = \frac{3}{4(1+2\gamma)} \left((1+3\gamma) + (1-\gamma)\cos^2\theta\right) \tag{5.16}$$

where

$$\gamma = \frac{\rho_n}{2-\rho_n} \tag{5.17}$$

$\rho_n$ is the depolarization factor, a unitless wavelength dependent parameter that accounts for the anisotropy of air (typically $4.545\times10^{-2} < \rho_n < 2.730\times10^{-2}$). Figure 5.3 displays the Rayleigh phase function for ($\lambda$=350 nm). The phase function depicted in this figure shows the relative probability of scattering out of the light path for each scattering angle. This plot can be viewed as though the incident light is travelling from right to left in the direction of the 'Angle of Scattering' axis. For example, if light is scattered with a 0° angle (forward scattered) the probability of scattering is greater than if it is scattered at 90°. Phase functions are used to describe the amount of light that is scattered in any given direction. This is important in determining how much light is scattered into the detector (see section 5.6.1). The angular volume scattering coefficient for Rayleigh scattering can be determined as follows:

$$\beta_{Ray}(\theta, \lambda, z) = \frac{\beta_{Ray}(\lambda, z)}{4\pi} P_{Ray}(\theta, \lambda) \tag{5.18}$$

## 5.3 Mie Scattering

When the scattering particles are of comparable size to or greater than the wavelength of incident light, the distribution of the scattered light intensity is more complex than

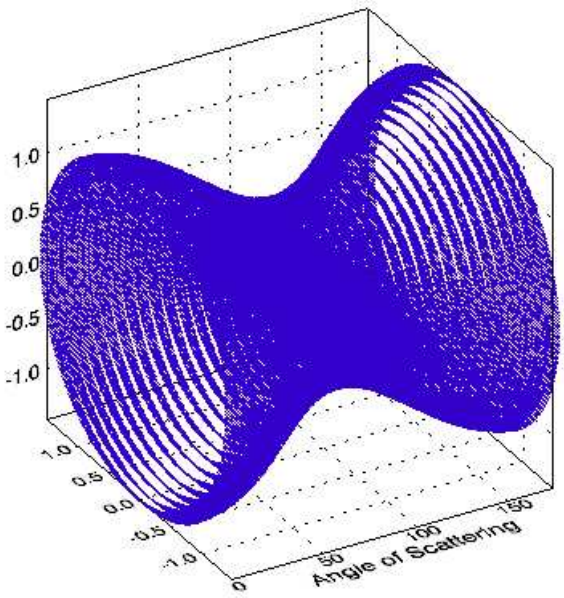


**Figure 5.3**: Rayleigh scattering phase function calculated for $\lambda$=350 nm. The highest probability for scattering is in the forward and backward directions. Scattering perpendicular to the incident light path is least likely.

seen with Rayleigh scattering. Mie scattering (*Mie*, 1908) is invoked in such cases (for a good review of Mie theory and how to evaluate coefficients see *Hansen and Travis* (1974)). In the development of the forward model the incorporation of aerosol scattering is quite simplistic in terms of Mie scattering theory, but adequate for the purposes of modelling clear sky radiative transfer.

Aerosol scattering out of the light path is determined from aerosol extinction profiles combining LIght Detection and Ranging (LIDAR) and aerosol backscatter sonde data (*Liley*, 2003, personal communication). These aerosol measurements give the extinction values directly for aerosol for 500 nm. To determine the extinction at another wavelength these values scale as $\left(\frac{500}{\lambda}\right)^{-1.2}$ giving the volume-scattering coefficient for aerosol scattering $\beta_{Mie}(\lambda, z)$.

The contribution of Mie scattering to the light that is modelled to be received by the detector is approximated using a one parameter Henyey-Greenstein based phase function (*Toublanc*, 1996).

$$P_{HG}(\theta, g) = \frac{1 - g^2}{[1 + g^2 - 2gcos\theta]^{\frac{3}{2}}} \tag{5.19}$$

where g is the asymmetry factor. For spherical particles with an effective radius of 6 $\mu$m g=0.86 over the wavelength range of 300 - 1200 nm (*Bodeker and McKenzie*, 1996). The single scattering albedo for $\lambda$ <1000 nm is very close to 1, indicating that for these wavelengths a negligible amount of absorption occurs when a photon interacts with a

particle and scattering will occur (*Wiscombe et al.*, 1984). Analogous to the Rayleigh

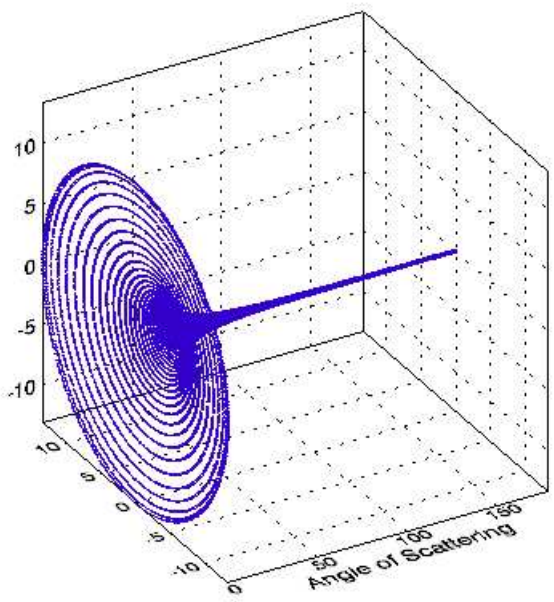


**Figure 5.4**: Mie scattering phase function, the highest probability for scattering is in the forward direction. This is calculated for aerosol particles with an effective radius of 6 $\mu$m for 300 nm$< \lambda <$1200 nm.

equation 5.18, a Mie angular volume-scattering coefficient can be expressed (equation 5.20). This equation is then used to determine the amount of light scattered from a given altitude into the instrument (see section 5.6.1).

$$\beta_{Mie}(\theta, \lambda, z) = \frac{\beta_{Mie}(\lambda, z)}{4\pi} P_{HG}(\theta, g) \tag{5.20}$$

## 5.4 Molecular Absorption

The intensity of received radiation depends on absorption and scattering as described in sections 5.2 and 5.3. Spectroscopy relies on the fact that the absorption features of different molecules have very different signatures. Thus the targeted wavelength region is chosen for its specificity for a given molecule, though it is almost a certainty that other species will absorb in the same wavelength region. Where a species is optically thick ($\tau > 1$) in a given wavelength region, its absorption needs to be considered in the radiative transfer calculation. Optically thin species have a negligible effect on the radiative transfer.

Absorption from the optically thick species ozone is included in the forward model. Ozone profiles for Lauder are obtained from ozonesonde data (*Bodeker et al.*, 1998). This is also the source of temperature and pressure profiles as forward model parameters.

Absorption from $NO_2$ is also included when calculating DSCDs for weaker absorbers. $NO_2$ profiles for Lauder are obtained from SAGE II (*NASA-LaRC*, 2003).

The effects of $NO_2$ and $O_3$ absorption on the calculated BrO DSCDs is negligible. Rayleigh scattering dominates the attenuation of the light intensity along the incident light paths.

## 5.5 Diurnal Variation of Target Species

Spectroscopy in the UV-Visible region is advantageous in the detection of highly reactive species, many of which play critical roles in ozone chemistry. These species are either radical in nature or their concentrations depend directly on radical chemistry. In general their resultant vertical profiles have strong diurnal variations due to photochemistry. The diurnal variation of BrO is displayed in figure 5.5.

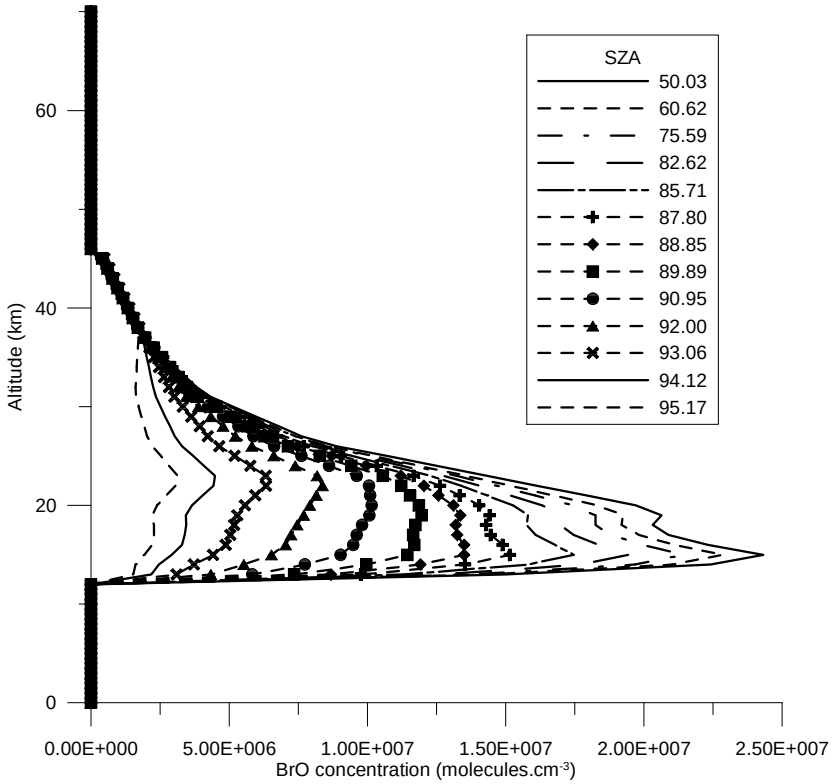


**Figure 5.5**: The diurnal variation of the BrO profile in the stratosphere at a range of SZAs calculated for the sunset on day 254, 2001 at Lauder, New Zealand using a stationary Lagrangian box model (*Kreher et al.*, 2003).

The local SZA $\xi$ (or true SZA) along any given light path decreases from the scattering point to the top of the atmosphere. This effect is most pronounced when the light path passes through a tangent point. For example, if light along a given path scatters at 93°

SZA, it has also sampled absorbers experiencing 90° SZA (at the tangent point) and at the top of the atmosphere the absorbers are experiencing less than 87° SZA. When the absorbing species has a strong diurnal variation the correct concentration associated with each path segment must be used in the calculation of the modelled intensity.

When a path is refracted, the angle of the light path at the top of the atmosphere along with the earth centric angle $\psi$ is required to calculate $\xi$ using simple trigonometry as displayed in the schematic figure 5.6.

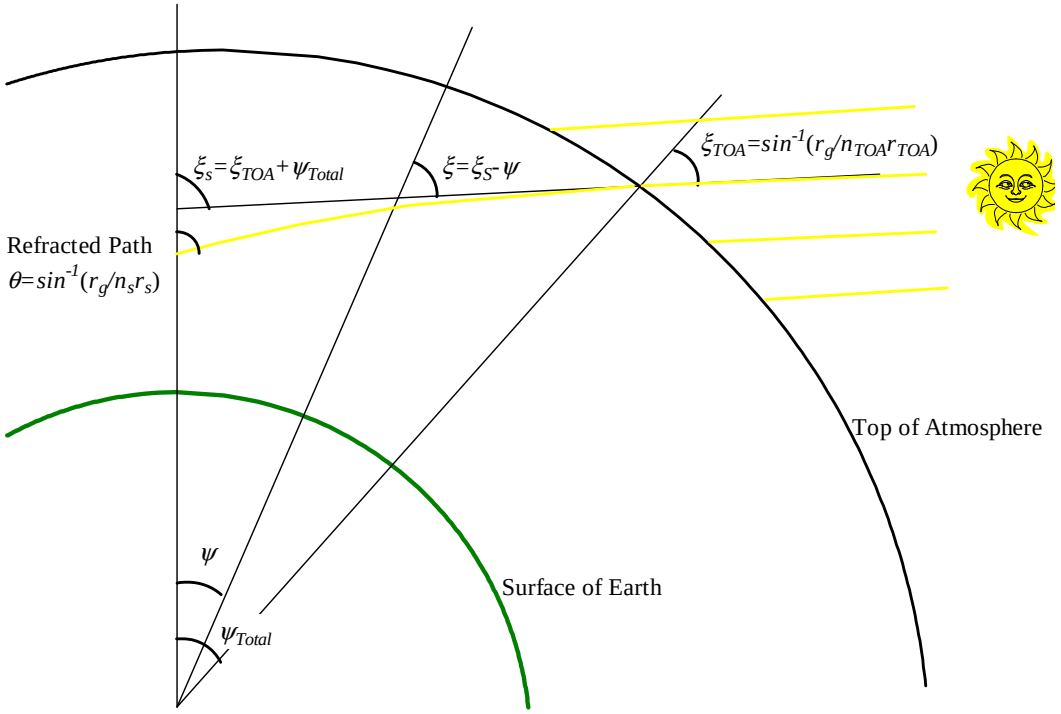


**Figure 5.6**: Schematic diagram illustrating how the local SZA ($\xi$) is determined for each path segment using the earth centric angle ($\psi$) associated with the path. Once $\xi$ is obtained the correct value for concentration of the diurnally variant absorber $N_Y(z,\xi)$ can be found.

Once $\xi$ is determined the correct value for the concentration can be assigned for the diurnally varying absorber. The concentration is then combined with the cross-section to give the extinction coefficient for the relevant model atmosphere layer.

$$\beta_Y(\lambda, z, \xi) = \sigma_Y(\lambda) N_Y(z, \xi) \tag{5.21}$$

The calculation of the extinction due to absorber Y is complicated in the case where Y has a strong diurnal variation. For a tangential path the local SZA associated with the two different passes through the same layer can be very different. Due to the symmetry about the tangent point, $\beta_Y$ for these layers is the average of the two different absorber

concentrations. The absorber extinction coefficient is calculated as:

$$\beta_Y(\lambda, z, \xi) = \sigma_Y(\lambda)\frac{N_Y(z, \xi_1) + N_Y(z, \xi_2)}{2} \tag{5.22}$$

## 5.6 Slant Column Density Calculations

The SCD measured is the number of molecules of an absorbing species that is detected after the radiation has travelled through the atmosphere. To model this in the case of diffuse light, when the light has travelled many different paths before being detected, there are two approaches. The exact method for evaluating the SCDs and the approximation of this method called the 'intensity weighting approximation' are discussed in the following sections.

### 5.6.1 The Exact Method

Beer-Lambert's Law gives the following formula to describe the intensity of light after it has traversed through a medium (here the atmosphere) containing an absorber Y:

$$I = I^* \exp(-\sigma_Y N_Y s) \tag{5.23}$$

Where $N_Y$ is the concentration of the species, $\sigma_Y$ is the cross-section of the species of interest and s is the optical path traversed by the light sampled by the detector. $I$ is the intensity of light received at the detector with Y present, and $I^*$ without Y present in the medium being studied. It is feasible to measure these directly using laboratory based spectroscopy, where the medium can be altered to suit, but in the atmosphere this can be more challenging. In terms of modelling the intensity that is received by the detector, an infinitely narrow field of view is assumed. Thus the integration becomes a summation of the intensity contributions from scattering from all the different altitudes (z) in the line of sight of the detector (*Sarkissian et al.*, 1995b).

$$I = I_o \sum_{z=0}^{N} \left(\beta_{Ray}(\theta, \lambda, z) + \beta_{Mie}(\theta, \lambda, z)\right) \exp^{-\tau(z)} \triangle z \tag{5.24}$$

Where $I_o$ represents the arbitrary intensity before absorption has taken place (chosen to be 1 in this work). The optical density $\tau$ for a single light path scattered from an altitude $z$ is defined as the following summation over all of the model atmospheric layers ($l$) as:

$$\tau(z) = \sum_{l=0}^{N} \left( \sum_{Y} \beta_Y(\lambda, l, \xi) + \beta_{Ray}(\lambda, l) + \beta_{Mie}(\lambda, l) \right) s(l, z) \tag{5.25}$$

The path $s(l,z)$ for a given scattering altitude $z$ through a model atmospheric layer $l$ takes into account that below the scattering altitude the light path either passes vertically through the layer or the light path goes through a tangent point. $s(l,z) = \triangle z$, the layer width, for the vertical path case. Where the path is tangential, it is symmetric about the tangent point, passing through all layers twice below the scattering altitude to, but not including, the tangent layer.

The SCD $\phi_Y$ is then calculated using a rearrangement of Beer's law equation 5.23 with I and I$^*$ calculated using equations 5.24 and 5.25.

$$\phi_Y = \frac{1}{\sigma_Y}\left(-\ln\left(\frac{I}{I^*}\right)\right) \tag{5.26}$$

The evaluation of $I$ and $I^*$ differ in the summation given by $\beta_Y(\lambda, l, \xi)$ in equation 5.25. $I$ is the intensity integral over all absorbers and $I^*$ is the intensity integral over all absorbers except the absorber of interest. The measurement $\mathbf{y}$ however is not the SCD but the DSCD. The DSCD is the SCD less the SCD at some reference angle, usually when there is little or none of the absorber present (or when the absorbance is low, e.g. a noon SZA). Then the DSCD is evaluated as $\triangle\phi = \phi - \phi_R$.

### 5.6.2 Intensity Weighted Approximation

The intensity weighted approximation evaluates the SCD by weighting each light ray with its respective contribution to the total intensity that reaches the detector (*Solomon et al.*, 1987).

$$\phi_Y = \frac{\sum_z I_z N_Y s}{\sum_z I_z} \tag{5.27}$$

where $I_z$ is the intensity calculated for a single ray. The denominator $\sum_z I_z$ is equivalent to $I$ calculated by equation 5.24. $\tau(z)$ is evaluated using equation 5.25.

$$I_z = I_o\left(\beta_{Ray}(\theta,\lambda,z) + \beta_{Mie}(\theta,\lambda,z)\right)\exp^{-\tau(z)}\triangle z \tag{5.28}$$

The SCD evaluated using the intensity weighted approximation (equation 5.27) equals the more exact method (equation 5.26) only at the limit of weak absorption when $\tau \ll 1$ (*Sarkissian et al.*, 1995b). To study optically thick species this approximation should not be made and is easily avoided using equation 5.26.

### 5.6.3 Multiple Scattering

Multiple scattering has the greatest implications for the radiative transfer of the troposphere. The atmospheric air density is largest in the troposphere, hence the probability of scattering is greatest. As Rayleigh scattering scales as $1/\lambda^4$, the shorter wavelengths have

a higher probability of scattering. The altitude at which most of the detected light is being scattered from increases with increasing SZA and decreasing wavelength. Hence multiple scattering is most important for the determination of SCDs of tropospheric absorbers, short wavelengths and large SZA ($> 88°$). The SCD determination for stratospheric absorbers is relatively insensitive to the effects of multiple scattering, with most zenith-sky scattered light being singly scattered from the stratosphere (*Perliski and Solomon*, 1993).

In modelling the BrO zenith-sky DSCDs at $\lambda = 350\,\text{nm}$ the effects of neglecting multiple scattering had to be considered. Absolute SCDs are underestimated by $\sim 15\,\%$ by making a single scattering approximation in the radiative transfer calculation (see figure 5.8). Zenith-sky DSCDs of BrO are found to have only a second-order response to the inclusion of both multiple scattering and a tropospheric absorption component in the radiative transfer (*Sinnhuber et al.*, 2002). In this study *Sinnhuber et al.* (2002) found by taking the differential any tropospheric quantity or multiple scattering effects are essentially removed. *Sinnhuber et al.* (2002) also found the inclusion of aerosol scattering had a greater impact in the modelling of zenith-sky DSCDs for BrO. Thus a single scattering approximation for the modelling of cloud free zenith-sky DSCDs is considered reasonable.

## 5.7 Weighting Function Calculation

The weighting function matrix $\mathbf{K}$ gives the sensitivity of the DSCDs to changes in the state. $\mathbf{K}$ is determined by perturbing each state vector quantity, and then calculating the resultant change in each of the calculated DSCDs. The calculation of $\mathbf{K}$ is the most computationally expensive part of the retrieval.

$$\mathbf{K} = \frac{\delta F}{\delta \mathbf{x}} \tag{5.29}$$

The weighting functions for perturbing the state vector components for the 75°, 84° and 87° SZA profiles are displayed in 5.7 for both the direct-sun and zenith-sky measurements. Note that the two measurement modes have very different sensitivities to the three diurnal BrO profiles. The weighting functions are calculated for the illustrative case study day 254, 2001 at Lauder.

Perturbing the 75° SZA state vector profile leads to a negative sensitivity for high SZA measurements in both the direct-sun and zenith-sky cases. This is due to the fact that the measurements are differential with respect to the lowest measurement of each mode. Reference SZAs of 62° and 63° are used for the zenith-sky and direct-sun cases respectively in this example. For example, the resultant change in the 86.13° zenith-sky DSCD to a perturbation at any altitude of the 75° state profile is less than the resultant change in the reference SCD for 62.13°.

The zenith-sky DSCDs display the highest sensitivities to perturbations in the stratosphere for all three state profiles. In contrast the direct-sun weighting functions display a tropospheric sensitivity. The interesting shape of the direct-sun weighting functions for the 84° profile perturbations illustrates nicely where along a given measurement path the perturbation has the most influence. It is clear that the measurement sensitivities are very different for each of the three state vector profiles. To retrieve only one of these with an *a priori* assumed diurnal variation leads to complex and unusual features in the weighting functions. These features propagate as errors into the retrieved quantities.

Efficiency in the calculation of $\mathbf{K}$ is achieved by only recalculating the $\beta_Y(\lambda, z, \xi)$ for altitudes ($z$) and local SZA ($\xi$) which are affected by the change in $\mathbf{x}$. The measurement vector $\mathbf{y}$ in the retrieval algorithm is constructed using the direct-sun measurements to make up the first $m_1$ values, then the zenith-sky measurements make up the subsequent $m_2$ values in the vector (see section 6.3). As $\mathbf{K}$ describes the sensitivity of each measurement to changes in the state level $n$, it is constructed similarly with the direct-sun weighting functions preceding the zenith-sky weighting functions.

Further measurement platforms could be added to the basic structure of a retrieval displayed in figure 6.1 if a means of modelling the measurements and determining their weighting functions is integrated into the forward model. The multiple-axis viewing geometry for example could provide additional information about BrO columns at noon SZAs. There is a large computational expense associated with calculating weighting functions that account for the multiple-scattering inherent in this geometry. A means of minimizing this would be necessary to allow the multiple axis geometry measurements to be included.

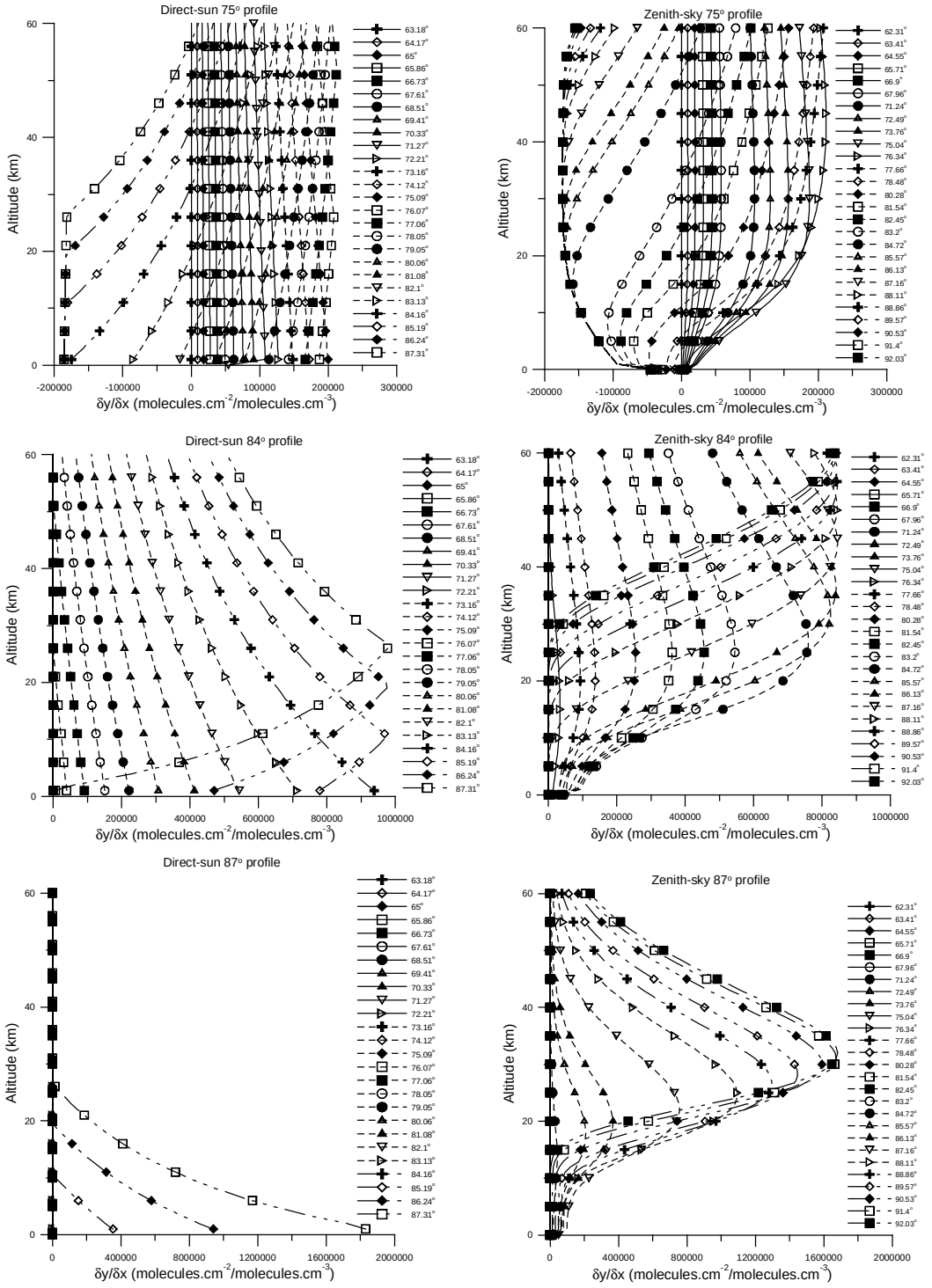


**Figure 5.7**: Weighting functions for direct-sun (left panels) and zenith-sky (right panels) resulting from perturbations in the 75° SZA state vector profile (top). The 84° SZA state vector profile is displayed in the middle and 87° SZA state vector profile at the bottom. These weighting functions are calculated for measurements taken on day 254, 2001 at Lauder. It can be clearly seen that the measurements, both comparing between the measurement modes and within one measurement mode, have very different sensitivities for the three diurnal state vector profiles.

## 5.8 Validation of Forward Model

A validation exercise was performed to ensure that the forward model developed here in this thesis produced similar results to other radiative transfer models in use. This intercomparison exercise was held as part of the European funded Quantification and Interpretation of Long-Term UV-Visible Observations of the Stratosphere (QUILT) project. The groups involved were IASB-BIRA (Brussels, Belgium), NILU (Kjeller, Norwary), UHB (Bremen, Germany), U-Heidelberg (Heidelberg, Germany), ISAC-CNR (Bologna, Italy), NERC (Cambridge, England), and NIWA (Lauder, New Zealand). The radiative transfer models examined in this workshop were developed for different purposes. The workshop focused on testing the consistency between the different models.

The radiative transfer model developed here was involved only in the single scattering comparison exercise. Calculations of the BrO, OClO, and $NO_2$ SCDs in zenith-sky geometry including photochemistry were made. For the exercise BrO, OClO, and $NO_2$ diurnal variation matrices, $O_3$, $NO_2$, pressure and temperature profiles were provided. Model parameters were defined on an altitude grid of 0-120 km with 1 km layer thickness. Fixed wavelengths of 352 nm (BrO), 368 nm (OClO), and 422 nm ($NO_2$) were used. Where appropriate a fixed ground albedo value of 0.20 was used. Cross-sections for all absorbers were also fixed. Aerosol scattering and refraction were not included. Calculations in single scattering (SS) mode and multiple scattering (MS) mode were made if possible.

The upper plots of figure 5.8 displays the calculated SCDs from the different radiative transfer models for BrO, $NO_2$ and OClO. For all three of these SCD calculations the NIWA model overlays the SCDs determined by the NILU and IASB single scattering models. The lower plots display the ratio with respect to the IASB models, this illustrated that the agreement between the NIWA, NILU and IASB models was within 3 % for all the three species investigated. The high agreement between the NILU and IASB groups is due largely to the use of the same UVspec/DISORT package (*Stamnes et al.*, 1988). DISORT is a discrete ordinate radiative transfer model. It is the most flexible and widely used pseudo-spherical plane-parallel model available to the atmospheric community. The intensity calculation solves the radiative transfer equation using a scattering formalism. The composition and detailed physics of the medium is not necessary. Optical depths, single scattering albedos and phase function moments are all that is required (*Spurr et al.*, 2001).

The effect of multiple scattering is also displayed in figure 5.8. Multiple scattering increases the calculated SCD by 10 - 15 %, at all SZAs, acting like an offset.

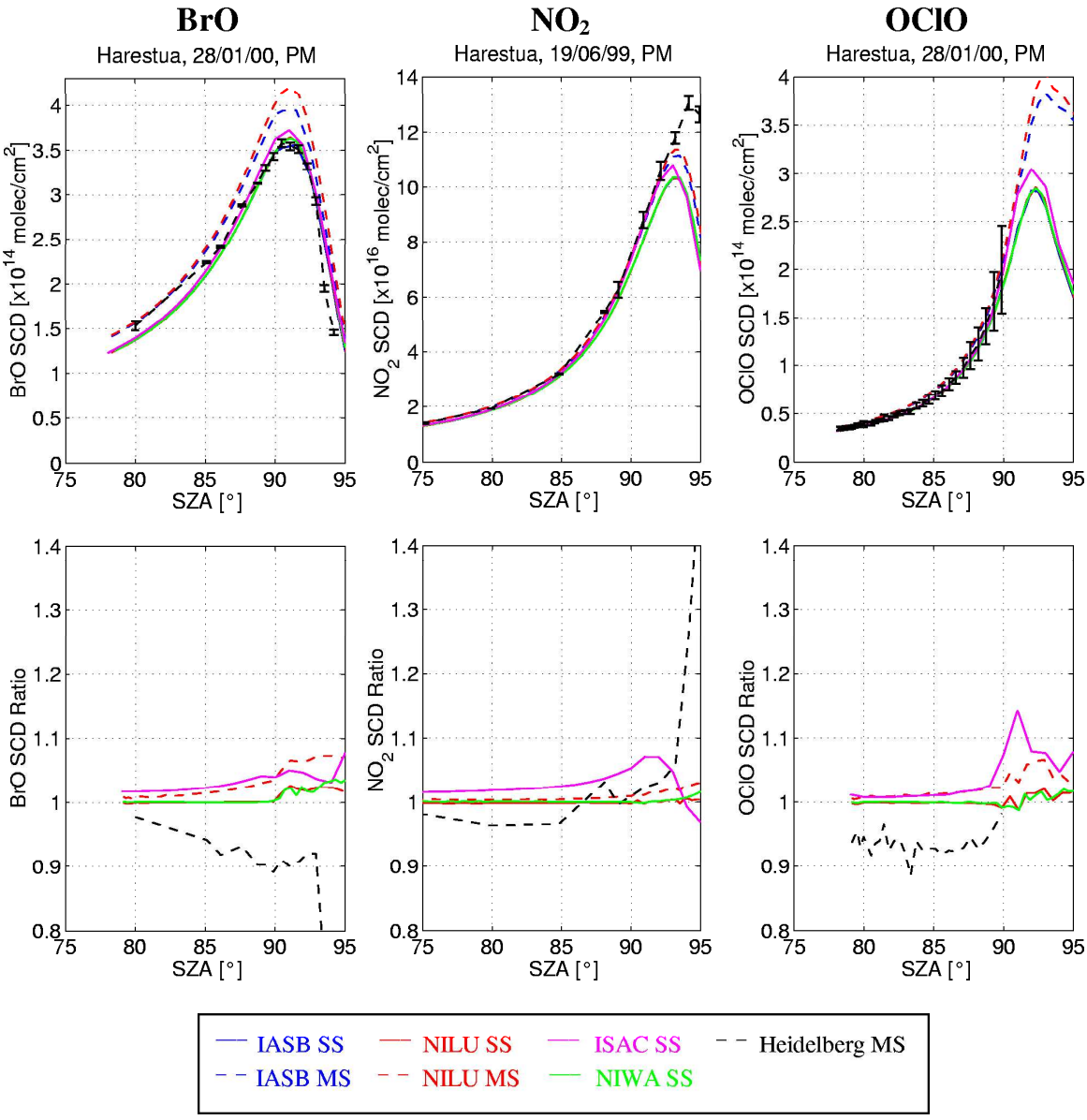


**Figure 5.8**: BrO, $NO_2$, and OClO SCD calculations are compared between groups participating in the European QUILT project. These groups included IASB (Brussels, Belgium), NILU (Kjeller, Norway), U-Heidelberg (Heidelberg, Germany), ISAC-CNR (Bologna, Italy), and the model developed by this work NIWA (Lauder, New Zealand). SS denotes single scattering model calculations and MS multiple scattering calculations. The upper plots are corresponding to the SCDs and the lower plots to the ratios between results from the different models and the IASB model arbitrarily taken as the reference model. Two different scenarios have been considered: Harestua (Norway, 60°N) in summer ($NO_2$) and in winter when chlorine activation occurs (BrO and OClO). Solid and dashed lines are corresponding to calculations in SS and MS modes, respectively (*Hendrick*, 2003, personal communication).

## Chapter 6

# Retrieval Model

Remote sensing techniques often have the disadvantage that what is being measured has a complex relationship with what is desired to be known. Optimal estimation is a retrieval method that allows the inversion of 'measurements' $\mathbf{y}$ ($\triangle\phi$) (Chapter 4) into the desired state $\hat{\mathbf{x}}$, in this instance a set of profiles at different diurnal stages. For a given state $\mathbf{x}$ a forward model must describe the expected $\triangle\phi$. This is the radiative transfer part of the algorithm (see Chapter 5). A detailed description of retrieval concepts is given by *Rodgers* (1976, 1990, 2000). The basic structure of the retrieval algorithm used in this work is displayed by figure 6.1, illustrating how complementary sets of measurements are combined. This chapter discusses the expressions and terms used in the retrieval model algorithm and is the basis of the paper *Schofield et al.* (2003). The formulation and notation used here follows *Rodgers* (2000) conventions. A exemplary retrieval was performed for day 254, 2001 over Lauder, to illustrate the concepts of retrieval characterisation. An algorithm was developed in IDL© in this work to characterise the retrieval with averaging kernels, resolution, area, degrees of freedom for signal and information content.

## 6.1 Linear Inversion

A linear inversion is the most simple and relies on the sensitivity of the measurements to the state being independent of the state. If the sensitivity of the forward model to changes in the state ($\mathbf{K}$) is sensitive to the state, the problem is said to be non-linear in nature. The measurements considered in this work are in optically thin spectral regions and have a linear dependence on the profile of the trace gas. For a species to be optically thin, the calculated optical depth $\tau$ must be much smaller than one. The optical depth calculation depends on the path geometry of the measurement. It also requires the extinction coefficients for Rayleigh and Mie scattering, and the absorbing species. For linear problems the weighting function matrix is independent of the state. Species that are optically thick influence the intensity, hence $F$, in a non-linear fashion (refer to Chapter 5 for forward model details). If this general retrieval technique is applied to retrieve profile information for a species that is optically thick, then a non-linear retrieval will be necessary.

Inversion of the DSCD measurement vector $\mathbf{y}$ is performed using the following formula

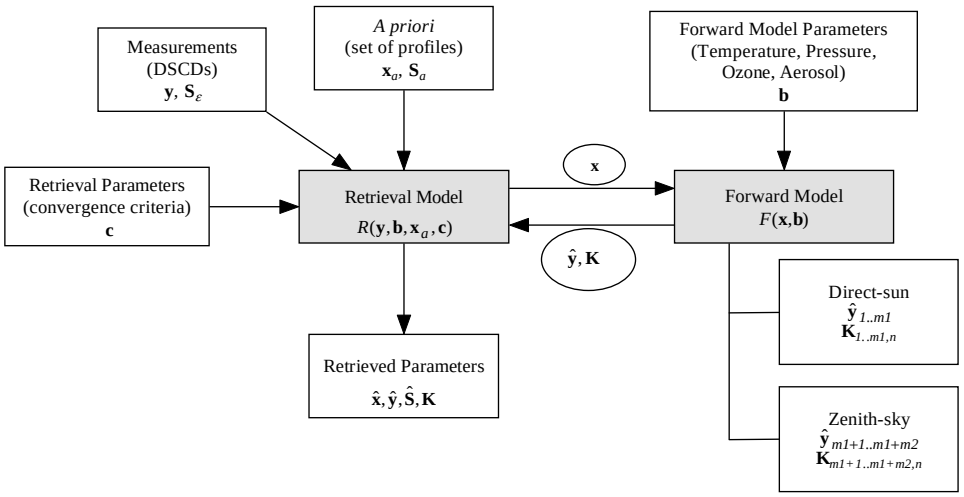


**Figure 6.1**: A schematic diagram displaying the basic structure of the retrieval algorithm. The inputs that are necessary and how the forward model and inverse models can be effectively separated is clearly shown.

for a linear problem (*Rodgers*, 2000):

$$\hat{\mathbf{x}} = \mathbf{x}_a + \mathbf{S}_a\mathbf{K}^T(\mathbf{K}\mathbf{S}_a\mathbf{K}^T + \mathbf{S}_\epsilon)^{-1}(\mathbf{y} - \mathbf{K}\mathbf{x}_a) \tag{6.1}$$

where $\mathbf{x}_a$ is the *a priori* of the state, $\mathbf{S}_a$ is the covariance of the *a priori* and $\mathbf{S}_\epsilon$ is the measurement covariance. These terms are discussed in sections 6.3 and 6.4.

## 6.2 Non-Linear Inversion

The retrieval of profile information for an optically thick species requires a non-linear retrieval. The error due to ignoring the non-linearity in a retrieval problem is given by $\delta\hat{\mathbf{x}}$:

$$\delta\hat{\mathbf{x}} = \mathbf{G}_y(F(\hat{\mathbf{x}}) - F(\mathbf{x}_a) - \mathbf{K}(\hat{\mathbf{x}} - \mathbf{x}_a)) \tag{6.2}$$

Where $\mathbf{G}_y$ is the Gain matrix defined by equation 6.6.

A Gauss-Newtonian iteration linearizes the problem in the case where the problem is slightly non-linear, and then iterates to find the solution. If the retrieval problem is non-linear in nature (the error $\delta\hat{\mathbf{x}}$ is too large and equation 6.1 cannot be used) the following iterative Gauss-Newtonian expressions are used to evaluate the retrieved state. The non-linear expressions are given as the deviation of the $\mathbf{x}_{i+1}$ from the *a priori* $\mathbf{x}_a$. $\mathbf{x}_i$ tends to $\hat{\mathbf{x}}$ as $i$, the number of iterations, increases. Equation 6.3 gives the 'n-form' for the Gauss-Newtonian iterative expression solving the $n \times n$ matrix equation, where n is the number of state vector quantities. This is effectively a non-linear weighted least squares solution to the problem. This method is chosen for situations where the number

of state vector quantities is much smaller than the number of measurements (m).

$$\mathbf{x}_{i+1} = \mathbf{x}_a + (\mathbf{S}_a^{-1} + \mathbf{K}_i^T \mathbf{S}_\epsilon^{-1} \mathbf{K}_i)^{-1} \mathbf{K}_i^T \mathbf{S}_\epsilon^{-1} (\mathbf{y} - F(\mathbf{x}_i) + \mathbf{K}_i(\mathbf{x}_i - \mathbf{x}_a)) \tag{6.3}$$

In the case where the number of state vector quantities is much larger than the number of measurements an alternative inversion called the 'm-form' can be used (equation 6.4). The 'm-form' is the more computationally efficient form as only one matrix inversion is required compared to the four necessary when using the 'n-form'. A method called 'sequential updating' can be invoked when using the 'm-form' to give further efficiency; this allows the state estimate to be updated one measurement at a time. This was the method chosen by *Preston* (1995) for the inversion of $NO_2$ DSCDs to give a $NO_x$ profile.

$$\mathbf{x}_{i+1} = \mathbf{x}_a + \mathbf{S}_a \mathbf{K}_i^T (\mathbf{K}_i \mathbf{S}_a \mathbf{K}_i^T + \mathbf{S}_\epsilon)^{-1} (\mathbf{y} - F(\mathbf{x}_i) + \mathbf{K}_i(\mathbf{x}_i - \mathbf{x}_a)) \tag{6.4}$$

Both these iterative methods for evaluation of the retrieved state requires $\mathbf{K}$ to be re-calculated at each iteration, thus making it much more demanding on computer resources than the linear case. Any gain in numerical efficiency by choice of Gauss-Newtonian 'n-form' or 'm-form' to suit the DOAS problem is by far outweighed by the computational expense of the $\mathbf{K}$ calculation.

In this retrieval algorithm it is actually the 'n-form' non-linear equation that is used, due solely to historical reasons. In infrared and microwave retrieval algorithms this is the equation chosen. These retrieval problems are non-linear and the 'n-form' of the Gauss-Newtonian iterative method can be chosen for efficiency in these problems (equation 6.3) (*Connor et al.*, 1995). Since the evaluation of $\mathbf{K}$ dominates the computer resources there was no advantage in using another formulation. BrO is a weak absorber and therefore it is actually a linear retrieval problem, therefore the use of a non-linear equation is surplus to requirements. As this is a general algorithm and the desire is that it can be used for all absorbers the non-linear equation is used, and for the case where the problem is linear, convergence occurs after one iteration.

## 6.3 Measurements and Covariance

Inversion algorithms can use the intensity measurements from the detectors directly in construction of the measurement vector $\mathbf{y}$. These measurements are a function of wavelength and the measurement vectors may be huge. The magnitude of these type of retrievals make them quite complex.

It is common for some spectroscopic measurements to be reported as line of sight DSCD measurements, the product of spectral fitting (refer to Chapter 4). DSCD are evaluated from the intensity using a non-linear least squares fit, so essentially have already undergone

a retrieval (see section 4.3). It is these 'preprocessed' quantities that are defined as the measurements used in this retrieval algorithm.

The measurement vector $\mathbf{y}$ in the retrieval algorithm is constructed using the direct-sun measurements to make up the first $m_1$ values, then the zenith-sky measurements make up the subsequent $m_2$ values in the vector (see figure 6.1).

The covariance matrix of the uncertainties in the measurements, $\mathbf{S}_\epsilon$, is constructed by placing the variance arising from one standard deviation of the error from the DOAS spectral fitting along the diagonal of the $\mathrm{m} \times \mathrm{m}$ matrix. The off-diagonal elements are assumed to be zero. The measurement error covariance matrix $\mathbf{S}_\epsilon$ from the DOAS fitting is assumed to incorporate all the errors that are present in determining the DSCDs.

## 6.4 *A Priori* Information and Covariance

Profile retrievals involving ozone and $\mathrm{NO_x}$ (a quantity that doesn't have a diurnal variation) avoid the complications that arise due to the strong diurnal variation such as is typical of radical or radical-like trace gas species (NO, $\mathrm{NO_2}$, IO, OClO, BrO etc) involved in photochemical cycles. This work explores the complications and errors arising from diurnal variation when incorporated in the retrieval of altitude information.

There are two approaches that allow the retrieval of profiles of diurnally varying trace gases. The first approach is to assume that the chemistry is known *a priori* from chemical models and that a single profile varies in a predetermined way, for example as a scalar multiple or a more complex change of profile shape. The diurnal variation is thus being treated as a forward model parameter (see section 5.5). The retrieval errors associated with this approach are explored below. However, the main concern with this approach is that while existing chemical models explain diurnal variations for the stratosphere (i.e. SLIMCAT (*Chipperfield et al.*, 1993; *Sinnhuber et al.*, 2002)), tropospheric diurnal variations are essentially unknown and an area of active research. Assuming diurnal variation from stratospheric models alone causes discontinuity in the weighting functions at the troposphere-stratosphere boundary. Consequently this produces errors in the final retrieved state.

The second possible method, used here to account for the diurnal variation of the species, is to retrieve it. Sets of profiles defined on a time (or SZA) grid, to describe the diurnal variation of the species, are retrieved. Thus the *a priori* $\mathbf{x}_a$ supplied to the retrieval model is a set of profiles, not just one profile. This does lead to an increased number of retrieved parameters but avoids the problems associated with assuming the diurnal variation as a forward model parameter and allows direct comparison with chemical models. The degrees of freedom for the signal and information content that characterise the retrieval both improve employing this second method. This is due to the fact that

less knowledge is being assumed initially so more can be learnt from the measurements.

The *a priori* profiles include a profile at 0°. This is necessary as the measurements made at one location sample the atmosphere at a previous time or lower SZA at the top of the atmosphere. The retrieval of this profile is not meaningful, having a heavy reliance on the initially supplied *a priori* information. It can be thought of as a noon profile.

The construction of the *a priori* covariance $\mathbf{S}_a$ is not straightforward. If the equation is to be used formally as an optimal estimator, then $\mathbf{S}_a$ describes whatever is known about the state (*a priori* knowledge), however little. In principle the best that can be done for a case taken at random from some ensemble of profiles is to use the ensemble covariance. If no ensemble is available then care is needed.

### 6.4.1 L-Curve Optimization

The use of $\mathbf{S}_a$ as a tuning parameter means that the retrieval is formally non-optimal, but it provides a convenient means of determining where the retrieval should be run to give the maximum information and minimum error. The variances used in the construction of this diagonal matrix can be optimized such that the most information can be retrieved from the measurements without over-fitting them (i.e. mapping measurement errors into the retrieved state). Assuming low values in the construction of the $\mathbf{S}_a$ matrix implies low error in the *a priori* for the state ($\mathbf{x}_a$), with the result that the retrieval is heavily reliant on this *a priori* with the information from the measurements being largely ignored. Conversely an assumed high error in the construction of $\mathbf{S}_a$, results in the *a priori* being ignored and the retrieval being an unrealistic over-interpretation of the measurements. To determine an appropriate *a priori* error is complicated. It should be large enough that the measurements are fitted well, yet small enough that the retrieved values are not oscillatory or otherwise unrealistic. In this work, a percentage of the peak for each of the temporal profiles is used as a conservative estimate of the *a priori* variance. The value of this percentage is determined by an l-curve method. The percentage is varied from a very low value (tightly constrained) to a very high value (loosely constrained). A plot of the root mean square of the retrieval fit to the measurements versus this percentage is constructed (see figure 6.2). The percentage chosen is the value where increasing the *a priori* error no longer results in a marked improvement of the measurement fit.

## 6.5 Retrieval Parameters

As displayed in figure 6.1 the retrieval model requires retrieval parameters $\mathbf{c}$. When the problem is non-linear the convergence criterion is a retrieval parameter that is necessary. The equations 6.3 and 6.4 for the inversion in the non-linear case allow for $\mathbf{x}_{i+1} - \mathbf{x}$ to be used as a convergence criterion.

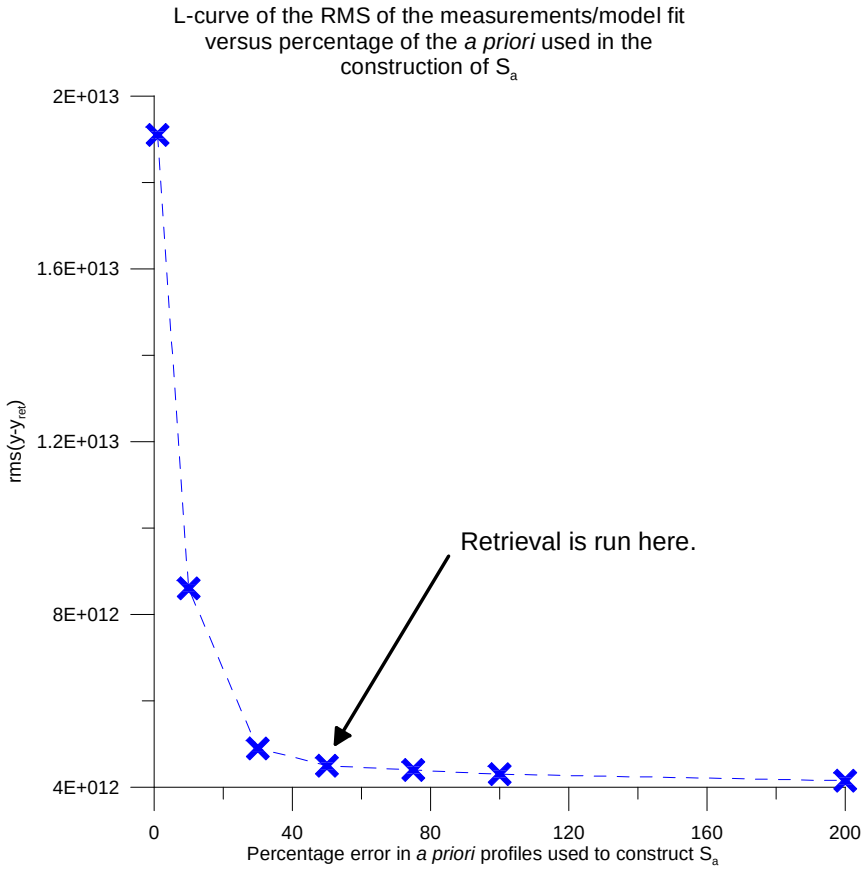


**Figure 6.2**: The L-curve for the profile retrieval from measurements made at Lauder on day 254, 2001. $\mathbf{S}_a$ is adjusted to ascertain a error which obtains the maximum amount of information from the measurements without mapping their errors into the retrieval.

The change in the state between iterations transformed into the space of the measurements must at all values be some fraction of the measurement error. A tolerance value $\delta$ is used to define this fraction.

$$\mathbf{K}_{i+1}(\mathbf{x}_{i+1} - \mathbf{x}_i) \leq \delta\sigma_\epsilon \tag{6.5}$$

where the squared values of $\sigma_\epsilon$ make up the diagonal elements of the measurement covariance matrix $\mathbf{S}_\epsilon$.

## 6.6 Error Analysis and Characterisation

Optimal estimation allows a solution to be found that minimizes the differences between the measured and modelled DSCDs, given their errors, the *a priori* information and its associated errors.

An optimal estimation retrieval is used to obtain the best solution from a set of all possible solutions for the case where the problem is ill posed. The retrieval problem

here is formally ill posed, as there are more elements in the state vector than there are measurements. There is an infinite set of solutions and the *a priori* constraint allows a single solution to be determined. The *a priori* is important to provide a best estimate of components of the state vector for which the measurements provide no information, i.e. in the null space and near-null space of the retrieval problem. The 0° profile of BrO retrievals performed here is in the near-null space of the retrieval problem. This is because DSCDs remove almost all information about the 0° profile, thus it is not well sampled by the measurements.

### 6.6.1 Gain Matrix - Contribution Functions

The Gain matrix ($\mathbf{G}_y$) describes how changes in the measurements affect the retrieved state. The contribution functions illustrate how each measurement contributes to the final retrieval. The Gain matrix is calculated from the weighting function and covariance matrices, for its derivation refer to *Rodgers* (2000).

$$\mathbf{G}_y = \frac{\delta \hat{\mathbf{x}}}{\delta \mathbf{y}} = (\mathbf{K}^T \mathbf{S}_\epsilon^{-1} \mathbf{K} + \mathbf{S}_a^{-1})^{-1} \mathbf{K}^T \mathbf{S}_\epsilon^{-1} \tag{6.6}$$

The contribution functions are extremely complex in this instance as figure 6.3 displays. How each measurement influences the final retrieved state cannot be clearly separated into direct-sun and zenith-sky components using the contribution functions. The averaging kernels discussed in section 6.6.2 address this question more completely.

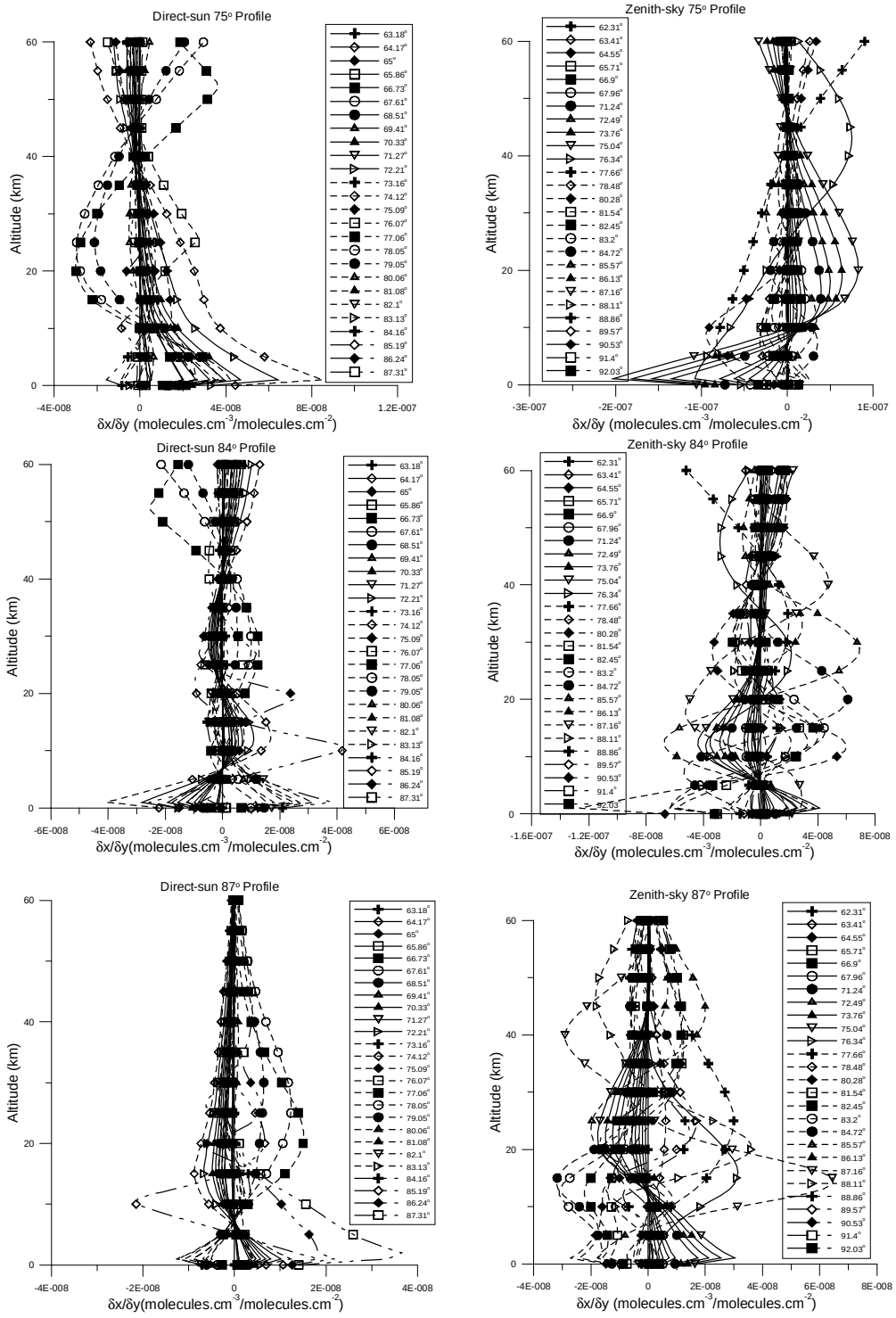


**Figure 6.3**: Contribution functions for direct-sun (left panels) and zenith-sky (right panels). The response of the 75° SZA state vector profile (top). The 84° SZA state vector profile is displayed in the middle and 87° SZA state vector profile at the bottom. These contribution functions are calculated for measurements taken on day 254, 2001 at Lauder. The contribution functions illustrate how each measurement contributes to the final retrieved state.

### 6.6.2 Averaging Kernel Matrix

Analysis of the smoothing of the true state by the retrieval is essential to understanding what information can be obtained from a set of measurements. The smoothing functions or averaging kernels are vital in the charactization of a retrieval. The averaging kernel matrix ($\mathbf{A}$) describes the sensitivity of the retrieved state ($\hat{\mathbf{x}}$) to the true state ($\mathbf{x}$). The averaging kernel matrix is calculated from the weighting function and gain matrices.

$$\mathbf{A} = \frac{\delta \hat{\mathbf{x}}}{\delta \mathbf{x}} = \mathbf{G}_y \mathbf{K} = (\mathbf{K}^T \mathbf{S}_\epsilon^{-1} \mathbf{K} + \mathbf{S}_a^{-1})^{-1} \mathbf{K}^T \mathbf{S}_\epsilon^{-1} \mathbf{K} \tag{6.7}$$

The rows of $\mathbf{A}$ are the averaging kernels and these indicate how the retrieved state represents the true state.

The averaging kernels produced by this retrieval method are not only a function of altitude but also of profile or time (SZA). Each element of the state vector has an averaging kernel that is two-dimensional. So while it is possible to view the averaging kernels in a traditional altitude sense, their variation in the space of profiles (time sense) should also be considered, thus they are best seen as two-dimensional. Contour plots are used to view the averaging kernels and derived quantities such as resolution and area. While contours give the impression of continuity, the values are discrete in both space and time.

Figure 6.4 displays the averaging kernels for the 0 km, 10 km, 20 km, 30 km, and 40 km retrieval points of the 84° profile. The black crosses indicate the retrieval points that each of the averaging kernels represent. Ideally the averaging kernel will be focused on this point. The averaging kernels shown in figure 6.4 illustrate clearly how the retrieval is improved by combining measurement geometries. The averaging kernels of the direct-sun only retrieval illustrate how these measurements are sensitive to the lower altitudes. Conversely, the zenith-sky only retrieval demonstrates this geometry to be more sensitive to the stratosphere. The combination of the two geometries provides enhanced sensitivity over all altitudes.

### 6.6.3 Area of Averaging Kernels

The area of an averaging kernel gives a qualitative indication of the influence of the *a priori* on the retrieved state. The area of an averaging kernel is the sum of the elements in that averaging kernel. When the area is approximately unity then most of the information on a spatial scale greater than the width of the averaging kernel is being supplied by the measurements rather than the *a priori*. When the area is close to zero then the retrieved value has come from the *a priori* information and the measurements have not added any information.

Figure 6.5 shows the area of the averaging kernels that characterise the direct-sun

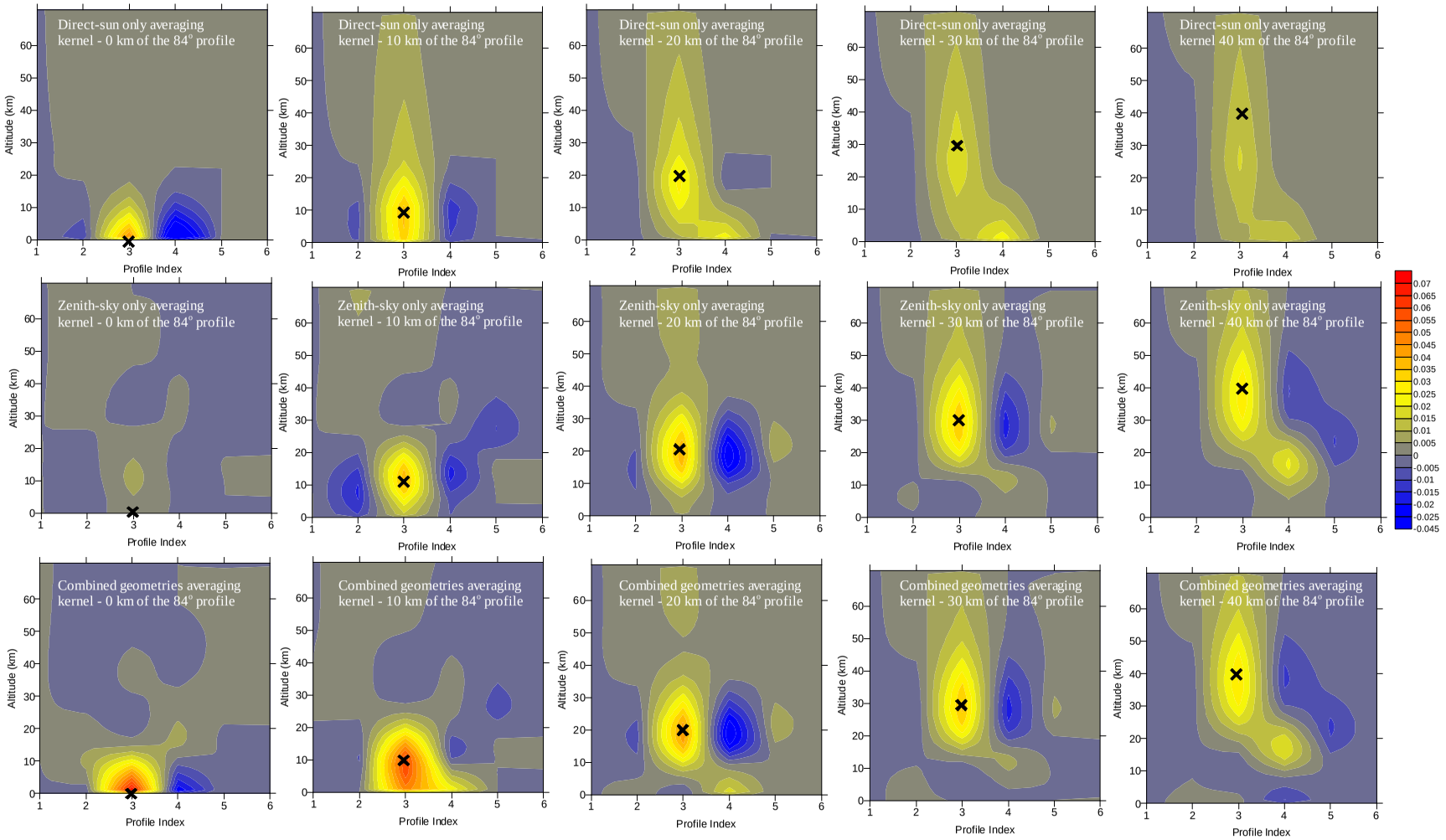


**Figure 6.4**: Averaging kernels in altitude space (y axis in km) and profile space (x axis) for the BrO profiles. The profile index refers to the solar zenith angle corresponding to the profile: 1=0°, 2=75°, 3=84°, 4=87°, 5=92° and 6=95°. These averaging kernels are calculated for measurements made on day 254, 2001 at Lauder. The measurement range for the direct-sun viewing geometry is 63.2° to 87.3° and for the zenith-sky viewing geometry is 62.3° to 92.0°. The middle panels display the averaging kernels for a retrieval using only the direct-sun measurements and the lower panels display the averaging kernels for a retrieval using only the zenith-sky measurements. The upper panels display the averaging kernels for a retrieval that combines both the measurement geometries. The black cross on each of the plots indicates the retrieval point that the averaging kernel represents. The contours therefore display how the true atmospheric profiles are smoothed to obtain this retrieval point.

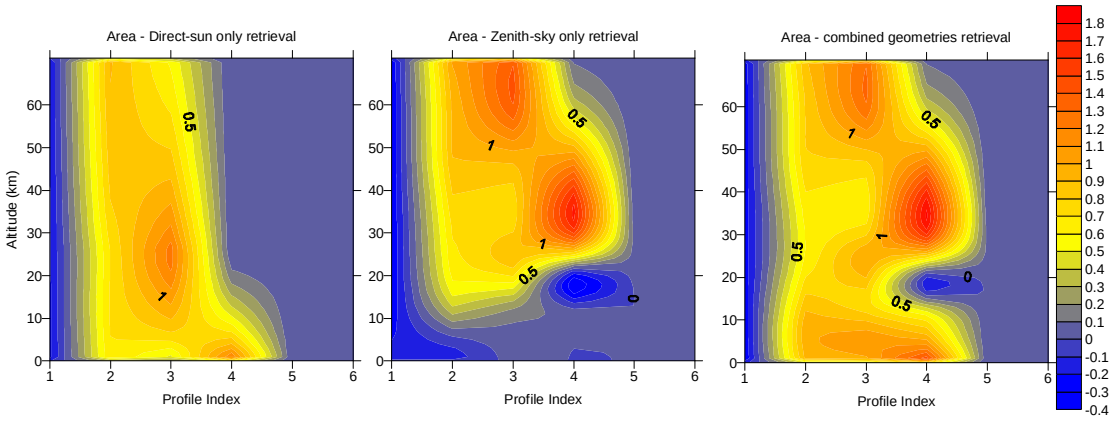


**Figure 6.5**: The area of the averaging kernels in altitude space (y axis in km) and profile space (x axis) for the BrO profiles. The profile index refers to the solar zenith angle corresponding to the profile: 1=0°, 2=75°, 3=84°, 4=87°, 5=92° and 6=95°. The area of the averaging kernels is calculated for measurements made on day 254, 2001 at Lauder. The area of the averaging kernels, and is a qualitative measure of how much information on the broad structure is being provided from the measurements rather than the *a priori*. For the state vector profiles 75° and 84° the retrieved quantities have come from the measurements, the 87° profile illustrates how there is a heavy reliance on the *a priori* data at 20 km due to the fact that the zenith-sky measurement sensitivity is in the higher stratosphere (above 25 km) and the direct-sun sensitivity is close to the surface.

only, zenith-sky only and combined geometry retrievals. This figure shows the direct-sun measurements contribute to the total column, particularly the tropospheric component. The zenith-sky measurements contribute to the stratospheric sensitivity and rely entirely on the *a priori* information for the troposphere. The combination of these geometries provides tropospheric and stratospheric sensitivity for the three profiles 75°, 84°, 87°. Where the area of the averaging kernel is negative, similar to where it is much larger than one the retrieved values are not necessarily a good representation of the true atmosphere. The area of the averaging kernels for the 84° profile between 55-65 km and the 87° profile between 30 and 40 km is considerably greater than one and considerably less than one for the 87° for the 87° at ∼20 km. The negative area in the 87° profile case is due to the zenith-sky measurement sensitivity being higher in the stratosphere and the direct-sun measurements sensitivity closest the ground. The enhanced stratospheric area can also be explained by referring to the weighting functions which show maximum peaks at the altitudes of high area.

### 6.6.4 Resolution

Resolution is a useful quantity in the evaluation of the quality of the retrieved data and an essential criterion for reporting retrieved parameters. Resolution has a number of definitions to describe the 'width' of the averaging kernel.

Full width half max of the averaging kernel peak is a commonly used definition, though it leads to overestimation of the resolution when the peak of the averaging kernel is dis-

placed from where it should be. Backus-Gilbert spread is another definition and emphases the negative lobes of the averaging kernels. This method of determining the 'width' is more complex in its determination.

A third definition utilizes the reciprocal of the averaging kernel peak. The spatial resolution of a retrieval is in this work complicated by the two-dimensional nature of the state vector. Rather than considering horizontal and vertical resolution separately as some 'width' of the averaging kernel, the simpler measure of the reciprocal of the diagonal values of **A** was used. The diagonal values of **A** give the number of degrees of freedom per state vector element. The reciprocal gives the number of state vector elements required to describe a degree of freedom.

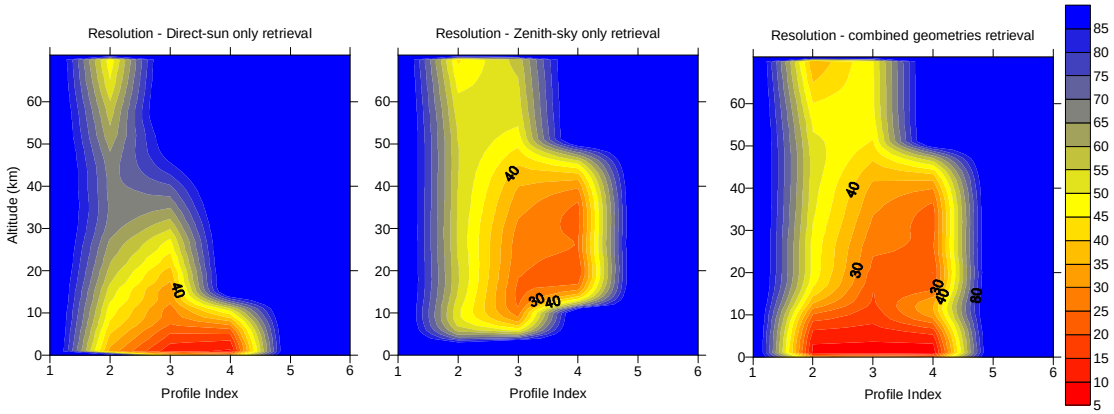


**Figure 6.6**: The resolution of the retrieval in altitude space (y axis in km) and profile space (x axis) for the BrO profiles. The profile index refers to the solar zenith angle corresponding to the profile: 1=0°, 2=75°, 3=84°, 4=87°, 5=92° and 6=95°. The resolution is calculated as the number of state vector elements required per degree of freedom. In the troposphere for the state vector profiles 75°, 84°, and 87° the resolution is 5-15 km and in the stratosphere it is 40 km for the 75° profile and 20 km for the 84° and 87° profiles.

Figure 6.6 displays the resolution for the retrievals for the direct-sun only, zenith-sky only and the combined geometries. The result that the highest resolution is achieved by combining the measurement geometries is not unexpected given the area of the averaging kernels. A resolution of 5-15 km is achieved in the troposphere for the three retrieved profiles 75°, 84° and 87°. In the stratosphere the resolution is 40 km for the 75° profile and 20 km for the 84° and 87° profiles. The resolution is poorer in the stratosphere for the 75° profile retrieval while the area of the averaging kernel is actually good. Conversely, while the area of the averaging kernel for the stratosphere of the 87° profile retrieval shows some reliance on *a priori* information, the resolution is good. This illustrates that all characterisation details need to be considered to best determine the final retrieved quantities.

| Retrieved Profile | 0° | 75° | 84° | 87° | 92° | 95° | Total |
|---|---|---|---|---|---|---|---|
| Information content(bits) | 0.03 | 2.9 | 4.0 | 2.3 | 0.02 | 0.0 | 13.5 |
| Degrees of Freedom | 0.05 | 2.1 | 2.6 | 2.3 | 0.04 | 0.0 | 7.1 |

**Table 6.1**: Information Content (bits) and Degrees of Freedom for signal for the direct-sun and zenith-sky combined geometries retrieval. The retrieval is performed for measurements made on day 254, 2001 at Lauder. Two independent pieces of information can be retrieved from the measurements for each of the retrieved profiles of 75°,84° and 87°.

### 6.6.5 Degrees of Freedom and Information Content

The degrees of freedom for signal describe the number of useful independent quantities that can be determined from a set of measurements. The degrees of freedom are evaluated by taking the trace of the averaging kernel matrix $\mathbf{A}$. As described in the previous section each value along the diagonal of $\mathbf{A}$ can be viewed as the degrees of freedom per retrieval point.

The information content of the measurements can be thought of as a measure of the factor by which knowledge is improved by making the measurement. It can be thought of as a multivariate generalization of the scalar concept of signal-to-noise ratio for the retrieval. Shannon's definition of information content is the reduction of entropy (or uncertainty) in the state that is achieved by making the measurement:

$$H = \frac{1}{2}\log_2|\hat{\mathbf{S}}^{-1}\mathbf{S}_a| = -\frac{1}{2}\log_2|\mathbf{I} - \mathbf{A}| \tag{6.8}$$

where $\hat{\mathbf{S}}$ is the retrieval covariance (see next section) and the units of $H$ are bits. Two bits of information means that the volume of the entropy in the state space has been reduced by a factor of four in making the measurement. $\mathbf{I}$ is the identity matrix.

The information content and degrees of freedom for signal are displayed in table 6.1 for measurements taken on day 254, 2001 at Lauder. There are two pieces of independent information for the three retrieved profiles 75°, 84° and 87°. These details combined with the characterisation of the retrieval obtained from the area of the averaging kernels and the resolution provide a good basis for determining what should be reported from the retrieval. A tropospheric and stratospheric column for the retrieved profiles 75°, 84° and 87° can be determined for this retrieval.

### 6.6.6 Retrieval Error Covariances

The error covariance of the retrieval $\hat{\mathbf{S}}$ is the summation of the smoothing covariance $\mathbf{S}_s$ and retrieval noise covariance $\mathbf{S}_m$:

$$\hat{\mathbf{S}} = (\mathbf{K}^T\mathbf{S}_\epsilon^{-1}\mathbf{K} + \mathbf{S}_a^{-1})^{-1} \tag{6.9}$$

$$\mathbf{S}_s = (\mathbf{A} - \mathbf{I}_n)\mathbf{S}_a(\mathbf{A} - \mathbf{I}_n)^T \tag{6.10}$$

$$\mathbf{S}_m = \mathbf{G}_y\mathbf{S}_\epsilon\mathbf{G}_y^T \tag{6.11}$$

The covariance due to each forward model parameter ($\mathbf{S}_f$) is a useful error term to evaluate. This covariance provides a quantitative evaluation of the error that a forward model parameter produces in the final retrieved quantity. When this error is too large, consideration should be given to retrieving the forward model parameter. $\mathbf{S}_f$ is evaluated as:

$$\mathbf{S}_f = \mathbf{G}_y\mathbf{K}_b\mathbf{S}_b\mathbf{K}_b^T\mathbf{G}_y^T \tag{6.12}$$

The forward model parameter covariance converts the errors in the space of the forward model parameters into the state space. This gives a quantification for the error relative to other errors arising in the retrieval, such as smoothing and retrieval noise.

## 6.7 Post Processing of the Retrieval

The area, resolution, information content and degrees of freedom collectively indicate that the usefully resolved retrieval product is the tropospheric and stratospheric column amount for the 75°, 84° and 87° state vector profiles. A matrix $\mathbf{g}$ is defined to evaluate the stratospheric and tropospheric columns from the retrieved state ($\hat{\mathbf{x}}$) summing over the relevant altitudes in the state vector to give tropospheric and stratospheric columns for each of the six state profiles ($\hat{\mathbf{x}}_c$):

$$\hat{\mathbf{x}}_c = \mathbf{g}\hat{\mathbf{x}} \tag{6.13}$$

The averaging kernels for the tropospheric and stratospheric columns for each of the six state profiles are evaluated using the following equation:

$$\mathbf{A}_c = \mathbf{g}\mathbf{A} \tag{6.14}$$

The averaging kernels for the tropospheric and stratospheric columns for the 75°, 84° and 87° retrieved profiles are displayed in figure 6.7. These display how there is a clear separation of the tropospheric and stratospheric columns for the BrO profiles of 75°, 84° and 87°. The stratospheric column for the 87° profile is somewhat poorer than the other profiles, with some of the retrieved value being derived from the 92° profile at $\sim 25\,\mathrm{km}$. Thus for the 87° stratospheric column the error in the retrieved value is expected to be higher. This is the case as displayed in the results in table 6.2.

The covariance matrices for the retrieved column quantities are evaluated in a similar

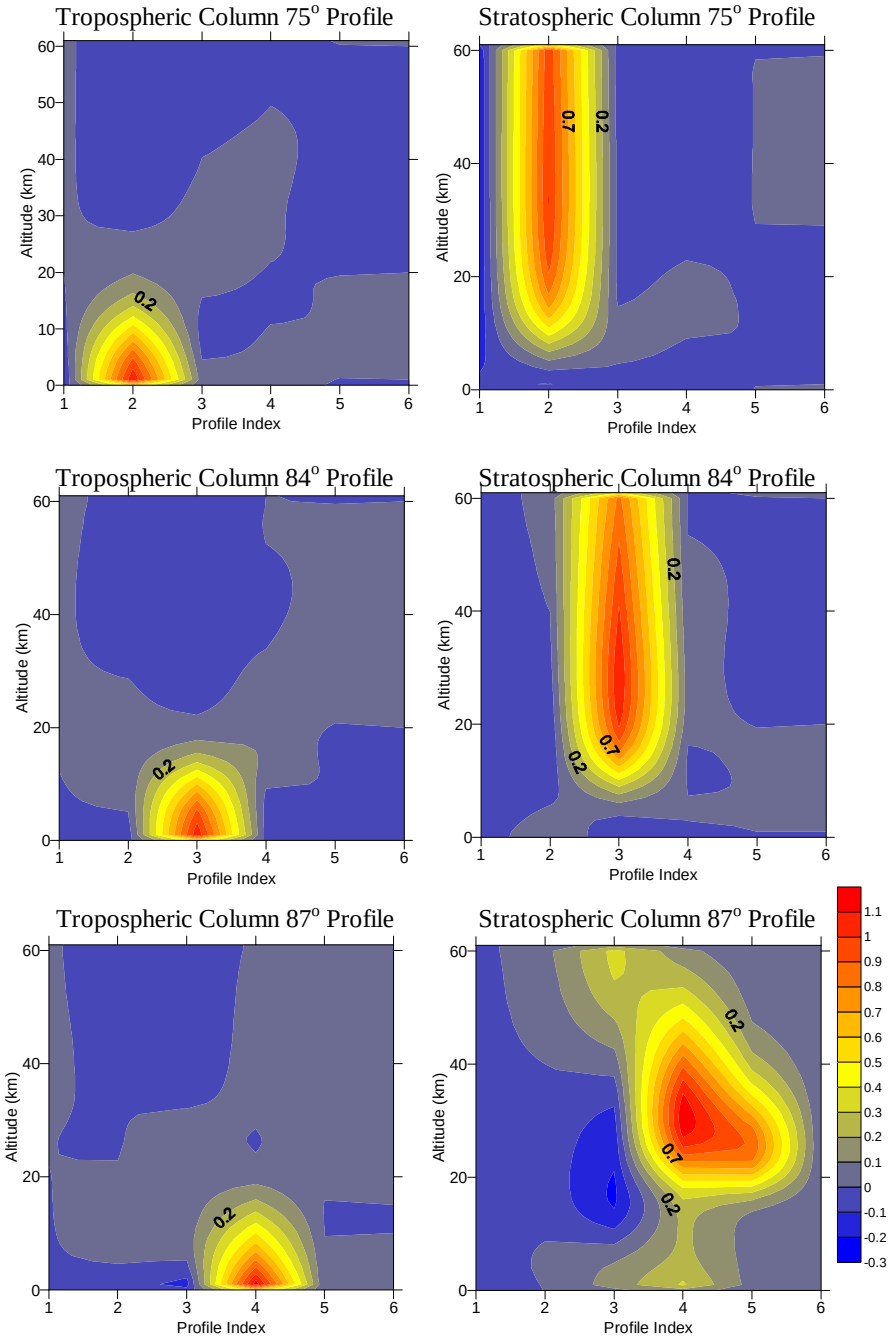


**Figure 6.7**: The column averaging kernels of the the combined measurement geometries retrieval in altitude space (y axis in km) and profile space (x axis) for the BrO profiles. The profile index refers to the solar zenith angle corresponding to the profile: 1=0°, 2=75°, 3=84°, 4=87°, 5=92° and 6=95°. The left panels display the column averaging kernels for the tropospheric columns and the right panels the column averaging kernels for the stratospheric columns. The top panels display the averaging kernels for the 75° profile, the middle panels the 84° profile and the lower panels the 87° profile.

fashion to the averaging kernels ie:

$$\mathbf{S}_c = \mathbf{g}\mathbf{S}\mathbf{g}^T \tag{6.15}$$

Table 6.2 displays the values for the *a priori* and retrieved tropospheric and stratospheric columns along with the error breakdown for the state vector profiles of 75°, 84° and 87°. The error contribution from the forward model parameters to the final retrieval error is important in the assessment of which parameters should be retrieved rather than assumed to be known to a high enough precision *a priori*. The contribution of errors arising from the variability of temperature, ozone and aerosol profiles is negligible in the total retrieval error. The covariance matrices for the forward model parameters used in the $\mathbf{S}_f$ calculation are derived from the variability of these measured quantities over Lauder. The error reduction from the *a priori* to the retrieved value demonstrates the factor by which the entropy has been reduced by making the measurement, i.e. is indicative of the information content of the measurement.

| | Tropospheric Column | | | Stratospheric Column | | |
|---|---|---|---|---|---|---|
| Retrieved Profile | 75° | 84° | 87° | 75° | 84° | 87° |
| Column *a priori* ($\times 10^{13}$ molecules.cm$^{-2}$) | 0.53±0.30 | 0.38±0.27 | 0.24±0.22 | 2.25±0.73 | 2.02±0.64 | 1.72±0.52 |
| Column retrieved($\times 10^{13}$ molecules.cm$^{-2}$) | 0.27±0.15 | 0.15±0.11 | 0.17±0.11 | 2.38±0.18 | 2.20±0.16 | 1.76±0.37 |
| Total Retrieval Error | 0.15 | 0.11 | 0.11 | 0.18 | 0.16 | 0.37 |
| Noise Error | 0.09 | 0.06 | 0.07 | 0.07 | 0.08 | 0.09 |
| Smoothing Error | 0.12 | 0.09 | 0.09 | 0.17 | 0.14 | 0.36 |
| Temperature Error | 0.03 | 0.003 | 0.002 | 0.004 | 0.01 | 0.008 |
| Pressure Error | 0.003 | 0.003 | 0.002 | 0.003 | 0.005 | 0.005 |
| Ozone Error | 0.003 | 0.0008 | 0.0001 | 0.001 | 0.002 | 0.001 |
| Aerosol Error | 0.002 | 0.0005 | 0.0003 | 0.003 | 0.002 | 0.001 |

**Table 6.2**: The retrieved column amounts for the troposphere and stratosphere with the retrieval errors. The retrieval error is then broken down into the error contribution from retrieval noise, smoothing and forward model parameter errors of temperature, pressure, ozone and aerosol to the final retrieved column in $\times 10^{13}$ molecules.cm$^{-2}$. When $\mathbf{S}_a$ is used as a tuning parameter the smoothing error is not necessarily meaningful. As $\mathbf{S}_a$ is a diagonal matrix on a 1 km grid, then the smoothing error is likely to be overestimated, because the real state will probably have longer scale correlations.

## 6.8 Measurement Fit

The 'measured' DSCDs are the products of the DOAS spectral fitting procedure described in Chapter 4. The fit of the forward model calculated DSCDs ($\hat{\mathbf{y}}$) to the measured DSCDs is essential for the retrieved quantities to represent the measurements. Figure 6.8 displays the modelled fit of the measured DSCDs with the residuals. The residuals give a good indication of how well the measurements are fitted by the forward model. A good fit is achieved with fairly low residual.

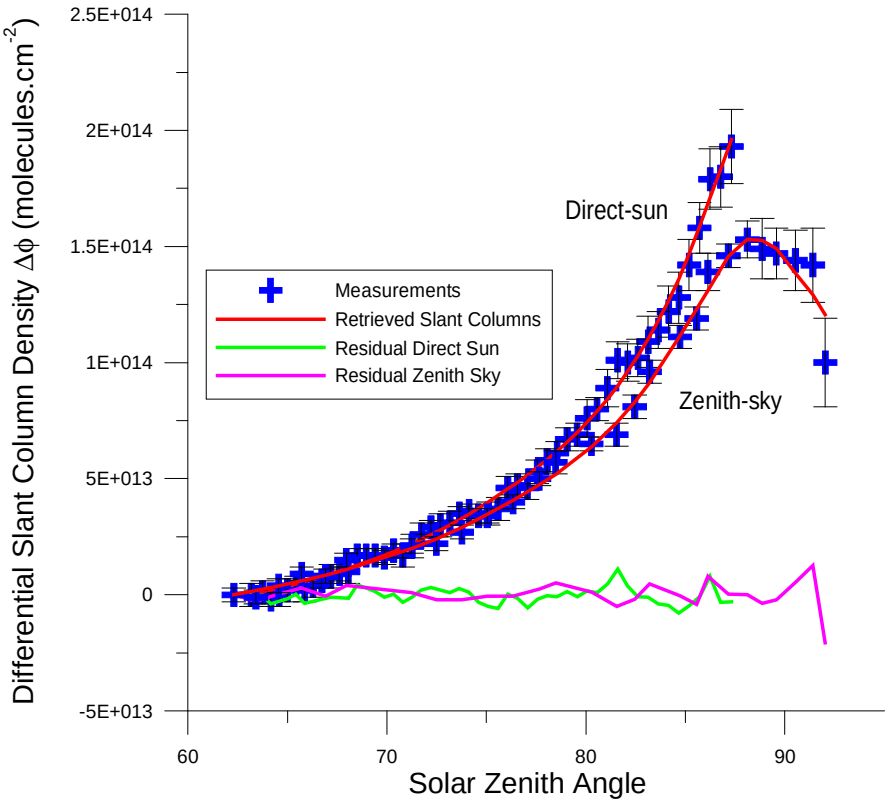


**Figure 6.8**: The measured and retrieved (modelled) DSCDs and the residuals for the direct-sun and zenith-sky sunset measurements made at Lauder on day 254, 2001.

# Chapter 7

# Measurements at Lauder, New Zealand

BrO zenith-sky measurements have been conducted at Lauder since 1995. A direct-sun viewing instrument targeting BrO has been making measurements since 2001. This Chapter presents the retrieved tropospheric and stratospheric columns for data recorded at Lauder from 2001-2003. The seasonal and diurnal variation was successfully retrieved. The stratospheric columns agree well with the coupled chemistry-climate Unified Model with Eulerian TRansport And Chemistry (UMETRAC) with an assumed total reactive bromine of 20 ppt in the lower stratosphere. The total retrieved columns agree well with coincident GOME satellite BrO measurements. An error analysis and retrieval characterisation was performed. The error contributions due to the forward model parameters are found to be negligible. A sensitivity test was conducted to establish the response of the retrieved columns to the *a priori* information and to the Ring effect. Then a brief summary is provided.

## 7.1 Measurement Site

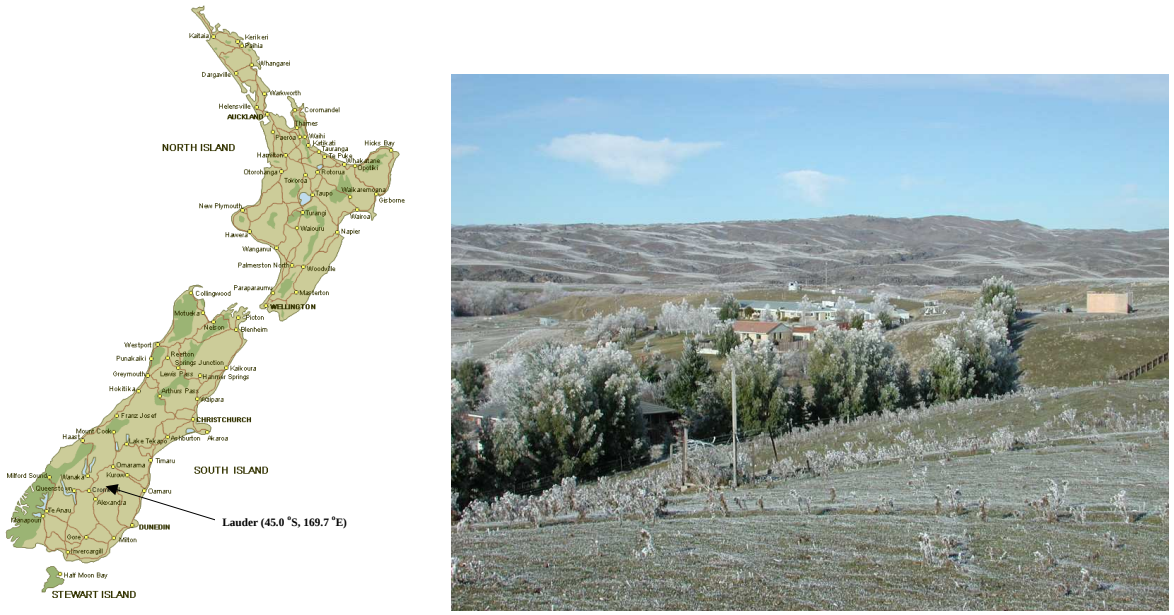


**Figure 7.1**: Lauder is located on state highway 85 north of Alexandra, Central Otago, New Zealand (45.0°S, 169.7°E).

Lauder is located at an altitude of 370 m above sea level in Central Otago, New Zealand. It is one of the five primary sites in the Network for the Detection of Stratospheric Change (NDSC). One of the world's longest spectroscopic records has been made at Lauder, New Zealand (45.0°S, 169.7°E) targeting $NO_2$ in the zenith-sky viewing mode (*Liley et al.*, 2000).

## 7.2 Retrieval of BrO Columns Over Lauder

Tropospheric and stratospheric columns were retrieved over Lauder. Only measurements made under cloud-free conditions were considered for the retrieval of tropospheric and stratospheric columns using the concepts developed in Chapters 5 and 6. A cloud-free bias is unavoidable for the direct-sun measurements, which can only be made with an unobscured sun.

72 twilight measurements were investigated for Lauder, 41 sunrise and 31 sunset periods. These measurements were made from March 2001 to April 2003. The summer and autumn months were much better sampled than the winter and spring months, since the measurement period began in summer 2001 and ended in autumn 2003. The instrument was also relocated to Arrival Heights for the late winter-spring period of 2002, as will be discussed in Chapter 8. The summer retrievals for December, January and February were calculated with 13 sunrise and 6 sunset measurements, with a tropopause height of 11.5 km. The autumn months of March, April and May were the best sampled with 22 sunrise and 18 sunset measurements, these retrievals were conducted with a tropopause height of 11.2 km. The winter retrievals for June, July and August were calculated with 4 sunrise and 4 sunset measurements, with a tropopause height of 10.6 km. The spring months of September, October and November were the least well sampled with 2 sunrise and 3 sunset measurements, these retrievals were conducted with a tropopause height of 10.8 km. The tropopause is determined from the mean seasonal tropopause heights over Lauder from ozonesonde measurements (*Bodeker et al.*, 1998).

The retrievals were conducted with the model atmosphere described up to 70 km, with 1 km model atmospheric layers (see Chapter 5 for details). The effects of refraction, molecular absorption, Rayleigh and Mie scattering were included. The aerosol extinction profiles for the stratosphere were provided by LIDAR and aerosol backscatter sonde data (*Liley*, 2003, personal communication). Ozone, temperature and pressure profiles were obtained from the ozonesonde measurements conducted at Lauder (*Bodeker et al.*, 1998). To ensure consistency, constant *a priori* information and forward model parameters were used for all retrievals over Lauder.

Six *a priori* profiles at the diurnal stages of 0°, 80°, 84°, 87°, 92° and 96° SZA were chosen to adequately describe the diurnal variation while minimizing the number of re-

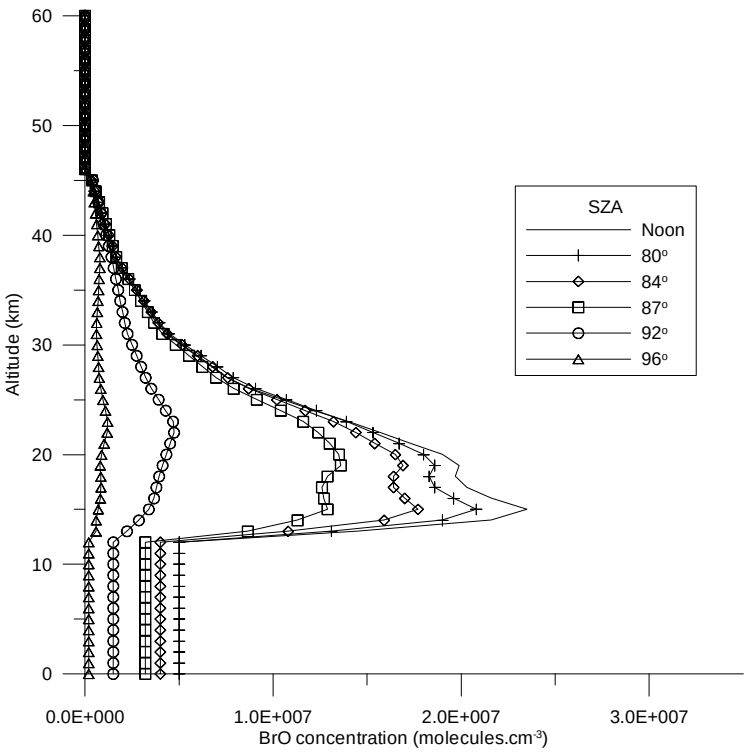


**Figure 7.2**: The stratospheric diurnal variation was calculated using a Lagrangian box model (*Kreher et al.*, 2003) for Lauder, New Zealand day 254, 2001. The tropospheric column was from the literature (*Richter et al.*, 2002) and a diurnal decrease assumed. These profiles were used as the *a priori* for the column retrievals of all measurements at Lauder.

trieval parameters. A profile at 80° SZA was chosen instead of the example given in Chapter 6 of 75° SZA to ensure that adequate information was obtained for the whole data set. Figure 7.2 displays the *a priori* profiles used in the column retrievals for Lauder. The stratospheric diurnal variation was obtained from a stationary Lagrangian chemical box model run over Lauder for sunset on day 254, 2001. A constant tropospheric number density of $5\times10^6$ molecules.cm$^{-2}$ was used in the construction of the 0° *a priori*, consistent with current estimates of an ubiquitous free tropospheric mid-latitude BrO concentration (*Richter et al.*, 2002) and a diurnal decrease was assumed.

In the construction of $\mathbf{S}_a$, 50 % of the peak value (for each of the profiles in the *a priori* state vector) was used as the error. 50 % was chosen to ensure the measurements were interpreted to provide the maximum amount of information, without over-fitting them (for more details refer to section 6.4.1).

The range of SZAs described by the DSCDs differed between measurement days due to cloud, season and the topography. A maximum of ∼88° SZA was possible most days for the direct-sun measurements. This was limited by the hills that surround the Lauder measurement site. The zenith-sky measurements had a maximum SZA of ∼93° most days, with light intensities becoming too small above this angle. The different SZA ranges for

both the zenith-sky and direct-sun geometries between days did affect the individual retrieval characterisations slightly. However, the 80°, 84° and 87° columns were well described for all of the measurement days investigated, with retrieval characterisations almost identical to those seen in Chapter 6, the averaging kernels for the 80° columns being almost identical to the 75° column averaging kernels.

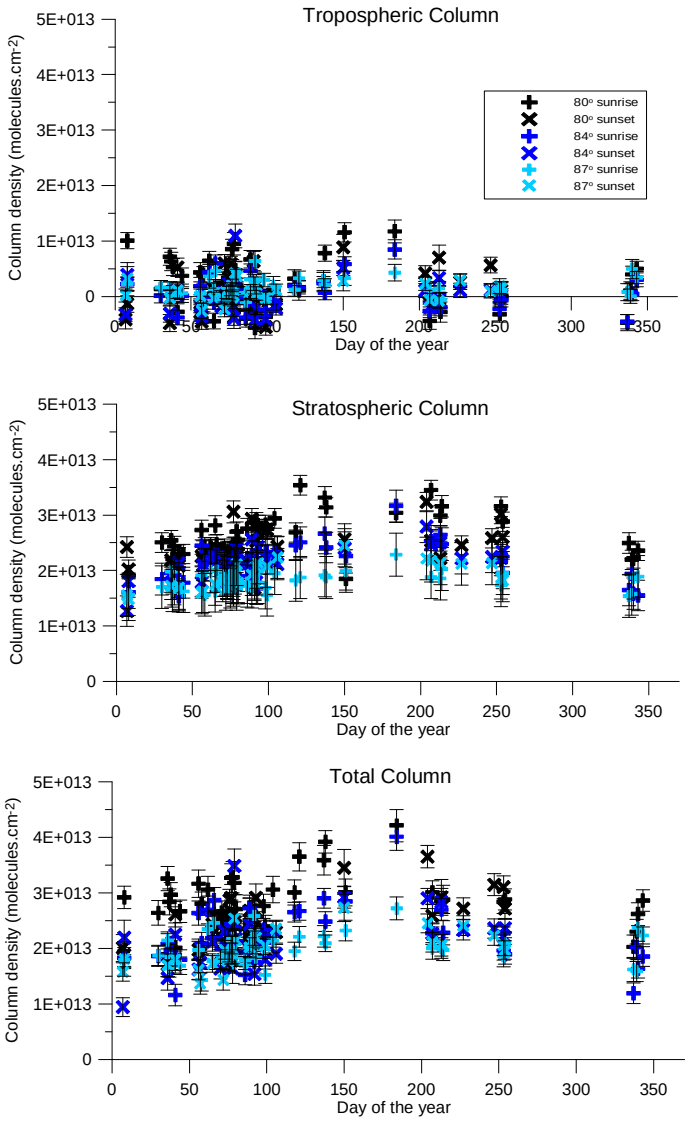


**Figure 7.3**: The retrieved tropospheric (top plot), stratospheric (middle plot) and total (lower plot) columns for BrO over Lauder 2001-2003. The retrieved columns are divided into sunrise and sunset columns for the three SZA of 80°, 84° and 87°.

The retrieved tropospheric, stratospheric and total columns for all measurement days for Lauder are displayed in figure 7.3. The seasonal and diurnal variation was captured by the retrieved stratospheric and total columns. The stratospheric columns display a clear decrease from 80° to 84° to 87° SZA, with the winter columns higher than the summer columns. The variance weighted means and errors for each season are displayed in figure

7.4 and table 7.1. The seasonal and diurnal variations are discussed in more detail in the following sections.

| **Column retrievals for each season - sunrise** | | | | | | |
|---|---|---|---|---|---|---|
| | Tropospheric Column | | | Stratospheric Column | | |
| SZA | 80° | 84° | 87° | 80° | 84° | 87° |
| Summer | 0.35±0.15 | 0.02±0.14 | 0.14±0.13 | 2.35±0.18 | 1.83±0.28 | 1.72±0.38 |
| Autumn | 0.25±0.17 | 0.14±0.14 | 0.24±0.14 | 2.63±0.18 | 2.21±0.28 | 1.83±0.38 |
| Winter | 0.22±0.18 | 0.20±0.15 | 0.17±0.14 | 3.16±0.18 | 2.70±0.29 | 2.02±0.39 |
| Spring | -0.17±0.14 | -0.14±0.13 | 0.13±0.14 | 3.02±0.18 | 2.07±0.28 | 1.85±0.39 |
| **Column retrievals for each season - sunset** | | | | | | |
| | Tropospheric Column | | | Stratospheric Column | | |
| SZA | 80° | 84° | 87° | 80° | 84° | 87° |
| Summer | -0.19±0.15 | 0.01±0.15 | 0.09±0.15 | 2.23±0.18 | 1.81±0.28 | 1.61±0.38 |
| Autumn | 0.20±0.16 | 0.08±0.14 | 0.15±0.14 | 2.39±0.18 | 2.11±0.28 | 1.95±0.38 |
| Winter | 0.46±0.17 | 0.09±0.13 | 0.09±0.13 | 2.57±0.19 | 2.49±0.29 | 2.16±0.39 |
| Spring | 0.26±0.14 | 0.04±0.12 | 0.15±0.12 | 2.74±0.17 | 2.27±0.28 | 1.94±0.38 |

**Table 7.1**: The retrieved column amounts ($\times 10^{13}$ molecules.cm$^{-2}$) for the troposphere and stratosphere of each season over Lauder 2001-2003. The upper table gives the sunrise values and the lower table the sunset values.

The retrieved tropospheric columns have an average close to zero, though scatter over a large range was observed. The variation of the retrieved tropospheric columns between measurement days (figure 7.3) illustrated that for some days elevated tropospheric BrO was observed, while other days clearly no tropospheric BrO was seen. A number of the tropospheric columns retrieved were negative with their associated retrieval errors being small, indicating a high information content is retrieved from the measurements. The negative tropospheric columns are consistent with the uncertainties within the retrieval problem (even if non-intuitive). The maximum retrieved tropospheric column of $1.2\times10^{13}$ molecules.cm$^{-2}$ is equivalent to a tropospheric mixing ratio of 0.9 ppt if the BrO is assumed to be uniformly mixed vertical profile throughout the troposphere. The seasonal mean tropospheric column amounts (figure 7.4) indicate no clear diurnal or seasonal variation. The variance weighted mean for the tropospheric column over all days was $0.14\times10^{13}$ molecules.cm$^{-2}$ (0.1 ppt if uniformly mixed throughout the troposphere). However, due to the large variability of the tropospheric column this is misleading. The Lauder ground-based measurements are consistent with a highly variable ubiquitous tropospheric column equivalent to 0.0-0.9 ppt. The majority of the tropospheric column retrievals were below $0.8\times10^{13}$ molecules.cm$^{-2}$ (0.6 ppt if uniformly mixed throughout the troposphere). These retrieved values are consistent with, but lower than the estimate of 0.5-2.0 ppt made from GOME measurements over the remote Pacific ocean (*Richter et al.*, 2002).

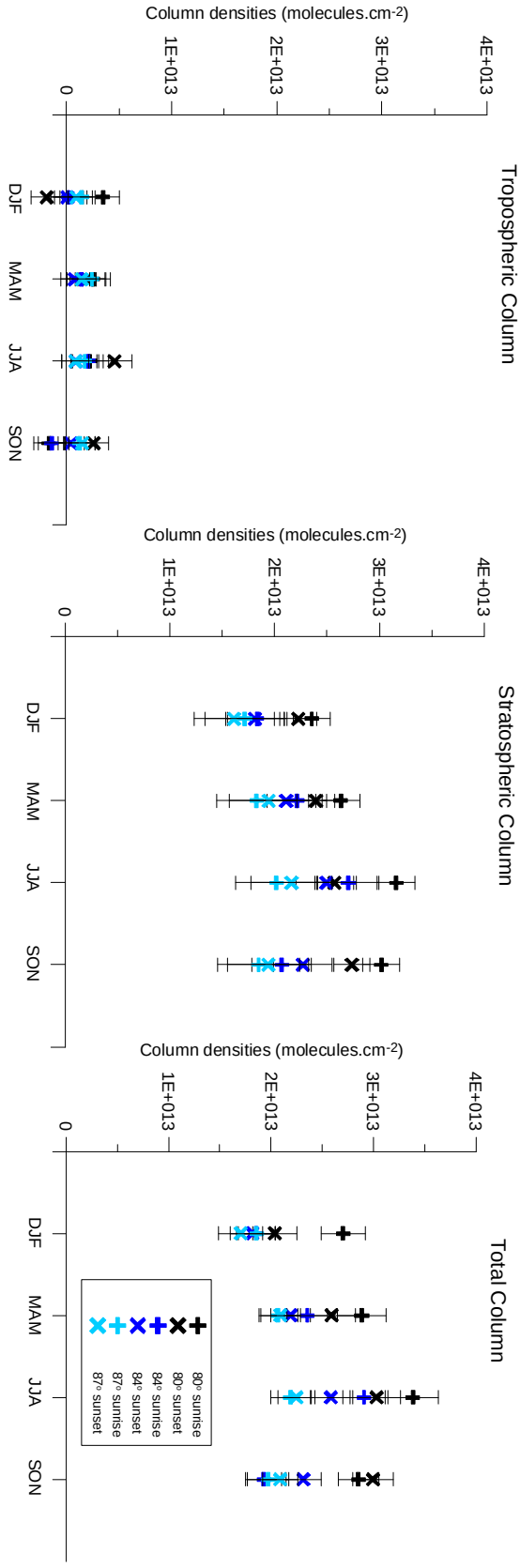


**Figure 7.4**: The variance weighted seasonal means for the retrieved tropospheric (left plot), stratospheric (middle plot) and total (right plot) columns for BrO over Lauder. The columns are divided into sunrise and sunset columns.

### 7.2.1 Seasonal Variation

Stratospheric bromine monoxide has a strong seasonal cycle. The seasonal cycle of BrO is driven by both the $Br_y$ maxima and $NO_2$ minima (*Sinnhuber et al.*, 2002). The total amount of stratospheric bromine $Br_y$ has a seasonal variation similar to that of ozone, being driven by dynamical transport. The maximum of the $Br_y$ column is in late winter-spring with the minimum in autumn. The chemical partitioning of $BrO/Br_y$ is driven mainly by the $NO_2$ seasonal cycle which is strongly temperature dependent (*Fish et al.*, 1997). A study by *Sinnhuber et al.* (2002) found the maximum $BrO/Br_y$ partitioning of 70 % occurred in winter ($NO_2$ minima) and the minimum partitioning ratio of 50 % in the summer months at mid-latitudes. Thus minimum BrO columns are expected in the summer months (December, January and February) and maximum columns in winter (June, July and August).

The retrieved columns over Lauder clearly display this seasonal behaviour. Table 7.1 shows that the maximum BrO columns were observed in winter and the minimum columns in summer. The total magnitude of seasonal variation of the columns was found to be slightly larger for the sunrise columns compared to the sunset columns. The higher BrO columns in winter, and the rapid release of BrO from HOBr and BrCl at sunrise is one possibility for this seasonality difference between sunrise and sunset. Also at colder temperatures the nighttime reservoir for bromine favours BrCl, over HOBr having implications for sunrise photolytic BrO production (*Fish et al.*, 1997).

### 7.2.2 Diurnal Variation

At mid-latitudes the most abundant inorganic daytime bromine species is BrO. The bromine daytime reservoir species are, in order of prevalence, $BrONO_2$, HOBr and BrCl (*Fish et al.*, 1995). BrO disappears into $BrONO_2$ at sunset. As a result of heterogeneous processing, $BrONO_2$ is converted to HOBr overnight, to be the major reservoir species before sunrise. The release of BrO from HOBr with sunrise is quite different from the conversion to $BrONO_2$ at sunset.

The decrease in the 80°, to the 84°, to the 87° stratospheric column was observed in the retrieved columns (see figures 7.3 and 7.4). The difference between the sunrise and sunset columns are displayed in figure 7.5 as the difference in the variance weighted monthly mean columns. In the stratosphere the 87° column sunset-sunrise difference shows that there persists more BrO at sunset than at sunrise (radical loss to reservoir species compared to radical formation by photolysis). This diurnal difference has a seasonality for the stratosphere. The sunset-sunrise difference is largest in the winter months consistent with model and observation studies (*Sinnhuber et al.*, 2002). The 84° column sunset-sunrise difference shows that these columns are approximately equal for the sunset and sunrise

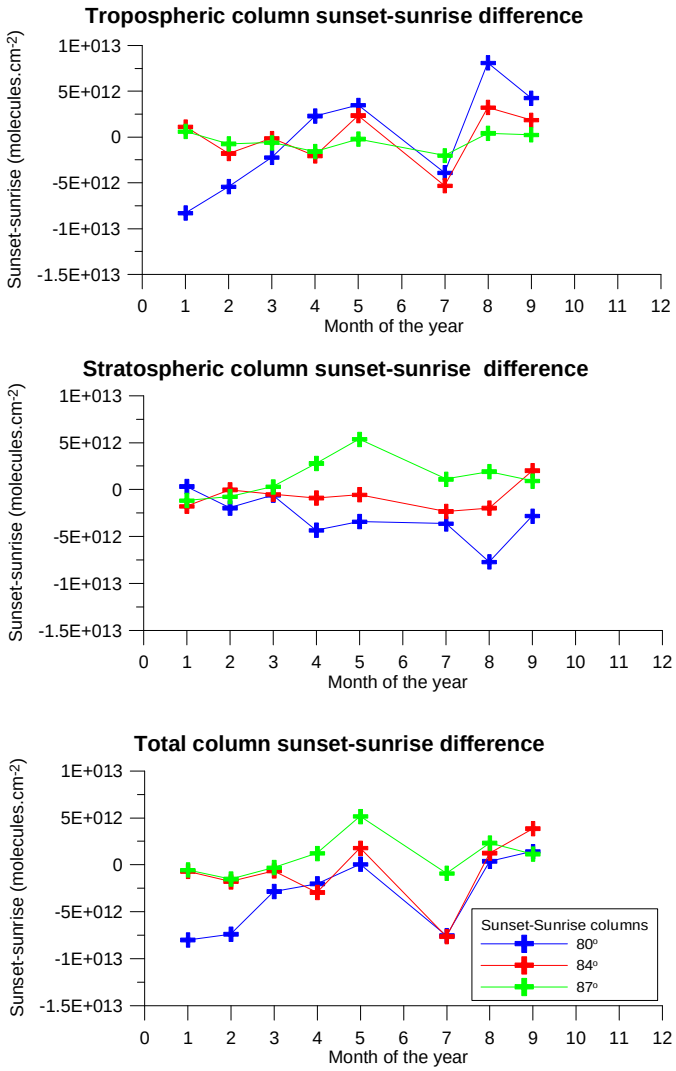


**Figure 7.5**: The sunset-sunrise difference in the tropospheric, stratospheric and total columns for BrO over Lauder 2001-2003. The retrieved columns are divided into sunset-sunrise difference for the variance weighted monthly mean columns of 80°, 84° and 87°. The summer and autumn months January through to April were well sampled for this data set. The months of June, October, November and December were less well sampled.

periods. The 80° column sunset-sunrise difference illustrates that the sunrise column is larger than the sunset column for this SZA. The seasonal difference seen for the 80° columns compared to the 87° columns is about the same in magnitude, but opposite in sign. The tropospheric and total column sunset-sunrise differences have no clear diurnal or seasonal trends.

The diurnal variation with SZA of the total columns is displayed in figure 7.8. The total columns display a diurnal variation which is dominated by the stratospheric diurnal variation. Figure 7.8 clearly illustrates the increase in columns with decreasing SZA for each season and is discussed in more detail in the GOME comparison section 7.3 below.

### 7.2.3 Retrieval Residuals

The mean residuals for the forward model fit to the measurements for all of the Lauder column retrievals are displayed in figure 7.6. The mean residuals ($\mathbf{y}$-$\hat{\mathbf{y}}$) allow many types of systematic errors to be determined. The upper plot of figure 7.6 clearly illustrates that

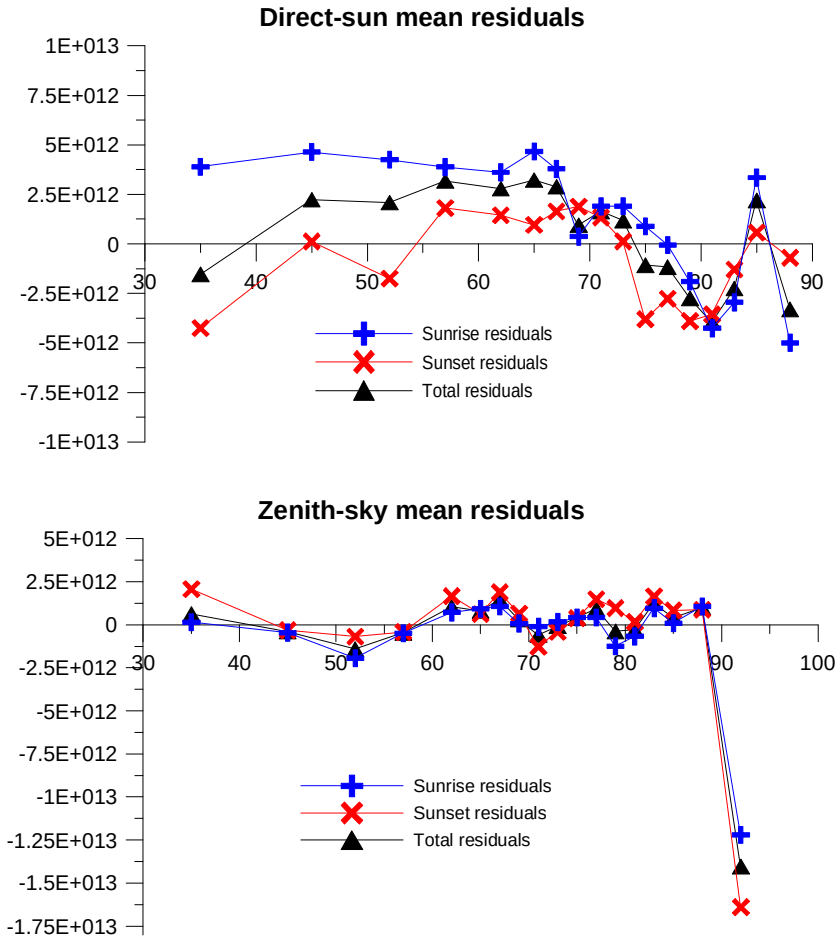


**Figure 7.6**: The mean residuals for all retrieval fits to the data. The upper plot displays the mean residuals for the direct-sun measurement fits. The lower plot displays the mean residuals for the zenith-sky measurement fits. Clear systematic errors are evident in the direct-sun fit with filter changes. The zenith-sky residuals show a systematic low residual for the highest SZA.

some systematic errors were present in the direct-sun viewing geometry. These features were caused by the filter changes which are necessary in this geometry to avoid high levels of light intensity saturating the detector. Filter changes occurred at 77° - 78° and at 82° - 84°. The mean residuals for the sunrise of the direct-sun geometry indicated that the forward model values were systematically too low compared to the measurements for low SZAs. This indicated that in the sunrise direct-sun measurements the reference SCD was often lower than expected (due to cloud, sun-tracker drift etc).

The mean residuals for the retrieval fit of the zenith-sky measurements indicated that

the measurements were systematically lower than the forward model for large SZA. This is indicative that perhaps the forward model is no longer a good approximation to the true atmospheric radiative transfer at large SZA. Alternatively the low measurement intensities of these measurements may be introducing errors.

These residuals are small compared to the DSCDs, except at low SZA where the residuals are about equivalent to the DSCDs. The total residuals for the direct-sun represent about an error of 50 % error for the DSCDs less than 60°. The systematic errors caused by the filter changes represent an error of about 10 % in the DSCDs (refer to figure 6.8 for typical DSCD values). The systematic high residuals in the highest SZA for the zenith-sky DSCDs correspond to an error of about 15 %.

## 7.3 Comparison with GOME

The Global Ozone Monitoring Experiment (GOME) is one of the experiments on the ERS-2 satellite, which was launched in April 1995 (*Burrows et al.*, 1999). GOME is a nadir viewing experiment with a footprint of $40\times320\,\mathrm{km}^2$ and covers the whole earth in 3 days. As well as monitoring ozone, columns of $NO_2$, BrO, OClO, HCHO and $SO_2$ can be retrieved. The global coverage and column retrievals make this satellite experiment seem ideal for a comparative study with the columns retrieved in this work for Lauder. However, the comparison is complicated by the different SZAs of the two methods. Near realtime column maps are available on http://www.iup.physik.uni-bremen.de/gomenrt/. Comparative ground-based and balloon studies with GOME have led to the conclusion that there exists a free tropospheric background concentration of BrO at all latitudes between 0.5 - 2 ppt (*Van Roozendael et al.*, 2002; *Richter et al.*, 2002; *Fitzenberger et al.*, 2000).

The GOME overpasses within 200 km of Lauder made at the same time as the sunrise ground-based measurements were used for this comparative work (*Richter*, 2003, personal communication). *Richter* (2003) retrieved DSCDs for GOME with a reference spectrum taken for each equatorial crossing. A reference amount of $4\times10^{13}\,\mathrm{molecules.cm}^{-2}$ was added to account for the equatorial slant column amount. Then the VCDs were determined with AMFs calculated with a climatology that only included stratospheric BrO (*Richter*, 2003). The ERS-2 satellite overpasses Lauder at 10.30 am local time, with SZAs in the range of 40°-70°.

The comparison was not straightforward due to the columns retrieved from ground-based measurements being at higher SZA than the GOME columns. Figure 7.7 shows the comparison between the ground-based retrieved columns and the columns measured by GOME on the same day (concurrent). Unfortunately only eight GOME overpasses were concurrent with the sunrise ground-based measurements, even though the GOME

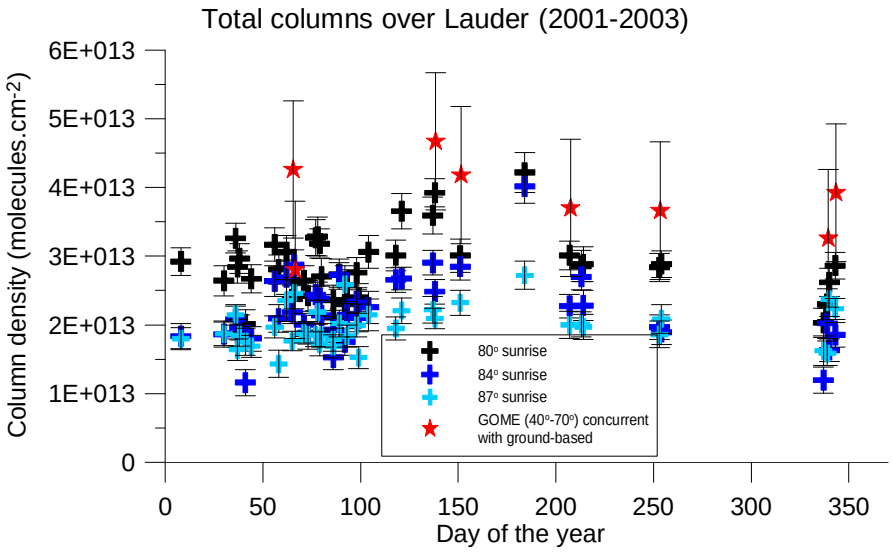


**Figure 7.7**: The total BrO columns retrieved from ground-based sunrise measurements over Lauder 2001-2003 are compared with the total columns from concurrent GOME overpasses (2001-2002).

sampling was frequent (every three days). Clear-sky conditions generally persisted for 2-4 days, and some periods occurred without a satellite overpass within 200 km of Lauder. The GOME columns were on the whole higher than the 80° retrieved columns from the ground-based measurements in this work. The difference between the 80° retrieved columns and the GOME columns was $\sim 0.9 \times 10^{13}$ molecules.cm$^{-2}$, but the methods agreed within their respective errors. Of this $0.9 \times 10^{13}$ molecules.cm$^{-2}$ about $0.3 \times 10^{13}$ molecules.cm$^{-2}$ accounts for the difference in SZA (from diurnal variation of BrO (see the noon versus 80° profiles in figure 7.2)). The GOME satellite is measuring total BrO columns with a bias (high) of between 15–18% of the 80° columns at Lauder.

The variation of the sunrise and sunset total columns with SZA for all of the seasons is displayed in figure 7.8. The retrieved columns as discussed above in section 7.2.2 increased with decreasing SZA. The sunrise columns were slightly higher than the sunset columns for 80°, but the reverse was true at 87°.

The seasonal variation of the columns is evident in both the retrieved ground-based and GOME columns. The winter columns were the highest retrieved columns, and the summer columns were the lowest. The GOME columns at large SZA represent the winter columns, and these were slightly higher than the low SZA GOME columns measrued at smaller SZAs in summer.

While the different SZAs of the GOME and ground-based column retrievals complicates their comparison, they agree within their errors. The GOME columns were overall higher than the 80° total column retrievals from the ground-based measurements.

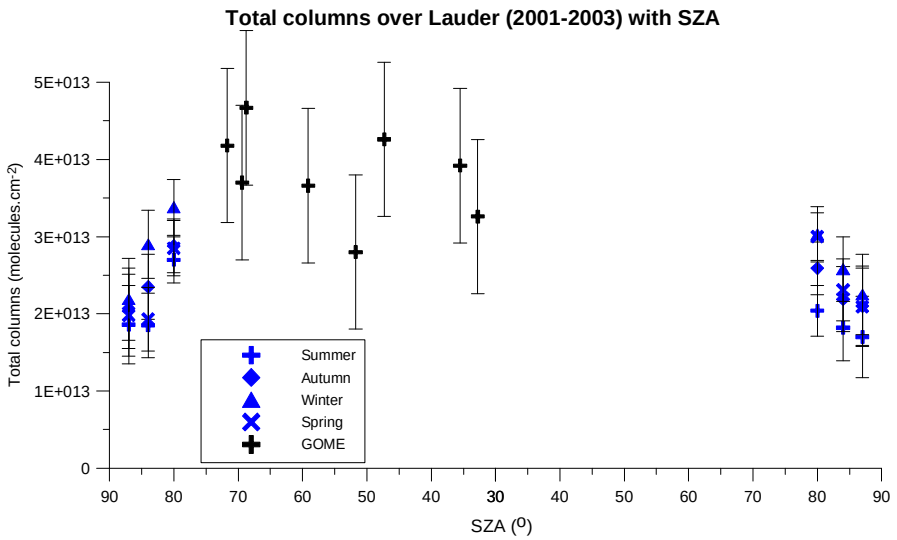


**Figure 7.8**: The variance weighted mean total columns for each season retrieved from ground-based measurements at Lauder, 2001-2003 are displayed with SZA. The concurrent GOME measurements made over the 2001-2002 period are also displayed.

## 7.4 Comparison with UMETRAC

UMETRAC (Unified Model with Eulerian TRansport And Chemistry) is a three dimensional chemistry-climate coupled model (*Austin*, 2002). A set of important stratospheric chemical reactions is included. The model is run on a 2.5° (latitude) × 3.75° (longitude) grid on 64 vertical levels from the surface to 0.01 hPa. UMETRAC model runs were conducted for Lauder 2002 (*Struthers*, 2003, personal communication).

At midlatitudes the $BrO/Br_y$ ratio is calculated by the UMETRAC model to be about 50 %, which is consistent with the stratospheric chemical model SLIMCAT calculations (*Sinnhuber et al.*, 2002). A $Br_y$ loading of 20 ppt has been recently inferred from modelling and observational studies (*Fish et al.*, 1997; *Harder et al.*, 2000; *Sinnhuber et al.*, 2002). The UMETRAC model assumes 16 ppt from early estimates of the stratospheric $Br_y$ loading (*Austin*, 2002). A more current $Br_y$ loading of 20 ppt is assumed in the lower stratosphere for the comparison here.

Figure 7.9 illustrates the comparison of the tropospheric and stratospheric columns over Lauder calculated with the UMETRAC model for 2002 and the columns retrieved in this work (2001-2003). The year 2002 of the UMETRAC model run was chosen for this comparison as it was representative of the model calculations for the years 2001-2003. The agreement between the retrieved columns over Lauder and those calculated by the UMETRAC model with a $Br_y$ loading of 20 ppt was very good. The UMETRAC model stratospheric columns were overall slightly lower than the observed columns. The seasonal variation of the columns was more pronounced for the UMETRAC model columns than that seen with the retrieval. The tropospheric columns calculated by the UMETRAC

model had a tropopause height of 11 km. The lower tropopause in winter explains the higher winter columns for the troposphere calculated by the model. However, overall the agreement was good, with the seasonal and diurnal variation quite consistent between the UMETRAC model (with 20 ppt for $Br_y$ in the lower stratosphere) and the retrieved columns.

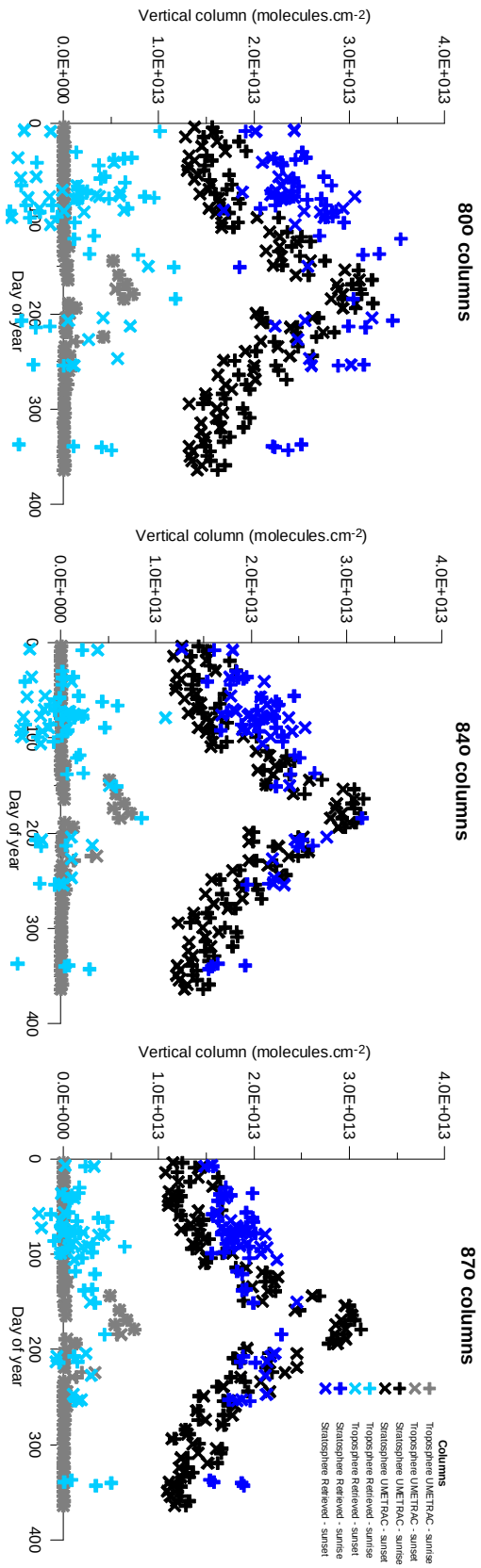


**Figure 7.9**: The retrieved tropospheric, stratospheric and total columns for BrO over Lauder, 2001-2002 are compared with the model calculations from the UMETRAC model for 2002. The left plot shows the comparison for the 80° columns, the middle plot for the 84° columns and the right plot for the 87° columns.

### 7.4.1 Implications for Mid-Latitude Ozone Loss

The implications of increased bromine loadings in the stratosphere are far reaching. A modelling study of the effect of reducing the stratospheric bromine burden from 20 ppt to 10 ppt was conducted by *Sinnhuber* (2000). *Sinnhuber* (2000) found that reducing the bromine loading to pre-industrial levels of 10 ppt led to an increase in ozone of 10 DU or 3 % at 45 °S in autumn. When the chlorine loading was also halved (reduced from 3.6 ppb to 1.8 ppb) the ozone increase was larger; 20 DU or 8 %. Ozone depletion cycles that directly involve bromine account for ∼25 % of southern hemispheric mid-latitude ozone losses (*Lee et al.*, 2002). The role of bromine in mid-latitude ozone losses is further extended by the heterogeneous hydrolysis of $BrONO_2$. This process is indirectly involved in mid-latitude ozone losses by increasing the $HO_x$ and $ClO_x$ abundances (*Hendricks et al.*, 1999).

The column amounts retrieved in this work are consistent with a $Br_y$ loading in the lower stratosphere of ∼ 20 ppt. Neglecting the increased bromine loadings will result in an underestimation of the ozone loss by chemical models.

## 7.5 Retrieval Characterisation and Error Analysis

A rigorous analysis was conducted to determine the errors that are produced by the retrieval and the forward model parameters over all of the twilight measurements at Lauder. Table 7.2 displays the mean error contribution from the retrieval and forward model parameters for all of the Lauder retrievals.

The retrieval error is broken down into the components of noise and smoothing. The noise error is the measurement error covariance in the space of the retrieval. The smoothing error is the largest and least well estimated source of error in the retrieved quantities. The use of $\mathbf{S}_a$ as a tuning parameter means that the smoothing error is not necessarily meaningful, and is likely to be an overestimate with the formulation used here, because the diagonal covariance describes a relatively large amplitude of fine structure. The real state will probably have longer scale correlations, and less fine structure (*Schofield et al.*, 2003). The smoothing errors produced in the column retrievals over Lauder were not grossly unrealistic, though they contribute the largest component to the total retrieval error.

The covariance matrices for the forward model parameters $\mathbf{S}_b$ used in the $\mathbf{S}_f$ calculation are derived from the variability of these measured quantities over Lauder (*Bodeker et al.*, 1998). The temperature profile variability was found to be ∼ 2 % and the surface pressure variability was ∼ 1 %. The ozone profile and aerosol extinction profile variabilities were found to be about ∼ 10 %. The variability in the temperature profile, surface pressure,

| Error breakdown for Lauder retrievals (2001-2003) | | | | | | |
|---|---|---|---|---|---|---|
| | Tropospheric Column | | | Stratospheric Column | | |
| Retrieved Profile | 80° | 84° | 87° | 80° | 84° | 87° |
| Total Retrieval Error | 0.16 | 0.14 | 0.14 | 0.18 | 0.28 | 0.38 |
| Noise Error | 0.09 | 0.08 | 0.08 | 0.07 | 0.13 | 0.09 |
| Smoothing Error | 0.13 | 0.11 | 0.11 | 0.16 | 0.25 | 0.37 |
| Temperature Error | 0.02 | 0.009 | 0.004 | 0.02 | 0.01 | 0.006 |
| Pressure Error | 0.004 | 0.003 | 0.002 | 0.005 | 0.006 | 0.006 |
| Ozone Error | 0.0005 | 0.0002 | 0.0001 | 0.0004 | 0.0002 | 0.0001 |
| Aerosol Error | 0.0003 | 0.0002 | 0.0001 | 0.0003 | 0.0002 | 0.0001 |
| Information Content | 0.8 | 0.7 | 0.5 | 2.1 | 1.8 | 1.1 |
| Degrees of Freedom | 0.8 | 0.8 | 0.6 | 1.6 | 1.9 | 1.3 |

**Table 7.2**: The error breakdown for the entire Lauder data set is tabulated. The error contribution to the retrieved columns is separated into noise and smoothing for the retrieval error. The forward model parameter errors of temperature, surface pressure, ozone and aerosol extinction are also tabulated. The errors are expressed in units of absolute vertical columns ($\times 10^{13}$ molecules.cm$^{-2}$). Also provided is the information content (bits) and the degrees of freedom for the whole data set.

ozone profile and aerosol extinction profile all produced negligible errors in comparison to the total retrieval error.

The mean Shannon information content and degrees of freedom for signal for each of the derived columns are also displayed in table 7.2. The information content describes the reduction in the uncertainty in the state that results from making the measurement. The degrees of freedom for signal describes the number of useful independent pieces of information in the retrieved quantity. There is an average of between 0.6 and 0.8 independent pieces of information in the tropospheric column retrievals over all the retrievals. The information content of the tropospheric column retrievals is between 0.5 and 0.8 bits. The stratospheric column retrievals showed between 1.3 and 2.0 independent pieces of information and an information content between 1.1 and 2.2 bits. Having less than one degree of freedom for signal indicated that generally the tropospheric columns were not as well described by the measurements as the stratospheric columns.

Information content and degrees of freedom for signal are just two of the parameters used in the characterisation of the retrievals, and are derived from the averaging kernels. The averaging kernels themselves give the best description of how well the retrieved values represent the true atmosphere. The averaging kernels for each of the 71 column retrievals performed over Lauder illustrated clear tropospheric and stratospheric column separation. While the averaging kernels for each individual column retrieval was slightly different due to different measurement ranges, they were well represented by the exemplary column averaging kernels displayed in figure 6.7. The stratospheric column of the 87° profile was consistently the poorest representation of the true atmosphere. This was reflected in the

larger smoothing error for this column.

## 7.6 Retrieval Sensitivity Studies

The response of the retrieval to three sensitivity tests (*a*, *b* and *c*) involving perturbations in the *a priori* were investigated. Changing the *a priori* to exclude a tropospheric amount (test *a*) resulted in less being retrieved for the tropospheric columns, without having much influence on the stratospheric columns. This is consistent with the tropospheric *a priori* having more influence on the tropospheric column retrievals than the stratospheric column retrievals.

| **Difference from standard retrieval** | | | | | | |
|---|---|---|---|---|---|---|
| | Tropospheric Column | | | Stratospheric Column | | |
| Retrieved Profile | 80° | 84° | 87° | 80° | 84° | 87° |
| Standard Column | 0.19 | 0.06 | 0.14 | 2.63 | 2.19 | 1.89 |
| No troposphere: *a* | -0.12 | -0.09 | -0.13 | -0.01 | 0.05 | -0.002 |
| 30 % *a priori* error: *b* | 0.03 | 0.04 | 0.04 | -0.02 | 0.06 | 0.04 |
| 70 % *a priori* error: *c* | -0.004 | -0.02 | -0.01 | 0.002 | -0.04 | -0.03 |
| 8 % increase in zenith-sky | -0.13 | -0.09 | -0.03 | 0.17 | 0.10 | -0.03 |

**Table 7.3**: The effect of changing the *a priori* information on the retrieved column amounts for the troposphere and stratosphere for Lauder 2001-2003 is tabulated. The standard retrieved columns are the variance weighted means of all of the retrievals over Lauder. The response is given as the difference from the standard retrieved column amounts ($\times 10^{13}$ molecules.cm$^{-2}$) calculated with an *a priori* error of 50 %. The retrieval response to assuming no tropospheric BrO in the construction of the *a priori* results in a decrease in the retrieved tropospheric columns while not altering the stratospheric columns. The retrieval response to assuming 30 % and 70 % error in the *a priori* information used in the construction of $\mathbf{S}_a$ is small. The result of adding 8 % to the zenith-sky measurements to simulate the underestimation by Raman scattering reduces the tropospheric column at the expense of the stratospheric column.

The affect of reducing the *a priori* error estimate from 50 % to 30 % was investigated (test *b*). This resulted in the retrieval being more heavily reliant on the *a priori*. The resultant columns were closer to the *a priori* columns, but the change was fairly negligible. By increasing the *a priori* error to 70 % (test *c*) there is an increased dependence on the measurements. The response of the retrieval to this perturbation was negligible indicating the 50 % *a priori* error was adequate to achieve a good measurement fit.

The Ring effect due to rotational Raman scattering (see section 4.3.3) is one of the influencing factors in the determination of the zenith-sky DSCDs. It is thought that BrO DSCDs are underestimated by ∼8 % (*Fish and Jones*, 1995) due to the reduction in intensity associated with viewing scattered light in this geometry. A further sensitivity test was performed where the zenith-sky DSCDs were increased by 8 % and the direct-sun measurements were left unaltered. An 8 % underestimation of the zenith-sky measurements

is probably too high for this data set because the Lauder measurements were conducted with a polarized instrument and there was a clear-sky bias.

The resultant retrieval response to this Ring test was to change the tropospheric and stratospheric partitioning. The zenith-sky measurements are most important for obtaining stratospheric sensitivity thus an 8 % increase in the DSCDs resulted in ∼7 % increase in the stratospheric columns. As the direct-sun measurements give good tropospheric and total column information, the absolute increase in the stratospheric column was compensated for by a similar decrease in the tropospheric column. The total columns increased slightly. This test highlighted the reliance of the column retrievals upon both measurement sets. This is advantageous in that information inaccessible by examining one measurement set independently can be retrieved. However, it also demonstrates that if one measurement set is not adequately described in terms of its absolute values and errors this will result in errors in the final retrieval.

## 7.7 Summary

The retrieved stratospheric columns at 80°, 84° and 87° SZA over Lauder capture seasonal and diurnal variations of the stratosphere. The largest BrO stratospheric columns were observed in winter and the smallest in summer. The decrease in the stratospheric column from 80° to 84° to 87° was seen in both the sunrise and sunset column retrievals. The sunrise columns, while smaller than the sunset columns for 87°, were larger for the 80° columns. The magnitude of this sunset-sunrise column difference was largest in winter.

The retrieved tropospheric columns showed large variability. A large range of tropospheric columns were retrieved from -5.6×$10^{12}$ to 1.2×$10^{13}$ molecules.cm$^{-2}$. No clear diurnal or seasonal variation was obvious. The maximum retrieved tropospheric column of 1.2×$10^{13}$ molecules.cm$^{-2}$ is equivalent to a tropospheric mixing ratio of 0.9 ppt if the BrO is assumed to be uniformly mixed throughout the troposphere. The direct-sun and zenith-sky measurements for Lauder are consistent with a variable ubiquitous tropospheric BrO mixing ratio between 0.0 - 0.9 ppt with an error of 0.2 ppt. The majority of the BrO tropospheric column retrievals over Lauder were below 0.8×$10^{13}$ molecules.cm$^{-2}$ and below 0.6 ppt if BrO is assumed to be uniformly mixed throughout the troposphere.

The comparison with GOME was not straightforward because of the different SZAs of the GOME and ground-based column retrievals. The agreement between the total columns retrieved by the ground-based measurements and the GOME measurements was within their respective errors. The GOME columns overall were slightly higher than the 80° total column retrieved from the ground-based measurements.

The overall consistency between the retrieved columns and the columns calculated by the UMETRAC model was good. The UMETRAC model showed the retrieved strato-

spheric columns over Lauder to be consistent with a $Br_y$ loading of 20 ppt in the lower stratosphere. The seasonality of the retrieved columns was not as pronounced as that seen by the model, though the general trend was quite consistent between the two data sets.

The errors for the whole Lauder data set due to the variability of the forward model parameters were found to be negligible. The retrieval errors of smoothing and noise dominated the errors of the columns retrievals. The averaging kernels for the Lauder measurements consistently showed good tropospheric and stratospheric column separation. The parameters of information content and degrees of freedom for signal showed that the columns were well described by the measurements.

The column retrievals demonstrated good stability to increasing the *a priori* error. Decreasing the *a priori* error resulted in larger changes in the retrieved columns as the retrievals were constrained more by the *a priori* information. Changing the *a priori* tropospheric description had the largest implications for the retrieved tropospheric columns. A test where the zenith-sky DSCDs were increased by 8 % altered the partitioning between the retrieved partial columns for the troposphere and the stratosphere.

# Chapter 8

# Measurements at Arrival Heights, Antarctica

A direct-sun BrO measurement campaign was run over ten weeks from the 20th of August to the 30th of October 2002. Zenith-sky measurements have been routinely made at Arrival Heights since 1995. This chapter presents the stratospheric and tropospheric columns retrieved for Arrival Heights, 2002 over the ten week spring campaign. Auxiliary surface ozone and multi-axis measurements were used to identify high tropospheric BrO events. The retrieved columns were compared with columns from the GOME satellite experiment and with the UMETRAC coupled climate-chemistry model. A complete characterisation and error analysis for all of the retrieved columns over Arrival Heights was performed. The sensitivity of the retrieved columns to changing the *a priori* error and to changing the cross-section used to derive the zenith-sky DSCDs was explored. A brief summary is provided.

## 8.1 Measurement Site


**Figure 8.1**: Arrival Heights is on Ross Island at the edge of the Ross Sea ice shelf. The picture depicts the view to the north west from the measurement site, over the sea-ice.

A New Zealand laboratory is situated at Arrival Heights, Antarctica (77.8°S, 166.7°E). Arrival Heights is located at an altitude of 250 m above the sea-ice on Ross Island, at the edge of the Ross Sea ice shelf. Arrival Heights is one of the sites that makes up the Antarctic NDSC primary measurement station.

## 8.2 BrO DSCDs and Surface Ozone Measurements

The polar spring of 2002 in the Antarctic was an unusual year with the polar vortex splitting in two and becoming weaker. Stratospheric ozone losses were not as great as in previous years (*Hoppel et al.*, 2003; *Allen et al.*, 2003). During the measurement campaign twilight runs at the beginning and end of the measurement period were the only ones made while Arrival Heights was under the polar vortex.

The direct-sun viewing instrument used at Lauder was relocated to Arrival Heights for the spring period of 2002. The lower horizon surrounding the Arrival Heights site compared to the Lauder site, allowed measurements to be made up to 89° SZA. The SZA range at Arrival Heights was much less than at Lauder, with a maximum range of 66°-89° at the end of October. The azimuthal change though was much larger than at mid-latitudes with the sun taking twelve hours to complete this change in SZA. As a result the integration times for one DSCD measurement were quite long. A complete twilight run in the direct-sun viewing mode required clear conditions over the entire twelve hours.

In the polar spring the phenomenon of almost complete depletion of ozone in the boundary layer has been attributed to very high levels of bromine (*Tang and McConnell*, 1996). These natural 'bromine explosion' events have been recorded in both the Arctic (*Barrie et al.*, 1988, 1994; *Hausmann and Platt*, 1994) and Antarctic (*Kreher et al.*, 1997; *Wagner and Platt*, 1998) (see section 3.3 for mechanistic details). Figures 8.2 and 8.3 display both the direct-sun and multi-axis DSCD measurements for Arrival Heights and the corresponding surface ozone measurements for spring 2002.

The lower panels of figures 8.2 and 8.3 illustrate the measurements made over the ten week spring period of 2002, in the direct-sun and the multi-axis viewing modes. Multi-axis measurements have been made at Arrival Heights since 1999 (for instrument description see *Friess* (2001)). The multi-axis measurements are made at four alternating elevation angles of zenith (90°), then 20°, 15°, and 10°, 20° behind the sun (see section 4.2 for viewing geometry information) (*Friess*, 2003, personal communication). The 90° viewing angle is equivalent to the zenith-sky viewing geometry. The radiative transfer through the stratosphere is similar for each of these multi-axis viewing angles. The difference between the viewing angles is their respective tropospheric paths. The longest tropospheric path is associated with the smallest elevation angle, thus the 10° measurements have the highest DSCDs when observing tropospheric absorbers. The separation of the DSCDs for the different viewing angles is indicative of tropospheric BrO, if the DSCDs decrease such that $\triangle\phi(90°) < \triangle\phi(20°) < \triangle\phi(15°) < \triangle\phi(10°)$.

Surface ozone measurements were made at Arrival Heights with a Dasibi instrument using UV-photometry. Hourly averages of the surface ozone measurements made for the 2002 spring period at Arrival Heights are displayed in the upper panels of figures 8.2 and

8.3 (*Oltmans*, 2003, personal communication).

Figures 8.2 and 8.3 show a strong anticorrelation between the BrO DSCDs and low surface ozone. The DSCDs for the different viewing angles of the multi-axis measurements overlay each other for most of the measurement days, indicating low tropospheric BrO concentrations. Two events of high tropospheric BrO were observed with the multi-axis viewing geometry during the spring campaign. The days of 262 and 297-300 show clear separation of the DSCDs for the different multi-axis viewing angles and a corresponding decrease in surface ozone. Clear-sky conditions existed for just two of the twilight periods during these high tropospheric BrO periods, allowing direct-sun DSCDs to be made for the sunset on day 297 and sunrise on day 298. The direct-sun DSCDs made on these days were much higher than all previous twilight periods, consistent with an elevated BrO column.

The surface ozone decreased over the measurement campaign consistent with the annual cycle of tropospheric ozone. The maximum surface ozone is in winter, with a minimum in summer due to photolysis rates (see Chapter 3). There were some lower surface ozone measurements which did not have corresponding high tropospheric BrO, (days 281 and 290), the cause of these is unknown. After day 302 the lower ozone values returned to $\sim$24 ppb, this showed the high tropospheric BrO concentrations persisted for about five days.

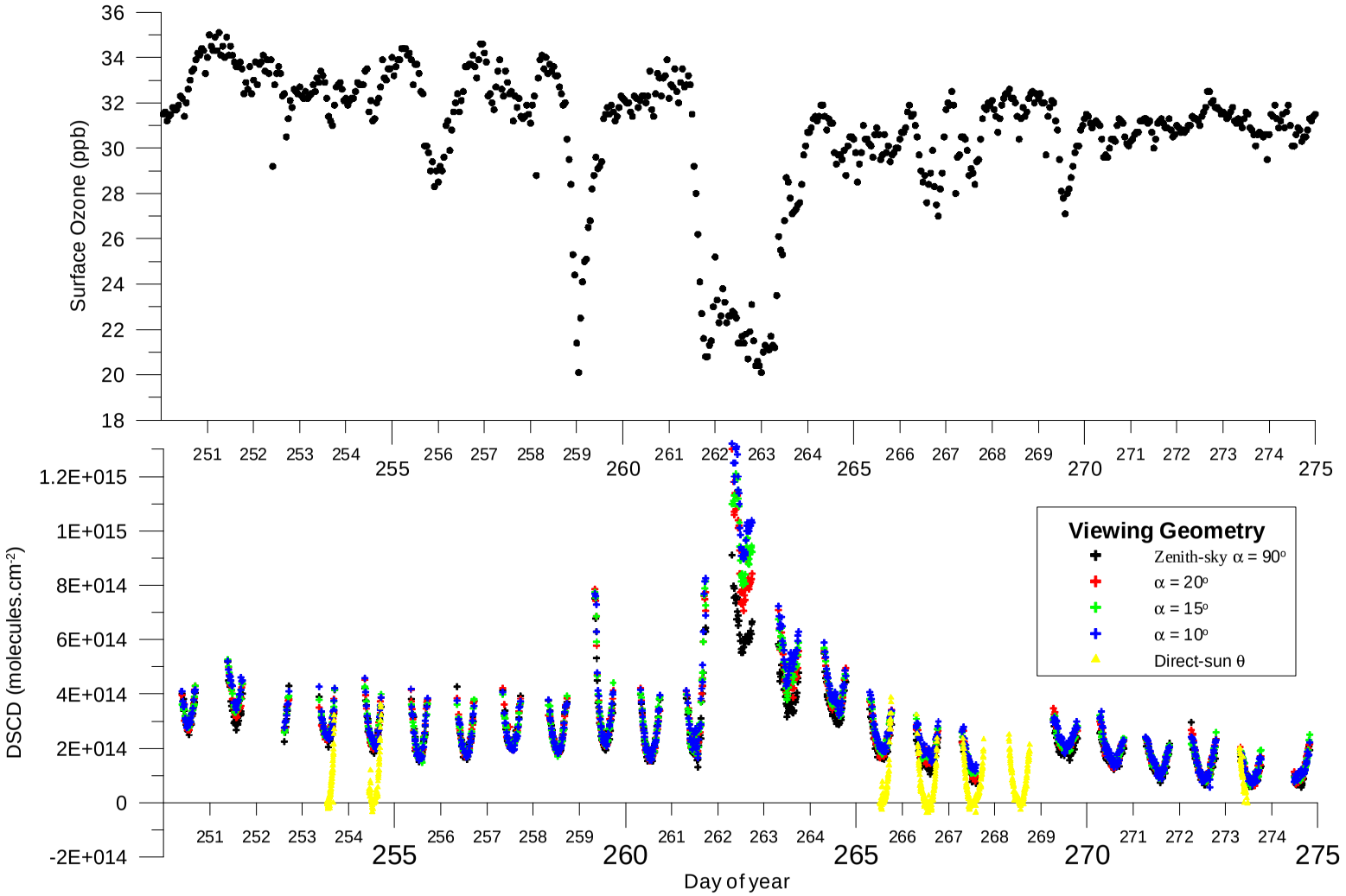


**Figure 8.2**: The top panel displays the surface ozone data made at Arrival Heights (*Oltmans*, 2003, personal communication). The lower panel DSCDs observations for the direct-sun and multi-axis (*Friess*, 2003, personal communication) viewing modes made at Arrival Heights, Antarctica for days 250 - 275 in the spring period 2002. Where there is clear separation in the DSCDs measured for different viewing angles of the multi-axis geometry is indicative of tropospheric BrO. Note that the upper plot axis of the surface ozone has a baseline of 18 ppb.

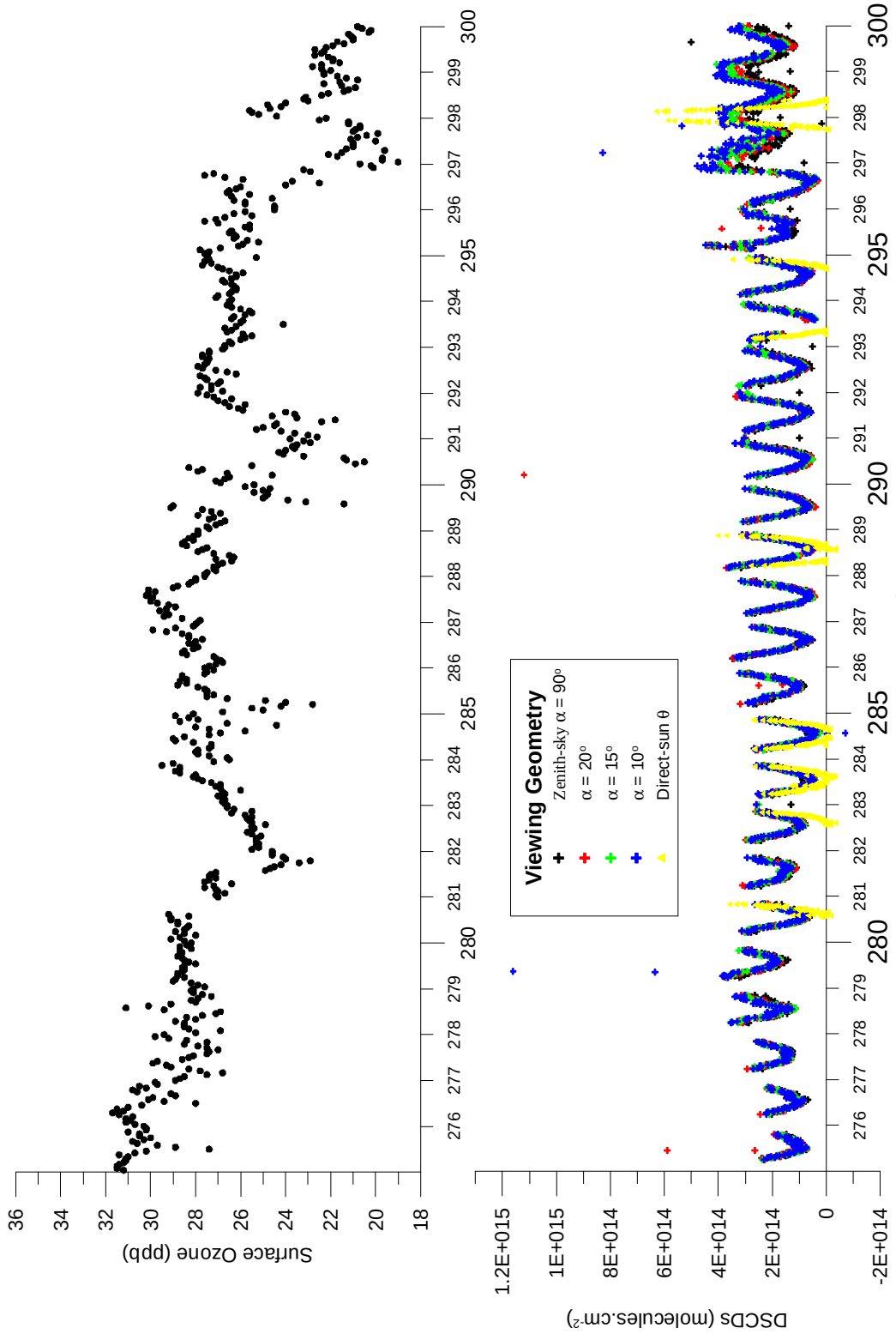


**Figure 8.3**: Same as figure 8.2 for days 275 - 300 at Arrival Heights, Antarctica in the spring period 2002.

## 8.3 Retrieved BrO Columns

Over the measurement campaign, nine sunrise and twelve sunset clear-sky twilight periods were examined. Zenith-sky measurements were made with an existing instrument at Arrival Heights, which has been making measurements since 1995 (for details on the zenith-sky measurements and analysis refer to (*Kreher et al.*, 1996; *Kreher*, 1996)). The zenith-sky measurements made with the multi-axis viewing instrument are identical, but shorter integration times for each angle are required, due to scanning over four angles. The column retrievals were performed using the zenith-sky DSCDs derived from the instrument devoted to just zenith-sky viewing.

A Lagrangian stationary chemical box model was used to determine a stratospheric *a priori* set of profiles. Unlike the mid-latitude case where there is a clear decrease in the profiles from 80° to 84° to 87°, the slower rate of change of SZA in the polar case meant that the diurnal variation was quite different. Seven profiles were chosen to describe the diurnal change (0°, 80°, 84°, 88°, 90°, 92° and 97°) with the model predicting a decrease in the profiles to occur after 90° for the sunset on day 280. There is almost no diurnal variation between 80° and 90° stratospheric profiles. There is however, a rapid decrease in the BrO profile from 90° to 92°, with almost no BrO present at 97°. Figure 8.4 shows the *a priori* diurnal variation for Arrival Heights in the spring used for the column retrievals in this work. The polar 0° tropospheric profile was assumed from balloon measurements made at Kiruna (*Fitzenberger et al.*, 2000) and a diurnal decrease was assumed.

The retrieval was conducted with the model atmosphere described up to 70 km, with 1 km model atmospheric layers (see Chapter 5 for details). The effects of refraction, molecular absorption, Rayleigh and Mie scattering were included. The aerosol extinction profiles for the stratosphere were provided by the Italian group who conducted and analysed Lidar measurements at McMurdo (4 km from Arrival Heights) as part of the NDSC program (*NDSC*, 2003). For the troposphere, an aerosol extinction profile from the winter climatology of Lauder was assumed (*Liley*, 2003), derived from back-scatter sondes. Ozone, temperature and pressure profiles were obtained from the ozonesonde measurements conducted from McMurdo as part of the NDSC program by a group from Wyoming University (*NDSC*, 2003).

An *a priori* error of 30 % was assumed in the construction of $\mathbf{S}_a$. The heavier reliance on the *a priori* compared to the Lauder data set, was due to the smaller SZA range for the DSCDs, especially at the beginning of the measurement period. The 30 % error was sufficient to provide a good fit for all of the measurements without overfitting them. The sensitivity of the column retrievals to changing the *a priori* error is explored in section 8.7 below.

The columns retrieved over the measurement campaign period at Arrival Heights are

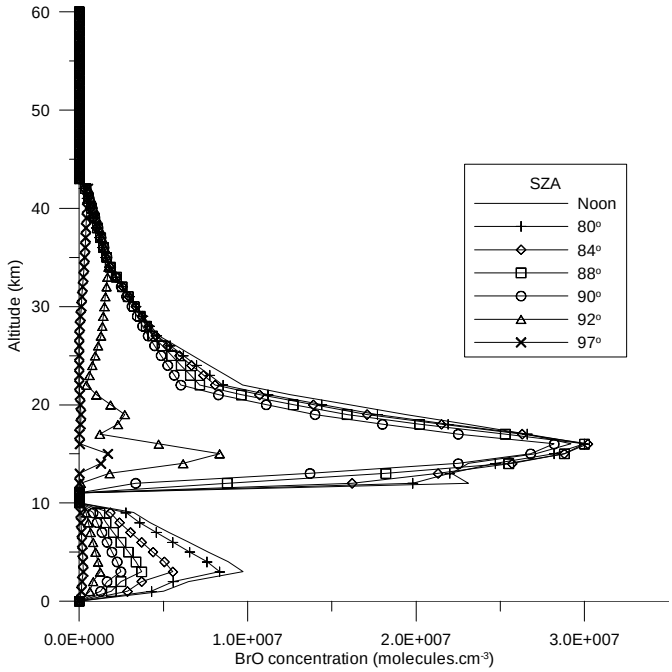


**Figure 8.4**: The stratospheric diurnal variation calculated using a Lagrangian box model (*Kreher et al.*, 2003) for sunset on day 280, 2002 at Arrival Heights, Antarctica. The polar 0° tropospheric profile is from polar balloon measurements (*Fitzenberger et al.*, 2000) and a diurnal decrease was assumed. These profiles are used as the *a priori* for the column retrievals from all measurements at Arrival Heights.

displayed in figure 8.5. The retrieved columns had a high variability between twilight measurements. The two twilight measurements on days 297 and 298 were conducted when the auxillary multi-axis and surface ozone measurements indicated increased tropospheric BrO.

| **Retrieved columns for BrO over Arrival Heights** | | | | | | |
|---|---|---|---|---|---|---|
| | Tropospheric Column | | | Stratospheric Column | | |
| Profile | 80° | 84° | 88° | 80° | 84° | 88° |
| Sunrise | 0.71±0.17 | 0.43±0.13 | 0.24±0.15 | 3.12±0.17 | 3.05±0.27 | 2.64±0.51 |
| Sunset | 0.24±0.17 | 0.22±0.13 | 0.31±0.13 | 2.57±0.29 | 2.71±0.29 | 2.51±0.51 |
| High BrO | 1.65±0.14 | 1.89±0.12 | 1.67±0.13 | 2.61±0.16 | 3.10±0.26 | 3.14±0.50 |

**Table 8.1**: The retrieved columns for the entire Arrival Heights data set is tabulated. The columns are expressed in units of $10^{13}$ molecules.cm$^{-2}$. The data set is divided into sunrise, sunset and high BrO (comprising the twilight measurements of the sunset day 297, and sunrise day 298).

Table 8.1 displays the variance weighted mean columns over all of the sunrise and sunset column retrievals excluding the high tropospheric BrO days of 297-298 for Arrival Heights. The two high tropospheric BrO twilight retrievals were combined and tabulated separately for comparison.

The stratospheric column retrievals for the background and high BrO retrievals were

within their respective errors. The variance weighted mean stratospheric BrO columns over Arrival Heights were similar to the mid-latitude 80° and 84° columns retrieved for winter over Lauder (see Chapter 7).

The mean sunrise stratospheric columns increase from 88°-80° SZA. The mean sunset stratospheric columns are lower than the mean sunrise columns and do not display a change with SZA. The change with SZA in the retrieved total columns for sunrise and sunset are displayed in figure 8.8 and are compared with the total columns retrieved from GOME (see section 8.4.1).

The variance weighted mean background tropospheric column over all days excluding the high tropospheric BrO days was $0.35\times10^{13}$ molecules.cm$^{-2}$. This is equivalent to 0.3 ppt if the BrO is assumed to be well mixed throughout the troposphere. The retrieved tropospheric column for the high BrO case of $\sim1.73\times10^{13}$ molecules.cm$^{-2}$ was almost a third of the total column. If this tropospheric BrO is assumed to all be located and well mixed in the lowermost 2 km boundary layer, consistent with a 'bromine explosion' event, it corresponds to a mixing ratio of 7.3 ppt. The Arrival Heights sunrise tropospheric columns were higher than the sunset columns.

The tropospheric columns retrieved for Arrival Heights over the spring period were higher than those seen at Lauder. The *a priori* tropospheric columns used for in the Lauder retrievals were slightly higher than those used for the Arrival Heights retrievals (with the tropopause being higher at mid-latitudes). The tropospheric *a priori* columns were $0.50\times10^{13}$ molecules.cm$^{-2}$ (0.4 ppt) and $0.45\times10^{13}$ molecules.cm$^{-2}$ (0.4 ppt) for the 80° profiles of Lauder and Arrival Heights retrievals respectively.

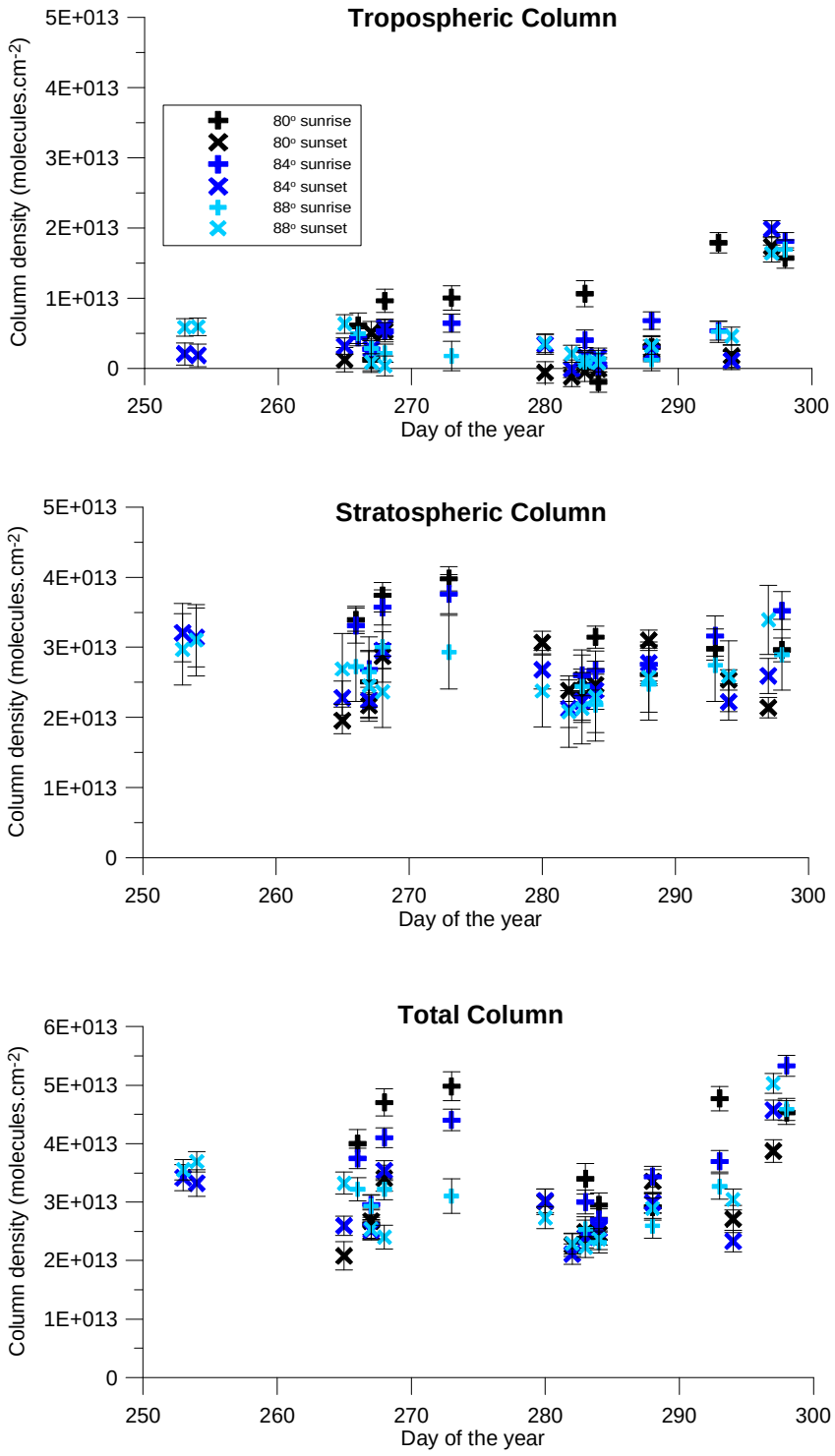


**Figure 8.5**: The retrieved tropospheric (upper plot), stratospheric (middle plot) and total columns (lower plot) for BrO over Arrival Heights, 2002 are displayed.

### 8.3.1 Retrieval Residuals

The model fit to the measured DSCDs is given by the retrieval residuals ($\mathbf{y}$-$\hat{\mathbf{y}}$). The mean residuals for the forward model fit to the measurements for all of the Arrival Heights column retrievals are displayed in figure 8.6. The upper plot of the mean direct-sun residuals show these to be quite noisy, relative to the residuals seen for the Lauder retrievals (refer to figure 7.6). The filter changes can account for some of the gross features (78° and 84°).

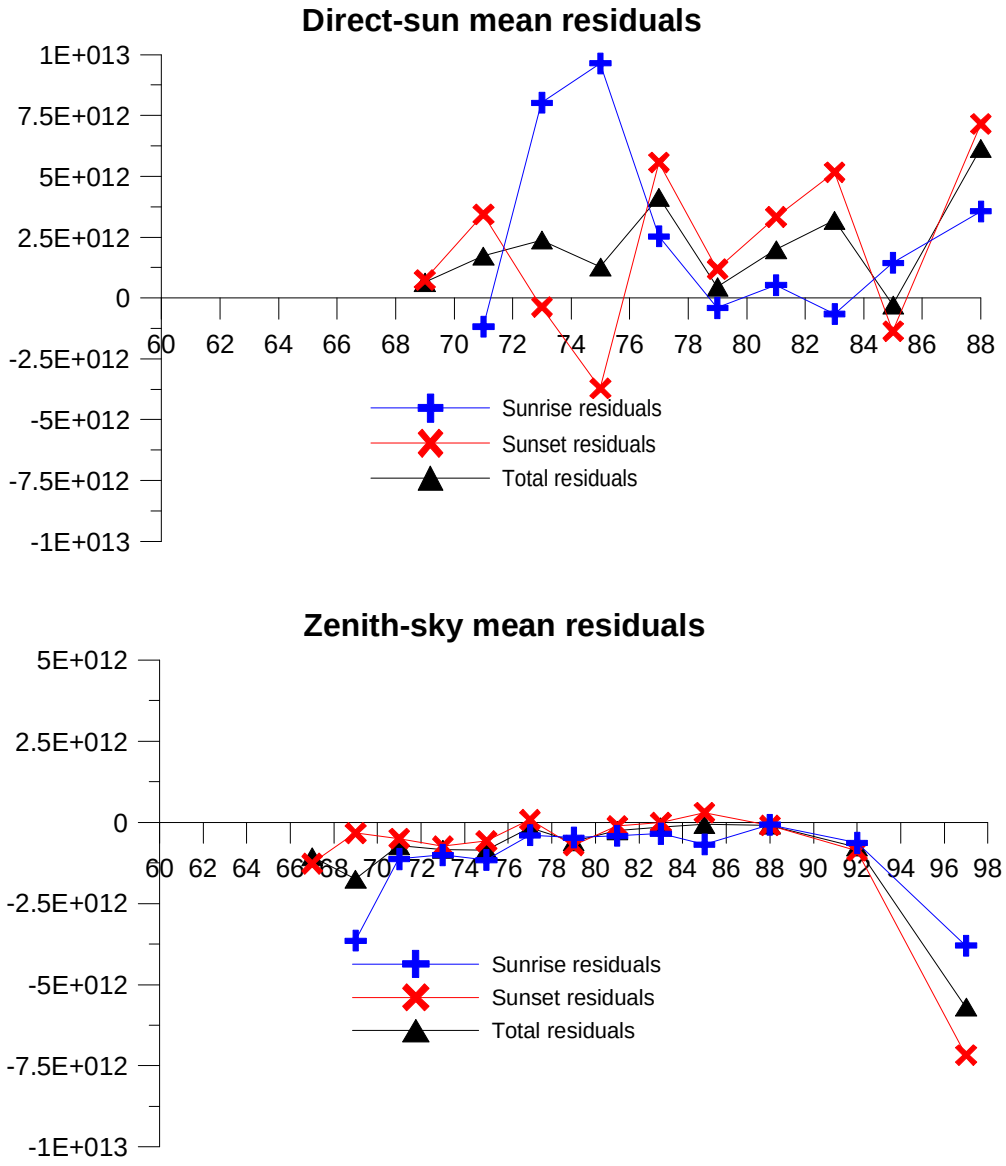


**Figure 8.6**: The mean residuals for all retrieval fits to the data. The upper plot displays the mean residuals for the direct-sun measurement fits. The lower plot displays the mean residuals for the zenith-sky measurement fits. Clear systematic errors are evident in the direct-sun fit with filter changes. The zenith-sky residuals show a systematic large residual for the highest SZA.

The high direct-sun residuals at low SZAs can be partially explained by only data at the end of the season contributing; the sun was too low at the beginning of the season (low SZAs not possible). Drift of the sun-tracking system, which was important for ensuring that direct-sun intensities were being measured and patchy cloud at noon also may be contributing factors. It is interesting to note that these residuals indicate that the calculated direct-sun DSCDs from the forward model seem to underestimate the measurements at most SZA.

The lower plot of the zenith-sky residuals show much less noise, and good forward model fits of the measurements. Similar to the residuals seen for Lauder, at high SZA the measurements are lower than the calculated DSCDs from the forward model. This is indicative that perhaps the forward model is no longer a good approximation to the true atmospheric radiative transfer at large SZA. Alternatively the low measurement intensities of these measurements may be introducing errors.

## 8.4 Comparison with GOME

At polar latitudes the 10.30 am overpass time for the ERS-2 satellite coincides with large SZAs at the beginning of the polar spring. It was therefore possible to directly compare the total columns retrieved in this work with those obtained by GOME (*Richter*, 2003, personal communication) at the same SZAs. Furthermore at this high latitude site, (78°S) the probability of concurrent measurements was greater than at mid-latitudes, due to the higher sampling of the polar regions with this satellite.

Figure 8.7 displays the sunrise total column comparison between the columns obtained using the ground-based zenith-sky and direct-sun measurements and the columns from the GOME experiment within 200 km of Arrival Heights. The qualitative agreement is good. The increase in the total column from day 284 onwards is seen with both methods. The agreement between the absolute columns for days 265-275 is fairly good. The agreement between the absolute columns is poorer after day 284. There are two possible explanations for this difference. The SZA for the GOME overpasses are less than 80° for these days so the two methods report columns at different times. The other possible explanation is that the Air Mass Factors (AMFs) (refer to section 4.4 for AMF details) for GOME are stratospheric only and it is during this time that high tropospheric BrO is being observed. Incorporation of tropospheric AMFs in the GOME data analysis would reduce the columns dramatically, especially if the BrO is located close to the surface, which is the case for the high tropospheric BrO amounts observed during 'bromine explosion' events.

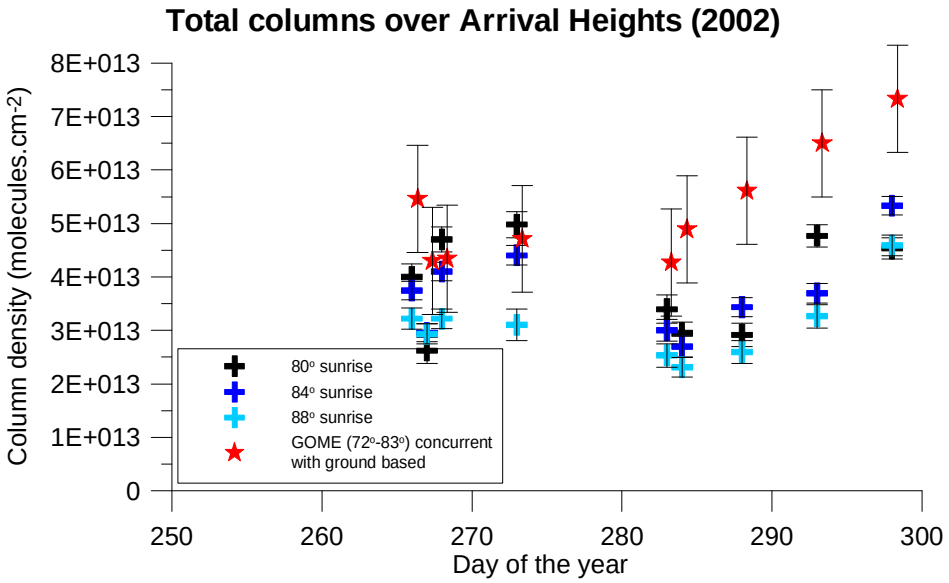


**Figure 8.7**: The retrieved total sunrise columns for BrO over Arrival Heights, 2002 are displayed along with the total columns measured by the GOME experiment.

### 8.4.1 Diurnal Variation

The diurnal variation of the mean sunrise and sunset retrieved total columns over all measurement days (excluding the high tropospheric BrO days) is displayed in figure 8.8. The sunrise columns increase with decreasing SZA. The sunset columns do not show a diurnal variation from 80° - 88° SZA. This is consistent with the diurnal variation shown in figure 8.4 calculated by the stationary chemical box model.

All of the concurrent GOME sunrise measurements are also displayed with their corresponding SZA. This comparison was complicated due to the fact that the total column was changing over the measurement period. Overall the GOME total columns are higher than the mean retrieved columns from the ground-based measurements where the SZAs are coincident. The agreement between GOME and the retrieved total columns is within the errors for the two methods. The high GOME columns at low SZA, were those at the end of the measurement period when there was the occurrence of high tropospheric BrO and stratospheric vortex columns. The absolute difference in the total columns between the GOME total columns and those retrieved from the ground-based measurements, where the comparison is possible, is about $0.8\times10^{13}$ molecules.cm$^{-2}$ when the mean columns for the entire spring are considered. This corresponds to a bias (high) of $\sim$20% in the 80° columns, slightly higher than the bias observed in the Lauder data-set.

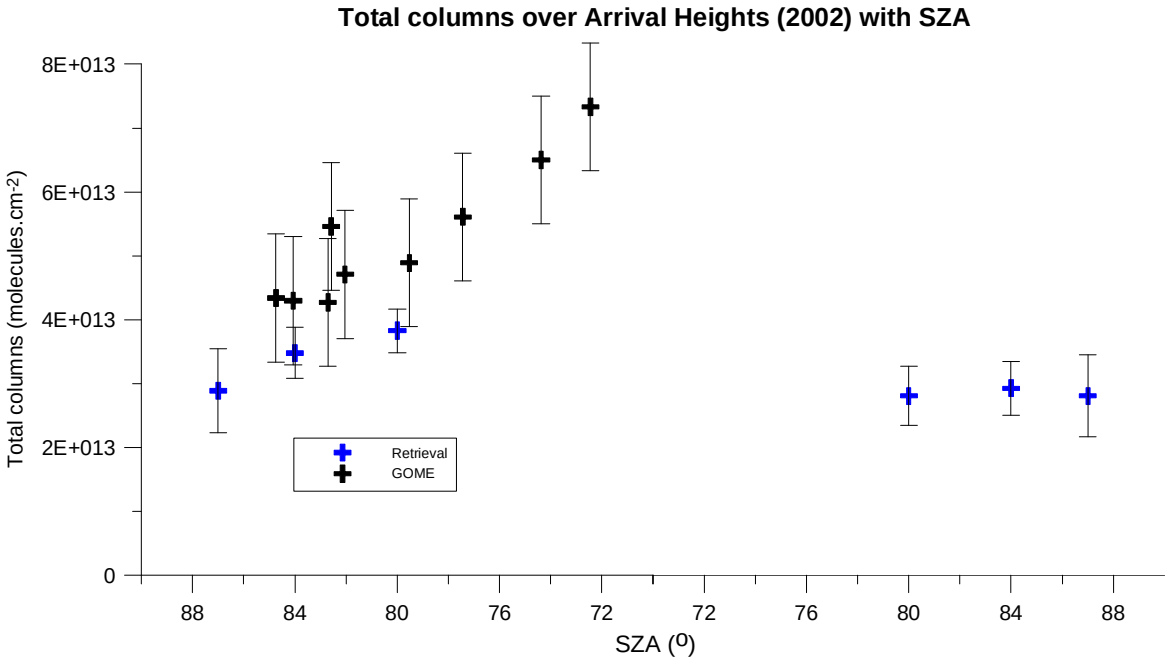


**Figure 8.8**: The variance weighted mean total columns retrieved from ground-based measurements at Arrival Heights, 2002 are displayed with SZA. The concurrent GOME measurements made over the same period are also displayed.

## 8.5 Comparison with UMETRAC

The coupled chemistry-climate model UMETRAC that was used to compare with the Lauder data set was also used to compare with the retrieved columns for Arrival Heights (*Struthers*, 2003, personal communication). The $Br_y$ assumed within the model was 20 ppt for the lower stratosphere, consistent with the calculations for Lauder.

The comparison of the UMETRAC model calculated columns with the retrieved columns is displayed in figure 8.9. The shaded parts of figure 8.9 indicate when Arrival Heights was under the stratospheric polar vortex (*Kreher et al.*, 2003). Most years Arrival Heights would be under the polar vortex for the entirety of the campaign period. 2002 however, was an unusual year and the vortex split meant that Arrival Heights was outside the vortex between days 265 and 284.

Overall the agreement was good between the UMETRAC model and the retrieved stratospheric columns for all angles studied. The discrepancies between the BrO columns calculated by the UMETRAC model and those retrieved from the ground-based measurements were when Arrival Heights was under the polar vortex at the end of the examined period. The lower temperatures associated with the polar vortex resulted in a decrease in the total amount of $NO_2$ (a strongly temperature dependent species) (*Otten et al.*, 1998). As the concentration of BrO is dependent on $NO_2$ concentrations, the depressed quantities of $NO_2$ result in elevated BrO levels. This is because less of the reservoir species

$BrONO_2$ is formed. The observed increase in the retrieved columns was expected when the polar vortex returned on day 284. The temperatures within the UMETRAC model did not change as dramatically as the real temperatures over Arrival Heights for 2002. The UMETRAC model did not capture the really low temperatures that were associated with being in the polar vortex, nor did it capture the high temperatures of the unusual vortex split of 2002. Within the UMETRAC model the polar vortex is stronger, but more tightly confined than in reality, thus Arrival Heights is always calculated as outside of vortex conditions. The agreement between the UMETRAC model and the retrieved columns was good when Arrival Heights was outside the polar vortex (thus 2002 was a fortuitous year for this comparison).

The sunrise columns calculated by the UMETRAC model and those retrieved were higher than the sunset columns (refer also to figure 8.8 for this diurnal variation). This is consistent with the enhanced reservoir release from BrCl compared with only HOBr at seen at Lauder and also the extended time spent at each SZA at this high latitude site.

The tropospheric columns calculated by the UMETRAC model were much lower than those retrieved over Arrival Heights. The tropospheric chemistry within the UMETRAC model does not include the unusual chemistry associated with the high BrO events in the polar regions.

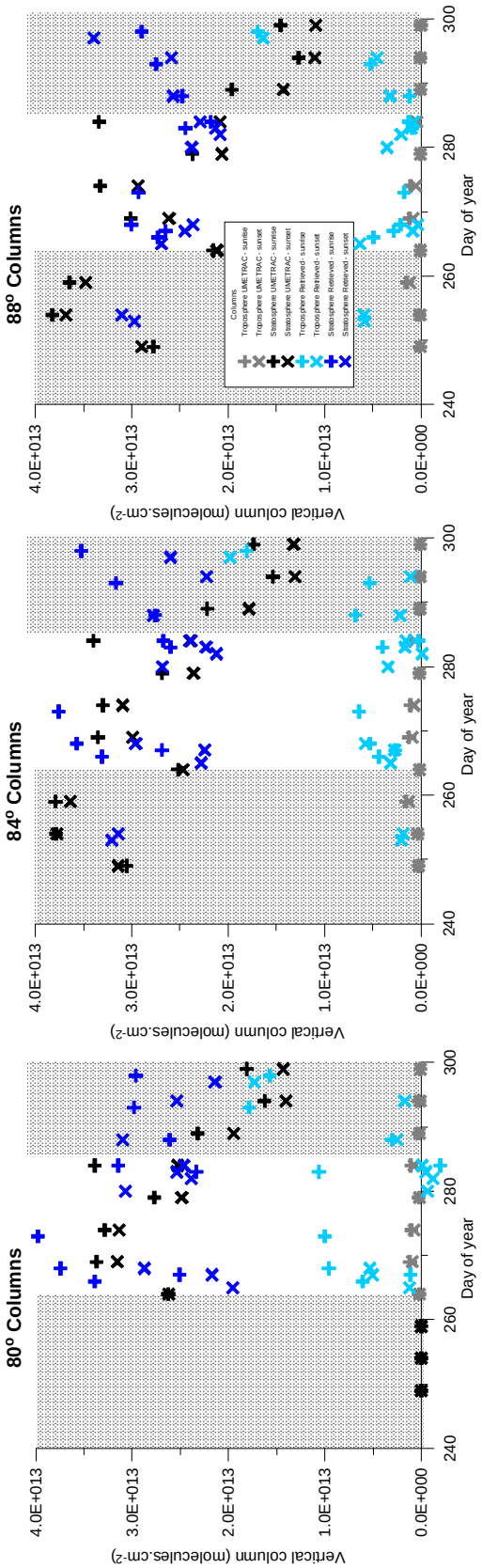


**Figure 8.9**: The retrieved tropospheric, stratospheric and total columns for BrO over Arrival Heights, 2002 are compared with the model calculations from the UMETRAC model. The left plot shows the comparison for the 80° columns, the middle plot for the 84° columns and the right plot for the 88° columns. The shaded portions of the plots indicate when Arrival Heights was under the polar vortex.

## 8.6 Retrieval Characterisation and Error Analysis

A complete error analysis and retrieval characterisation was performed on the Arrival Heights measurement set. Similar to the analysis performed for the Lauder measurements, the errors due to the retrieval and forward model parameters were calculated and these are displayed in table 8.2. In the same table the degrees of freedom and information content are given for the tropospheric and stratospheric columns for the SZAs of 80°, 84° and 88°.

| **Error breakdown for Arrival Heights retrievals (2002)** | | | | | | |
|---|---|---|---|---|---|---|
| | Tropospheric Column | | | Stratospheric Column | | |
| Retrieved Profile | 80° | 84° | 88° | 80° | 84° | 88° |
| Total Retrieval Error | 0.17 | 0.13 | 0.14 | 0.23 | 0.28 | 0.51 |
| Noise Error | 0.08 | 0.06 | 0.07 | 0.08 | 0.12 | 0.14 |
| Smoothing Error | 0.14 | 0.12 | 0.12 | 0.21 | 0.26 | 0.49 |
| Temperature Error | 0.02 | 0.01 | 0.005 | 0.03 | 0.01 | 0.01 |
| Pressure Error | 0.003 | 0.004 | 0.002 | 0.006 | 0.007 | 0.007 |
| Ozone Error | 0.0005 | 0.0002 | 0.0002 | 0.0006 | 0.0002 | 0.0003 |
| Aerosol Error | 0.005 | 0.002 | 0.002 | 0.006 | 0.003 | 0.003 |
| Information Content | 0.4 | 0.6 | 0.6 | 2.1 | 2.1 | 1.2 |
| Degrees of Freedom | 0.5 | 0.7 | 0.7 | 1.7 | 2.1 | 1.5 |

**Table 8.2**: The error breakdown for the entire Arrival Heights data set is tabulated. The error contribution to the retrieved columns is separated into noise and smoothing for the retrieval error. The forward model parameter errors of temperature, surface pressure, ozone and aerosol extinction are also tabulated. The errors are expressed in units of absolute vertical columns ($\times 10^{13}$ molecules.cm$^{-2}$). Also provided is the information content (bits) and the degrees of freedom for the whole data set.

The information content and degrees of freedom for signal for the Arrival Heights retrievals were different than those seen for the Lauder retrievals. The SZA range was quite different for the Arrival Heights retrievals compared to the Lauder retrievals. Early in the measurement period the retrievals had few or no independent pieces of information about the 80° columns, with the sun not reaching this SZA. The retrievals towards the end of the measurement period had a much larger SZA range, and with the long integration times, much more information about the 80°, and slightly less about the 88° columns. At Arrival Heights with the longer integration times and the elevation of the site above the surrounding horizon it was possible to retrieve 88° columns, as opposed to the 87° columns retrieved at Lauder. The information in the column retrievals for Arrival Heights was generally slightly better than that seen for Lauder. This was despite the lower *a priori* error which decreased the information in the retrievals. The lower measurement errors due to the longer integration times, and the ability to measure in both geometries to high SZAs provided information that wasn't possible at Lauder. The lower tropopause height of the Arrival Heights retrievals compared to the Lauder retrievals did reduce the

information content and degrees of freedom for the tropospheric columns. A tropopause height of 8.8 km (compared to ∼11 km for Lauder) was used for all of the polar retrievals. This height was derived by considering all of the ozonesonde data available for the spring period of 2002.

The averaging kernels for the tropospheric and stratospheric columns for the Arrival Heights retrievals were different than for the Lauder retrievals. This was a result of the different SZA ranges of the measurements. However, the main features are well represented by the exemplary averaging kernels given in Chapter 6. The tropospheric and stratospheric columns had really good separation for all days. The stratospheric column for the 88° profile was consistently the poorest described column, this being the cause of the large smoothing error for this column.

The forward model error parameter sensitivity at Arrival Heights was similar to that seen at Lauder for the temperature profile, the surface pressure and the ozone profile. The retrieved columns were an order of magnitude more sensitive to the aerosol extinction profile (though still negligible). This was due to the higher stratospheric aerosol extinction values and higher variability seen at Arrival Heights relative to Lauder. The higher stratospheric aerosol extinction values were typical of the colder temperatures of the polar spring stratosphere.

## 8.7 Retrieval Sensitivity Studies

The retrieval sensitivity to the *a priori* information over all of the Arrival Heights column retrievals was investigated. A test was also performed to demonstrate the effect of changing the cross-section set in the zenith-sky DSCD determination on the retrieved columns. The results of these tests are displayed in table 8.3 and the details are discussed below.

| **Difference from standard retrieval** | | | | | | |
|---|---|---|---|---|---|---|
| | Tropospheric Column | | | Stratospheric Column | | |
| Retrieved Profile | 80° | 84° | 88° | 80° | 84° | 88° |
| Standard Column | 0.52 | 0.44 | 0.39 | 2.68 | 2.86 | 2.62 |
| 10 % *a priori* error | -0.06 | -0.02 | -0.06 | 0.06 | -0.02 | -0.02 |
| 50 % *a priori* error | 0.03 | 0.002 | 0.02 | -0.02 | 0.02 | 0.002 |
| Old cross-section | -0.20 | -0.20 | -0.09 | 0.06 | 0.35 | 0.22 |

**Table 8.3**: The effect of changing the *a priori* information on the retrieved column amounts for the troposphere and stratosphere for Arrival Heights, 2002 is tabulated. The standard retrieved columns are the variance weighted means of all of the retrievals over Arrival Heights. The response is given as the difference from the standard retrieved column amounts ($\times 10^{13}$ molecules.cm$^{-2}$) calculated with an *a priori* error of 30 %. The retrieval response to assuming 10 % and 50 % error in the *a priori* information used in the construction of $\mathbf{S}_a$ is small. The retrieval response to using the older BrO cross-section from *Wahner et al.* (1988) in the calculation of zenith-sky DSCDs is significant.

The effect of reducing the *a priori* error of 30 % for the standard column retrievals to 10 % showed that the increased constraint reduced all of the columns slightly, with the exception of the 80° stratospheric column. Increasing the *a priori* error to 50 % resulted in a slight increase in the tropospheric columns and a negligible change in the stratospheric columns. The very small percentages associated with increasing the *a priori* error indicated that the 30 % error was sufficient to fit the measurements well. An *a priori* error of 50 % resulted in oscillatory behaviour in the column retrievals when the measurement range was small (at the beginning of the measurement campaign).

A sensitivity test where the zenith-sky DSCDs were derived using the older BrO cross-section of *Wahner et al.* (1988) was conducted. The direct-sun measurements were unaltered and determined by the more recent BrO cross-section of *Wilmouth et al.* (1999). The old cross-section resulted in increased zenith-sky DSCDs. Similar to what was seen in the Ring sensitivity test for the Lauder data set, (see section 7.6) the partitioning between the tropospheric and stratospheric columns was changed. The use of the older cross-section set did not produce a simple scalar increase in the DSCDs. The diurnal change of the DSCDs was therefore also affected. As a result the retrieved columns at the different angles responded differently. The use of the older cross-section resulted in a large decrease in the tropospheric columns and large increase in the stratospheric columns. The change in the tropospheric columns is an absolute decrease of $\sim 0.2 \times 10^{13}$ molecules.cm$^{-2}$, which is of the same magnitude as the total retrieval error.

The test using a different cross-section in the derivation of the DSCDs of one of the measurement sets highlighted the importance of consistency. The use of this retrieval method using DSCDs from different measurement geometries requires that the DSCDs are derived as consistently as possible to avoid these errors.

## 8.8 Summary

The stratospheric columns retrieved over the spring measurement campaign at Arrival Heights, Antarctica were similar to the columns observed at the mid-latitude site of Lauder during winter-spring. The variability of the stratospheric column retrievals was high, in part due to the unusual 2002 Antarctic spring. Higher stratospheric BrO columns were seen while Arrival Heights was under the polar vortex, which is typical polar spring conditions. The diurnal variation of the stratosphere for Arrival Heights was quite different than for Lauder. No diurnal variation was associated with the retrieved sunset stratospheric columns.

The tropospheric columns retrieved for Arrival Heights over the spring period were higher than those seen at Lauder. The sunrise columns were slightly higher than the sunset columns. A mean background (excluding the high tropospheric BrO days) tropospheric

column of $0.35\times10^{13}$ molecules.cm$^{-2}$ was determined. If the BrO is assumed to be well mixed throughout the troposphere this is equivalent to 0.3 ppt. The retrieved tropospheric column for the high BrO days was $\sim1.73\times10^{13}$ molecules.cm$^{-2}$. For a well mixed 2 km boundary layer this corresponds to a mixing ratio of 7.3 ppt.

The comparison with GOME was not straightforward as GOME measured at a different SZA each day. A further complicating issue was that the stratospheric column changed as the polar vortex returned. Also high tropospheric BrO at the end of the measurement period meant that the total columns were changing over the campaign period. The agreement between GOME total columns and the retrieved columns from ground-based measurements was good at the beginning of the measurement period. When the GOME measurement angles were higher and tropospheric columns larger, the agreement was poorer. The use of stratospheric AMFs in the GOME derivation of total columns may account for some of this difference. Qualitatively the agreement was good, with the data sets exhibiting similar variations. Overall the GOME measurements were about $0.8\times10^{13}$ molecules.cm$^{-2}$ higher when the mean columns were considered for SZA where a comparison was possible.

The retrieved columns compared very well with the UMETRAC model with a $Br_y$ loading of 20 ppt. The tropospheric columns were not well calculated by the UMETRAC model, due to the limited tropospheric chemistry within the model. The unusual Antarctic polar vortex behaviour of 2002 allowed for a comparative study, showing good agreement with the measurements when Arrival Heights was not under the polar vortex. The agreement was poorer when Arrival Heights was under the polar vortex.

The error analysis for the whole Arrival Heights data set showed sensitivity to the forward model parameters of the temperature profile, the surface pressure, the ozone and aerosol extinction profiles to be negligible. Relative to the Lauder retrievals the Arrival Heights retrievals were about an order of magnitude more sensitive to the aerosol extinction profile (but still negligible) due to the higher variability of this profile in the polar region. The retrieval errors were similar for the Arrival Heights and Lauder retrievals.

The information content and degrees of freedom for signal demonstrated that the measurement set for Arrival Heights had good information for the tropospheric and stratospheric columns. This was largely due to the ability to measure to high SZAs at the Arrival Heights site and because of the longer integration times.

The column retrievals demonstrated good stability to increasing the *a priori* error. Decreasing the *a priori* error resulted in larger changes in the retrieved columns as the retrievals were constrained more by the *a priori* information. A test where an older cross-section set was used to evaluate the zenith-sky DSCDs had a dramatic effect on all of the retrieved columns, illustrating the necessity of consistency in the derivation of DSCDs from different instruments.

## Chapter 9

# Conclusions

Ground-based UV-Visible spectroscopic measurements were made in the two complementary viewing modes of direct-sun and zenith-sky. The use of DSCDs from two different instruments allowed each instrument and spectral fitting procedure to be optimized, without compromising the subsequent column retrieval. The radiative transfer model developed in this work was validated against other existing models used for atmospheric radiative transfer, agreeing within 3 % of the DISORT model.

The retrieval characterisation displayed how combining measurements provided enhanced sensitivity over all altitudes. The direct-sun measurements provided sensitivity to the troposphere, while the zenith-sky measurements were more sensitive to the stratosphere. A resolution of 5-15 km was achieved for the troposphere and for the stratosphere the resolution was between 20-40 km.

Measurements conducted at Lauder from 2001-2003 allowed the retrieval of tropospheric and stratospheric columns at 80°, 84° and 87° SZA. The stratospheric seasonal variation was well captured by the retrieved stratospheric columns. The BrO columns retrieved for winter were larger than those seen for summer, consistent with stratospheric BrO concentrations being driven by the $Br_y$ maxima and the $NO_2$ minima. The diurnal variation of stratospheric BrO over Lauder was also retrieved. The decrease in the stratospheric column from 80° to 84° to 87° was seen in both the sunrise and sunset column retrievals. The sunrise columns, while smaller than the sunset columns for 87°, were larger for the 80° columns.

The direct-sun and zenith-sky measurements for Lauder are consistent with a variable ubiquitous tropospheric BrO mixing ratio between 0.0 - 0.9 ppt with an error of 0.2 ppt. The majority of the BrO tropospheric column retrievals over Lauder were below $0.8\times10^{13}$ molecules.cm$^{-2}$ or 0.6 ppt if BrO is assumed to be uniformly mixed throughout the troposphere.

A measurement campaign was conducted at Arrival Heights in the spring of 2002. Tropospheric and stratospheric columns were retrieved at 80°, 84° and 88° SZA. The variability of the stratospheric column retrievals for Arrival Heights was high, in part due to the unusual 2002 Antarctic spring. Higher stratospheric BrO columns at 80°, 84° and 88° SZA were seen while Arrival Heights was under the polar vortex. The diurnal

variation of the stratosphere for Arrival Heights was quite different than for Lauder. No diurnal variation was associated with the retrieved sunset stratospheric columns.

The tropospheric columns retrieved for Arrival Heights over the spring period were higher than those retrieved for Lauder. A mean background tropospheric column of $0.35\times10^{13}$ molecules.cm$^{-2}$ or 0.3 ppt (if uniformly mixed throughout the troposphere) was determined. The tropospheric BrO column of an observed 'bromine explosion' event was $\sim1.73\times10^{13}$ molecules.cm$^{-2}$. This corresponds to a mixing ratio of 7.3 ppt if uniformly mixed throughout the boundary layer.

The comparison of the retrieved total columns with the total columns from GOME was not straightforward because of the different SZAs of the GOME and ground-based column retrievals. The qualitative agreement between the retrieved columns and GOME was good at both measurement locations. Where a comparison was possible, the GOME columns overall were higher than the retrieved 80° total columns from the ground-based measurements for both Lauder and Arrival Heights.

The UMETRAC model showed the retrieved stratospheric columns over Lauder to be consistent with a $Br_y$ loading of 20 ppt in the lower stratosphere. The seasonality and the diurnal variations were consistent between the model and retrieved stratospheric columns. At Arrival Heights the UMETRAC model with 20 ppt in the lower stratosphere showed good agreement with the retrieved columns when Arrival Heights was not under the polar vortex.

## 9.1 Outlook

Stratospheric and tropospheric sensitivity was achieved in this work by combining two ground-based viewing geometries. The addition of the multi-axis geometry would be advantageous with this instrument's sensitivity to the troposphere at noon. This would require a multiple scattering radiative transfer description to be incorporated into the forward model.

The Arrival Heights data set had really good information content as a result of being able to measure up to 89° in the direct-sun, and the zenith-sky measurements up to 95°. Measurements at a high altitude, marine tropical site such as Mauna Loa would have a very large SZA range, so there would potentially be an increased amount of information. Observations at a marine site would be interesting for the question of the role that BrO plays in the remote marine boundary layer.

Tests of the seasonality of the stratospheric columns over Lauder illustrated the value of having a large data set. If direct-sun measurements were made routinely alongside zenith-sky and multi-axis measurements, many more modelling and satellite comparative exercises would be possible.

An improvement in the light throughput of the instruments would facilitate measurements to higher SZAs. For the direct-sun an increase in the aperture, detector area and an improvement in the tracking system would allow routine measurements to be made to high SZA. An improvement in the $O_4$ cross-section would also be advantageous. For the zenith-sky measurements; a larger area detector and improved ozone cross-sections would improve the retrieval.

The error analysis would be improved if the retrieval was performed from the spectra, instead of having a two step retrieval. The lack of transparency of the errors in the DOAS retrieval into the final retrieved columns is inhibiting.

# References


Aben, I., D. M. Stam, and F. Helderman, The Ring effect in skylight polarisation, *Geophysical Research Letters*, *28*(3), 519–522, 2001.

Alicke, B., K. Hebestreit, J. Stutz, and U. Platt, Iodine oxide in the marine boundary layer, *Nature*, *397*(6720), 572–573, 1999.

Aliwell, S. R., et al., Analysis for BrO in zenith-sky spectra: An intercomparison exercise for analysis improvement, *Journal of Geophysical Research*, *107*(D14), doi:10.1029/2001JD000329, 2002.

Allan, B. J., G. McFiggans, J. M. C. Plane, and H. Coe, Observations of iodine monoxide in the remote marine boundary layer, *Journal of Geophysical Research*, *105*(D11), 14363–14369, 2000.

Allen, D. R., R. M. Bevilacqua, G. E. Nedoluha, C. E. Randall, and G. L. Manney, Unusual stratospheric transport and mixing during the 2002 Antarctic winter, *Geophysical Research Letters*, *30*, doi:10.1029/2003GL017117, in press, 2003.

Anderson, J. G., D. W. Toohey, and W. H. Brune, Free radicals within the Antarctic vortex: The role of CFCs in Antarctic ozone loss, *Science*, *251*, 39–46, 1991.

Anthony, S. E., T. B. Onasch, R. T. Tisdale, R. S. Disselkamp, M. A. Tolbert, and J. C. Wilson, Laboratory studies of ternary $H_2SO_4/HNO_3/H_2O$ particles: Implications for polar stratospheric cloud formation, *Journal of Geophysical Research*, *102*(D9), 10777–10784, 1997.

Atkins, P. W., *Physical Chemistry*. Oxford University Press, Oxford, 5th edn., 1994.

Austin, J., A three-dimensional coupled chemistry-climate model simulation of past stratospheric trends, *Journal of the Atmospheric Sciences*, *59*(2), 218–232, 2002.

Barrie, L. A., J. W. Bottenheim, R. C. Schnell, P. J. Crutzen, and R. A. Rasmussen, Ozone destruction and photochemical reactions at polar sunrise in the lower Arctic atmosphere, *Nature*, *334*, 138–141, 1988.

Barrie, L. A., S. M. Li, D. L. Toom, S. Landsberger, and W. Sturges, Lower tropospheric measurements of halogens, nitrates, and sulphur oxides during Polar Sunrise Experiment 1992., *Journal of Geophysical Research*, *99*(D12), 25453–25467, 1994.

Bates, D. R., and M. Nicolet, Atmospheric hydrogen, *Publications of the Astronomical Society of the Pacific*, *62*, 106–110, 1950.

Bodeker, G., I. Boyd, and W. Matthews, Trends and variability in vertical ozone and temperature profiles measured by ozonesondes at Lauder, New Zealand: 1986-1996, *Journal of Geophysical Research*, *103*(D22), 28661–28681, 1998.

Bodeker, G. E., and R. L. McKenzie, Modelling the effects of clouds on surface spectral UV irradiance, in *Atmospheric Ozone, Proceedings of the XVIII Quadrennial Ozone Symposium*, edited by R. D. Bojkov, and G. Visconti, vol. 2, pp. 841–844, L'Aquila, Italy. Parco Scientifico e Tecnologico d'Abruzzo, 1996.

Bodeker, G. E., B. J. Connor, J. B. Liley, and W. A. Matthews, The global mass of ozone: 1978-1998, *Geophysical Research Letters*, *28*(14), 2819–2822, 2001.

Bottenheim, J. W., and A. G. Gallant, Measurements of $NO_y$ species and $O_3$ at 82° N latitude, *Geophysical Research Letters*, *13*(1), 113–116, 1986.

Bottenheim, J. W., L. A. Barrie, E. Atlas, L. E. Heidt, H. Niki, R. A. Rasmussen, and P. B. Shepson, Depletion of lower tropospheric ozone during Arctic spring - the Polar Sunrise Experiment 1988, *Journal of Geophysical Research*, *95*(D11), 18555–18568, 1990.

Brewer, A., C. T. McElroy, and J. Kerr, Nitrogen dioxide concentration in the atmosphere, *Nature*, *246*, 129–133, 1973.

Bucholtz, A., Rayleigh-scattering calculations for the terrestrial atmosphere, *Applied Optics*, *34*(15), 2765–2773, 1995.

Burrows, J., et al., The Global Ozone Monitoring Experiment (GOME): Mission concept and first scientific results, *Journal of the Atmospheric Sciences*, *56*(2), 151–175, 1999.

Butler, J. H., S. A. Montzka, A. D. Clarke, J. M. Lobert, and J. W. Elkins, Growth and distribution of halons in the atmosphere, *Journal of Geophysical Research*, *103*(D1), 1503–1511, 1998.

Chapman, S., On ozone and atomic oxygen in the upper atmosphere., *Philosophical Magazine and Journal of Science*, *7*, 369–383, 1930.

Chartrand, D. J., and J. C. McConnell, Heterogeneous chemistry and the $O_3$ budget in the lower mid-latitude stratosphere, *Journal of Atmospheric Chemistry*, *35*(2), 109–149, 1999.

Chipperfield, M., D. Cariolle, P. Simon, R. Ramaroson, and D. Lary, A three-dimensional modeling study of trace species in the Arctic lower stratosphere during winter 1989-1990, *Journal of Geophysical Research*, *98*(D4), 7199–7218, 1993.

Chipperfield, M. P., T. Glassup, I. Pundt, and O. V. Rattigan, Model calculations of stratospheric OBrO indicating very small abundances, *Geophysical Research Letters*, *25*(19), 3575–3578, 1998.

Connor, B. J., A. Parrish, J. J. Tsou, and M. P. McCormick, Error analysis for the ground-based microwave ozone measurements during STOIC, *Journal of Geophysical Research*, *100*(D5), 9283–9291, 1995.

Crutzen, P. J., The influence of nitrogen oxides on the atmospheric ozone content, *Quarterly Journal of the Royal Meteorological Society*, *96*, 320–325, 1970.

Crutzen, P. J., Ozone production rates in an oxygen-hydrogen-nitrogen oxide atmosphere, *Journal of Geophysical Research*, *76*(30), 7311–7327, 1971.

Crutzen, P. J., The possible importance of CSO for the sulfate layer of the stratosphere., *Geophysical Research Letters*, *3*(2), 73–76, 1976.

Daniel, J. S., S. Solomon, R. W. Portmann, and R. R. Garcia, Stratospheric ozone destruction: The importance of bromine relative to chlorine, *Journal of Geophysical Research*, *104*(D19), 23871–23880, 1999.

Danilin, M. Y., and J. C. McConnell, Stratospheric effects of bromine activation on/in sulfate aerosol, *Journal of Geophysical Research*, *100*(D6), 11237–11243, 1995.

Danilin, M. Y., N. D. Sze, M. K. W. Ko, J. M. Rodriguez, and M. J. Prather, Bromine-chlorine coupling in the Antarctic ozone hole, *Geophysical Research Letters*, *23*(2), 153–156, 1996.

Dickerson, R. R., K. P. Rhoads, T. P. Carsey, S. J. Oltmans, J. P. Burrows, and P. J. Crutzen, Ozone in the remote marine boundary layer: A possible role for halogens, *Journal of Geophysical Research*, *104*(D17), 21385–21395, 1999.

Dobson, G. M. B., Forty years' research on atmospheric ozone at Oxford: A history., *Applied Optics*, *7*(3), 387–405, 1968.

Ebinghaus, R., H. H. Kock, C. Temme, J. W. Einax, A. G. Lowe, A. Richter, J. P. Burrows, and W. H. Schroeder, Antarctic springtime depletion of atmospheric mercury, *Environmental Science and Technology*, *36*(6), 1238–1244, 2002.

Erle, F., U. Platt, and K. Pfeilsticker, Measurement of OBrO upper limits in the nighttime stratosphere, *Geophysical Research Letters*, *27*(15), 2217–2220, 2000.

Fahey, D. W., et al., In situ measurements constraining the role of sulphate aerosols in mid-latitude ozone depletion., *Nature*, *363*, 509–514, 1993.

Farman, J. C., B. G. Gardiner, and J. D. Shanklin, Large losses of total ozone in Antarctica reveal seasonal $ClO_x/NO_x$ interaction., *Nature*, *315*, 207–210, 1985.

Ferlemann, F., et al., Stratospheric BrO profiles measured at different latitudes and seasons - instrument description, spectral analysis and profile retrieval, *Geophysical Research Letters*, *25*(20), 3847–3850, 1998.

Finlayson-Pitts, B. J., and J. N. Pitts, *Chemistry of the Upper and Lower Atmosphere. Theory, Experiments and Applications*. Academic Press, San Diego, 1999.

Finlayson-Pitts, B. J., F. E. Livingston, and H. N. Berko, Ozone destruction and bromine photochemistry at ground level in the Arctic spring, *Nature*, *343*, 622–625, 1990.

Fish, D. J., Measurements of stratospheric composition using ultraviolet and visible spectroscopy, Ph.D. thesis, University of Cambridge, 1994.

Fish, D. J., and R. L. Jones, Rotational Raman-scattering and the Ring effect in zenith-sky spectra, *Geophysical Research Letters*, *22*(7), 811–814, 1995.

Fish, D. J., R. L. Jones, and E. K. Strong, Midlatitude observations of the diurnal variation of stratospheric BrO, *Journal of Geophysical Research*, *100*(D9), 18863–18871, 1995.

Fish, D. J., S. R. Aliwell, and R. L. Jones, Mid-latitude observations of the seasonal variation of BrO .2. interpretation and modelling study, *Geophysical Research Letters*, *24*(10), 1199–1202, 1997.

Fitzenberger, R., H. Bosch, C. Camy-Peyret, M. P. Chipperfield, H. Harder, U. Platt, B. M. Sinnhuber, T. Wagner, and K. Pfeilsticker, First profile measurements of tropospheric BrO, *Geophysical Research Letters*, *27*(18), 2921–2924, 2000.

Fraser, P., Chemistry of stratospheric ozone and ozone depletion, *Australian Meteorological Magazine*, *46*(3), 185–193, 1997.

Friess, U., Spectroscopic measurements of atmospheric trace gases at Neumayer-station, Antarctica, Ph.D. thesis, University of Heidelberg, 2001.

Friess, U., Personal communication. Off-axis spectroscopic data from Arrival Heights (78°S)., 2003.

Grainger, J. F., and J. Ring, Anomalous Fraunhofer line profiles, *Nature*, *193*, 762, 1962.

Hansen, J. E., and L. D. Travis, Light scattering in planetary atmospheres, *Space Science Reviews*, *16*, 527–610, 1974.

Harder, H., et al., Stratospheric BrO profiles measured at different latitudes and seasons - atmospheric observations, *Geophysical Research Letters*, *25*(20), 3843–3846, 1998.

Harder, H., et al., Comparison of measured and modeled stratospheric BrO: Implications for the total amount of stratospheric bromine., *Geophysical Research Letters*, *27*(22), 3695–3698, 2000.

Hausmann, M., and U. Platt, Spectroscopic measurement of bromine oxide and ozone in the high Arctic during Polar Sunrise Experiment 1992., *Journal of Geophysical Research*, *99*(D12), 25399–25413, 1994.

Hebestreit, K., J. Stutz, D. Rosen, V. Matveiv, M. Peleg, M. Luria, and U. Platt, DOAS measurements of tropospheric bromine oxide in mid-latitudes, *Science*, *283*(5398), 55–57, 1999.

Hendrick, F., Personal communication. Radiative transfer intercomparison workshop., 2003.

Hendricks, J., E. Lippert, H. Petry, and A. Ebel, Heterogeneous reactions on and in sulfate aerosols: Implications for the chemistry of the midlatitude tropopause region, *Journal of Geophysical Research*, *104*(D5), 5531–5550, 1999.

Hintsa, E. J., et al., Dehydration and denitrification in the Arctic polar vortex during the 1995-1996 winter, *Geophysical Research Letters*, *25*(4), 501–504, 1998.

Honninger, G., and U. Platt, Observations of BrO and its vertical distribution during surface ozone depletion at alert, *Atmospheric Environment*, *36*, 2481–2489, 2002.

Hoppel, K. W., R. M. Bevilacqua, D. R. Allen, G. Nedoluha, and C. E. Randall, POAM III observations of the anomalous 2002 Antarctic ozone hole, *Geophysical Research Letters*, *30*(7), doi:10.1029/2003GL016899, 2003.

Iraci, L. T., A. M. Middlebrook, M. A. Wilson, and M. A. Tolbert, Growth of nitric-acid hydrates on thin sulfuric-acid films, *Geophysical Research Letters*, *21*(10), 867–870, 1994.

Iraci, L. T., A. M. Middlebrook, and M. A. Tolbert, Laboratory studies of the formation of polar stratospheric clouds - nitric-acid condensation on thin sulfuric-acid films, *Journal of Geophysical Research*, *100*(D10), 20969–20977, 1995.

Jiang, Y., Y. L. Yung, and S. P. Sander, Detection of tropospheric ozone by remote sensing from the ground, *Journal of Quantitative Spectroscopy and Radiative Transfer*, *57*(6), 811–818, 1997.

Jones, R. L., and J. A. Pyle, Observations of $CH_4$ and $N_2O$ by the NIMBUS 7 SAMS: A comparison with in situ data and two-dimensional numerical model calculations., *Journal of Geophysical Research*, *89*(D4), 5263–5279, 1984.

Junge, C. E., C. W. Chagnon, and J. E. Manson, Stratospheric aerosols, *Journal of Meteorology*, *18*, 81–108, 1961.

Kemnitzer, H., S. Hilgers, G. Schwarz, T. Steck, T. v. Clarmann, M. Hopfner, and K. Ressel, Trace gas retrieval including horizontal gradients, *Advances in Space Research*, *29*(11), 1631–1636, 2002.

Kneizys, F. X., J. H. J. Chetwynd, S. A. Clough, E. P. Shettle, L. W. Abreu, R. W. Fenn, W. O. Gallery, and J. E. A. Selby, Atmospheric transmittance/radiance: Computer code lowtran 6, Tech. Rep. AFGL-TR-83-0187, Air force Geophysics Laboratory, 1983.

Kourtidis, K., R. Borchers, and P. Fabian, Vertical distribution of methyl bromide in the stratosphere, *Geophysical Research Letters*, *25*(4), 505–508, 1998.

Kourtidis, K. A., R. Borchers, P. Fabian, and J. Harnisch, Carbonyl sulfide (COS) measurements in the Arctic polar vortex, *Geophysical Research Letters*, *22*(4), 393–396, 1995.

Kreher, K., Spectroscopic measurements of atmospheric OClO, BrO and $NO_2$ and their relation to Antarctic ozone depletion, Ph.D. thesis, University of Heidelberg, 1996.

Kreher, K., J. G. Keys, P. V. Johnston, U. Platt, and X. Liu, Ground-based measurements of OClO and HCl in Austral spring 1993 at Arrival Heights, Antarctica, *Geophysical Research Letters*, *23*(12), 1545–1548, 1996.

Kreher, K., P. V. Johnston, S. W. Wood, B. Nardi, and U. Platt, Ground-based measurements of tropospheric and stratospheric BrO at Arrival Heights, Antarctica, *Geophysical Research Letters*, *24*(23), 3021–3024, 1997.

Kreher, K., et al., Measured and modelled chlorine partitioning in the Antarctic stratosphere 1998 - 2002, *Journal of Atmospheric Science*, Submitted, 2003.

Lary, D. J., Gas phase atmospheric bromine photochemistry, *Journal of Geophysical Research*, *101*(D1), 1505–1516, 1996.

Lary, D. J., Catalytic destruction of stratospheric ozone, *Journal of Geophysical Research*, *102*(D17), 21515–21526, 1997.

Lary, D. J., and R. Toumi, Halogen-catalyzed methane oxidation, *Journal of Geophysical Research*, *102*(D19), 23421–23428, 1997.

Lary, D. J., M. P. Chipperfield, R. Toumi, and T. Lenton, Heterogeneous atmospheric bromine chemistry, *Journal of Geophysical Research*, *101*(D1), 1489–1504, 1996.

Lee, A. M., R. L. Jones, I. Kilbane-Dawe, and J. A. Pyle, Diagnosing ozone loss in the extratropical lower stratosphere, *Journal of Geophysical Research*, *107*(D11), doi:10.1029/2001JD000538, 2002.

Leser, H., G. Honninger, and U. Platt, Max-doas measurements of BrO and $NO_2$ in the marine boundary layer, *Geophysical Research Letters*, *30*(10), doi:10.1029/2002GL015811, 2003.

Liley, J. B., Personal communication regarding the aerosol data and climatology over Lauder (45°S) from lidar and backscatter sondes., 2003.

Liley, J. B., P. V. Johnston, R. L. McKenzie, A. J. Thomas, and I. S. Boyd, Stratospheric $NO_2$ variations from a long time series at Lauder, New Zealand, *Journal of Geophysical Research*, *105*(D9), 11633–11640, 2000.

Livesey, J. J., and W. G. Read, Direct retrieval of line-of-sight atmospheric structure from limb sounding observations, *Geophysical Research Letters*, *27*(6), 891–894, 2000.

Lu, J. Y., et al., Magnification of atmospheric mercury deposition to polar regions in springtime: the link to tropospheric ozone depletion chemistry, *Geophysical Research Letters*, *28*(17), 3219–3222, 2001.

McConnell, J. C., G. S. Henderson, L. Barrie, J. Bottenheim, H. Niki, C. H. Langford, and E. M. J. Templeton, Photochemical bromine production implicated in Arctic boundary-layer ozone depletion., *Nature*, *355*, 150–152, 1992.

McCormick, M. P., H. M. Steele, P. Hamill, W. P. Chu, and T. J. Swissler, Polar stratospheric cloud sighting by SAM II, *Journal of the Atmospheric Sciences*, *39*, 1387–1397, 1982.

McElroy, C. T., C. A. McLinden, and J. C. McConnell, Evidence for bromine monoxide in the free troposphere during the Arctic polar sunrise, *Nature*, *397*(6717), 338–341, 1999.

McKenzie, R., P. Johnston, C. T. McElroy, J. Kerr, and S. Solomon, Altitude distributions of stratospheric constituents from ground-based measurements at twilight, *Journal of Geophysical Research*, *96*(D8), 15499–15511, 1991.

Mellouki, A., R. K. Talukdar, and C. J. Howard, Kinetics of the reactions of HBr with $O_3$ and $HO_2$ - the yield of HBr from $HO_2$+BrO, *Journal of Geophysical Research*, *99*(D11), 22949–22954, 1994.

Mie, G., *Annales Physics*, *25*(4), 337, 1908.

Miller, H. L., A. Weaver, R. W. Sanders, K. Arpag, and S. Solomon, Measurements of Arctic sunrise surface ozone depletion events at Kangerlussuaq, Greenland (67 degrees N, to 51 degrees W), *Tellus Series B-Chemical and Physical Meteorology*, *49*(5), 496–509, 1997.

Miller, H. L., R. W. Sanders, and S. Solomon, Observations and interpretation of column OClO seasonal cycles at two polar sites, *Journal of Geophysical Research*, *104*(D15), 18769–18783, 1999.

Molina, M. J., and F. S. Rowland, Stratospheric sink for chlorofluoromethanes: Chlorine atom-catalysed destruction of ozone., *Nature*, *249*, 810–812, 1974.

Molina, M. J., T.-L. Tso, L. T. Molina, and F. C. Y. Wang, Antarctic stratospheric chemistry of chlorine nitrate, hydrogen chloride, and ice: Release of active chlorine., *Science*, *238*, 1253–1257, 1987.

Molina, M. J., R. Zhang, P. J. Wooldridge, J. R. McMahon, J. E. Kim, H. Y. Chang, and K. D. Beyer, Physical-chemistry of the $H_2SO_4/HNO_3/H_2O$ system - implications for polar stratospheric clouds, *Science*, *261*(5127), 1418–1423, 1993.

Montzka, S. A., J. H. Butler, R. C. Myers, T. M. Thompson, T. H. Swanson, A. D. Clarke, L. T. Lock, and J. W. Elkins, Decline in the tropospheric abundance of halogen from halocarbons - implications for stratospheric ozone depletion, *Science*, *272*(5266), 1318–1322, 1996.

Mount, G. H., R. W. Sanders, and J. W. Brault, Interference Effects in Reticon Photodiode Array Detectors, *Applied Optics*, *31*(7), 851–858, 1992.

Mueller, R. W., H. Bovensmann, J. W. Kaiser, A. Richter, A. Rozanov, F. Wittrock, and J. P. Burrows, Consistent interpretation of ground based and GOME BrO slant column data, *Advances in Space Research*, *29*, 1655–1660, 2002.

Murayama, S., T. Nakazawa, and M. Tanaka, Variations of tropospheric ozone concentration over Syowa station, Antarctica, *Tellus Series B-Chemical and Physical Meteorology*, *44*, 262–272, 1992.

NASA-LaRC, SAGE II $NO_2$ profiles were supplied by the NASA Langley Research Center (NASA-LaRC) and the NASA Langley Radiation and Aerosols Branch, 2001-2003.

NDSC, The data used in this publication was obtained as part of the Network for the Detection of Stratospheric Change (NDSC) and is publicly available (see http://www.ndsc.ncep.noaa.gov), 2003.

Nickolaisen, S. L., R. R. Friedl, and S. P. Sander, Kinetics and mechanism of the ClO+ClO reaction: Pressure and temperature dependences of the bimolecular and termolecular channels and thermal decomposition of chlorine peroxide., *Journal of Physical Chemistry*, *98*(1), 155–169, 1994.

Noel, S., H. Bovensmann, J. P. Burrows, J. Frerick, K. V. Chance, and A. H. P. Goede, Global atmospheric monitoring with SCIAMACHY, *Physics and Chemistry of the Earth Part C-Solar-Terrestial and Planetary Science*, *24*(5), 427–434, 1999.

Noxon, J., Nitrogen dioxide in the stratosphere and troposphere measured by ground-based absorption spectroscopy, *Science*, *189*, 547–549, 1975.

Oltmans, S. J., Personal communication. surface ozone data from Arrival Heights (78°S)., 2003.

Oltmans, S. J., and H. Levy, Surface ozone measurements from a global network, *Atmospheric Environment*, *28*(1), 9–24, 1994.

Oltmans, S. J., et al., Trends of ozone in the troposphere, *Geophysical Research Letters*, *25*(2), 139–142, 1998.

O'Sullivan, D., International gathering plans ways to safeguard atmospheric ozone, *Chemical Engineering News*, (June 26), 33–36, 1989.

Otten, C., F. Ferlemann, U. Platt, T. Wagner, and K. Pfeilsticker, Groundbased DOAS UV/visible measurements at Kiruna (Sweden) during the sesame winters 1993/94 and 1994/95, *Journal of Atmospheric Chemistry*, *30*(1), 141–162, 1998.

Perliski, L. M., and S. Solomon, On the evaluation of air mass factors for atmospheric near-ultraviolet and visible absorption spectroscopy., *Journal of Geophysical Research*, *98*(D6), 10363–10374, 1993.

Pfeilsticker, K., et al., Lower stratospheric organic and inorganic bromine budget for the Arctic winter 1998/99, *Geophysical Research Letters*, *27*(20), 3305–3308, 2000.

Platt, U., Differential Optical Absorbtion Spectroscopy (DOAS), in *Air Monitoring By Spectroscopic Techniques*, edited by M. W. Sigrist, vol. 127 of *Chemical Analysis: A Series of Monographs on Analytical Chemistry and its Applications*, pp. 27–76. John Wiley and Sons, Inc., New York, 1994.

Platt, U., Reactive halogen species in the mid-latitude troposphere - Recent discoveries, *Water Air and Soil Pollution*, *123*(1-4), 229–244, 2000.

Preston, K. E., The retrieval of $NO_2$ vertical profiles from ground-based twilight UV-visible absorption measurements, Ph.D. thesis, University of Cambridge, 1995.

Preston, K. E., R. L. Jones, and H. K. Roscoe, Retrieval of $NO_2$ vertical profiles from ground-based UV-visible measurements - method and validation, *Journal of Geophysical Research*, *102*(D15), 19089–19097, 1997.

Rayleigh, L., On the light from the sky, its polarization and colour, *Philosophical Magazine and Journal of Science*, *41*, 107–120, 274–179, 1871.

Renard, J. B., M. Pirre, C. Robert, and D. Huguenin, The possible detection of OBrO in the stratosphere, *Journal of Geophysical Research*, *103*(D19), 25383–25395, 1998.

Richter, A., Personal communication. GOME data for Lauder (45°S) and Arrival Heights (78°S)., 2003.

Richter, A., F. Wittrock, M. Eisinger, and J. P. Burrows, GOME observations of tropospheric BrO in northern hemispheric spring and summer 1997, *Geophysical Research Letters*, *25*(14), 2683–2686, 1998.

Richter, A., F. Wittrock, A. Ladstatter-Weissenmayer, and J. P. Burrows, GOME measurements of stratospheric and tropospheric BrO, *Advances in Space Research*, *29*(11), 1667–1672, 2002.

Rodgers, C. D., Retrieval of atmospheric temperature and composition from remote measurements of thermal radiation, *Reviews of Geophysics and Space Physics*, *14*(4), 609–624, 1976.

Rodgers, C. D., Characterization and error analysis of profiles retrieved from remote sounding measurements, *Journal of Geophysical Research*, *95*(D5), 5587–5595, 1990.

Rodgers, C. D., *Inverse Methods for Atmospheric Sounding, Theory and Practice*, vol. 2 of *Series on Atmospheric, Oceanic and Planetary Physics.* World Scientific Publishing Co. Pte. Ltd., Singapore, 1st edn., 2000.

Russell, P. B., et al., Global to microscale evolution of the pinatubo volcanic aerosol derived from diverse measurements and analyses, *Journal of Geophysical Research*, *101*(D13), 18745–18763, 1996.

Salawitch, R. J., S. C. Wofsy, and M. B. McElroy, Chemistry of OClO in the Antarctic stratosphere: Implications for bromine, *Planetary and Space Science*, *36*(2), 213–224, 1988.

Sander, S. P., et al., Chemical kinetic and photochemical data for use in stratospheric modeling. supplement to evaluation number 12: Update of key reactions. evaluation number 13, Tech. Rep. 13, Jet Propulsion Laboratory, 2000.

Sanders, R. W., S. Solomon, J. P. Smith, L. Perliski, H. L. Miller, G. H. Mount, J. G. Keys, and A. L. Schmeltekopf, Visible and near-ultraviolet spectroscopy at McMurdo station, Antarctica 9. Observations of OClO from April to October 1991, *Journal of Geophysical Research*, *98*(D4), 7219–7228, 1993.

Sarkissian, A., H. K. Roscoe, D. J. Fish, M. Van Roozendael, M. Gil, H. B. Chen, P. Wang, P. Pommereau, J, and J. Lenoble, Ozone and $NO_2$ air-mass factors for zenith-sky spectrometers: Intercomparison of calculations with different radiative transfer models., *Geophysical Research Letters*, *22*(9), 1113–1116, 1995a.

Sarkissian, A., N. K. Roscoe, and D. J. Fish, Ozone measurements by zenith-sky spectrometers - an evaluation of errors in air-mass factors calculated by radiative transfer models, *Journal of Quantitative Spectroscopy and Radiative Transfer*, *54*(3), 471–480, 1995b.

Schauffler, S. M., L. E. Heidt, W. H. Pollock, T. M. Gilpin, J. F. Vedder, S. Solomon, R. A. Lued, and E. L. Atlas, Measurements of halogentated organic compounds near the tropical tropopause., *Geophysical Research Letters*, *20*(22), 2567–2570, 1993.

Schauffler, S. M., E. L. Atlas, F. Flocke, R. A. Lueb, V. Stroud, and W. Travnicek, Measurements of bromine containing organic compounds at the tropical tropopause, *Geophysical Research Letters*, *25*(3), 317–320, 1998.

Schauffler, S. M., E. L. Atlas, D. R. Blake, F. Flocke, R. A. Lueb, J. M. Lee-Taylor, V. Stroud, and W. Travnicek, Distributions of brominated organic compounds in the troposphere and lower stratosphere, *Journal of Geophysical Research*, *104*(D17), 21513–21535, 1999.

Schiff, H. I., Neutral reactions involving oxygen and nitrogen, *Canadian Journal of Chemistry.*, *47*, 1903–1916, 1969.

Schofield, R., B. J. Connor, K. Kreher, P. V. Johnston, and C. D. Rodgers, The retrieval of profile and chemical information from ground-based UV-visible spectroscopic measurements, *Journal of Quantitative Spectroscopy and Radiative Transfer*, in press, 2003.

Schroeder, W. H., and J. Munthe, Atmospheric mercury - an overview, *Atmospheric Environment*, *32*(5), 809–822, 1998.

Schroeder, W. H., K. G. Anlauf, L. A. Barrie, J. Y. Lu, A. Steffen, D. R. Schneeberger, and T. Berg, Arctic springtime depletion of mercury, *Nature*, *394*(6691), 331–332, 1998.

Sinnhuber, B. M., BrO photochemistry and impact on ozone destruction, in *Final report - Part A: Integrated report*. Programme Environment and Climate 1994 - 1998, Area 1.2.1.1. Stratospheric chemicstry and the depletion of the ozone layer, 2000.

Sinnhuber, B. M., et al., Comparison of measurements and model calculations of stratospheric bromine monoxide, *Journal of Geophysical Research*, *107*(D19), doi:10.1029/2001JD000940, 2002.

Solberg, S., N. Schmidbauer, A. Semb, F. Stordal, and O. Hov, Boundary-layer ozone depletion as seen in the Norwegian Arctic in spring, *Journal of Atmospheric Chemistry*, *23*(3), 301–332, 1996.

Solomon, S., Essay: Ozone depletion: From pole to pole, *Atmospheric Chemistry and Global Change.*, pp. 513–514, 1999a.

Solomon, S., Stratospheric ozone depletion: A review of concepts and history, *Reviews of Geophysics.*, *37*(3), 275–316, 1999b.

Solomon, S., A. L. Schmeltekopf, and R. W. Sanders, On the interpretation of zenith sky absorption measurements, *Journal of Geophysical Research*, *92*(D7), 8311–8319, 1987.

Solomon, S., R. W. Sanders, M. A. Carroll, and A. L. Schmeltekopf, Visible and near-ultraviolet spectroscopy at McMurdo station, Antarctica. 5. Observations of the diurnal variations of BrO and OClO., *Journal of Geophysical Research*, *94*(D9), 11393–11403, 1989.

Solomon, S., R. R. Garcia, and A. R. Ravishankara, On the role of iodine in ozone depletion, *Journal of Geophysical Research*, *99*(D10), 20491–20499, 1994.

Sprovieri, F., N. Pirrone, I. M. Hedgecock, M. S. Landis, and R. K. Stevens, Intensive atmospheric mercury measurements at Terra Nova bay in Antarctica during november and december 2000, *Journal of Geophysical Research*, *107*(D23), doi:10.1029/2002JD002057, 2002.

Spurr, R. J. D., T. P. Kurosu, and K. V. Chance, A linearized discrete ordinate radiative transfer model for atmospheric remote-sensing retrieval, *Journal of Quantitative Spectroscopy and Radiative Transfer*, *68*(6), 689–735, 2001.

Staehelin, J., A. Renaud, J. Bader, R. McPeters, P. Viatte, B. Hoegger, V. Bugnion, M. Giroud, and H. Schill, Total ozone series at Arosa (Switzerland) - homogenization and data comparison, *Journal of Geophysical Research*, *103*(D5), 5827–5841, 1998a.

Staehelin, J., R. Kegel, and N. R. P. Harris, Trend analysis of the homogenized total ozone series of Arosa (Switzerland), 1926-1996, *Journal of Geophysical Research*, *103*(D7), 8389–8399, 1998b.

Stam, D. M., I. Aben, and F. Helderman, Skylight polarization spectra: Numerical simulation of the Ring effect, *Journal of Geophysical Research*, *107*(D20), art. no.–4419, 2002.

Stamnes, K., S. C. Tsay, W. Wiscombe, and K. Jayaweera, Numerically stable algorithm for discrete-ordinate-method radiative-transfer in multiple-scattering and emitting layered media, *Applied Optics*, *27*(12), 2502–2509, 1988.

Struthers, H. A., Personal communication. Stationary runs were conducted for Lauder, and Arrival Heights, 2003.

Sturges, W. T., C. W. Sullivan, R. Schnell, L. E. Heidt, and W. Pollock, Bromoalkane production by Antarctic ice algae, *Tellus Series B-Chemical and Physical Meteorology*, *45*, 120–126, 1993.

Sturges, W. T., D. E. Oram, L. J. Carpenter, S. A. Penkett, and A. Engel, Bromoform as a source of stratospheric bromine, *Geophysical Research Letters*, *27*(14), 2081–2084, 2000.

Stutz, J., and U. Platt, Numerical analysis and estimation of the statistical error of Differential Optical Absorption Spectroscopy measurements with least-squares methods, *Applied Optics*, *35*(30), 6041–6053, 1996.

Stutz, J., R. Ackermann, J. D. Fast, and L. Barrie, Atmospheric reactive chlorine and bromine at the Great Salt Lake, Utah, *Geophysical Research Letters*, *29*(10), doi:10.1029/2002GL014812, 2002.

Tang, T., and J. C. McConnell, Autocatalytic release of bromine from Arctic snow pack during polar sunrise, *Geophysical Research Letters*, *23*(19), 2633–2636, 1996.

Tarasick, D. W., and J. W. Bottenheim, Surface ozone depletion episodes in the Arctic and Antarctic from historical ozonesonde records, *Atmospheric Chemistry and Physics*, *2*, 197–205, 2002.

Tie, X. X., and G. Brasseur, The response of stratospheric ozone to volcanic eruptions - sensitivity to atmospheric chlorine loading, *Geophysical Research Letters*, *22*(22), 3035–3038, 1995.

Tie, X. X., and G. Brasseur, The importance of heterogeneous bromine chemistry in the lower stratosphere, *Geophysical Research Letters*, *23*(18), 2505–2508, 1996.

Tisdale, R. T., A. M. Middlebrook, A. J. Prenni, and M. A. Tolbert, Crystallization kinetics of $HNO_3/H_2O$ films representative of polar stratospheric clouds, *Journal of Physical Chemistry*, *101*(11), 2112–2119, 1997.

Toublanc, C., Henyey-Greenstein and Mie phase functions in monte carlo radiative transfer computations, *Applied Optics*, *35*(18), 3270–3274, 1996.

Tuckermann, M., R. Ackermann, C. Golz, H. Lorenzenschmidt, T. Senne, J. Stutz, B. Trost, W. Unold, and U. Platt, DOAS-observation of halogen radical-catalysed Arctic boundary layer ozone destruction during the ARCTOC-campaigns 1995 and 1996 in Ny-Ålesund, Spitsbergen, *Tellus Series B-Chemical and Physical Meteorology*, *49*(5), 533–555, 1997.

Van der Leun, J., X. Tang, and M. Tevini, Environmental effects of ozone depletion: 1994 assessment., *Ambio*, *XXIV*(3), 138–196, 1995.

Van Roozendael, M., et al., Lessons learned from 2 years of coordinated multi-platform UV-visible observations of atmospheric bromine monoxide., *Proceedings of the QOS 2000 Symposium.*, pp. 157–384, 2000.

Van Roozendael, M., et al., Intercomparison of BrO measurements from ERS-2 GOME, ground-based and balloon platforms, *Advances in Space Research*, *29*(11), 1661–1666, 2002.

Vogt, R., P. J. Crutzen, and R. Sander, A mechanism for halogen release from sea-salt aerosol in the remote marine boundary layer, *Nature*, *383*(6598), 327–330, 1996.

Wagner, T., Satellite observations of atmospheric halogen oxides, Ph.D. thesis, Ruperta Calrola University, 1999.

Wagner, T., and U. Platt, Satellite mapping of enhanced BrO concentrations in the troposphere, *Nature*, *395*(6701), 486–490, 1998.

Wahner, A., A. R. Ravishankara, S. P. Sander, and R. R. Friedl, Absorption cross section of BrO between 312 and 385 nm at 298 and 223 K, *Chemical Physics Letters*, *152*(6), 507–512, 1988.

Wahner, A., R. O. Jakoubek, G. H. Mount, A. R. Ravishankara, and A. L. Schmeltekopf, Remote sensing observations of nighttime OClO column during the airborne Antarctic ozone experiment, September 8, 1987, *Journal of Geophysical Research*, *94*(D9), 11405–11411, 1989.

Wallace, J. M., and P. V. Hobbs, *Atmospheric Science An Introductory Survey*. Academic Press, Inc., Orlando, Florida, 1977.

Wamsley, P. R., et al., Distribution of halon-1211 in the upper troposphere and lower stratosphere and the 1994 total bromine budget, *Journal of Geophysical Research*, *103*(D1), 1513–1526, 1998.

Wayne, R. P., *Chemistry of Atmospheres. An Introduction to the Chemistry of the Atmospheres of Earth, the Planets, and their Satellites*. Clarendon Press, Oxford, 2nd edn., 1991.

Wilmouth, D. M., T. F. Hanisco, N. M. Donahue, and J. G. Anderson, Fourier transform ultraviolet spectroscopy of the A $^2\Pi_{2/3} \leftarrow$ X $^2\Pi_{2/3}$ transition of BrO, *Journal of Physical Chemistry A*, *103*(45), 8935–8945, 1999.

Wiscombe, W. J., R. M. Welch, and W. Hall, The effects of very large drops on clouds absorption. Part I: Parcel models, *Journal of Atmospheric Science*, *41*, 1338–1355, 1984.

WMO, Scientific assessment of ozone depletion: 2002, Global ozone research and monitoring project - Report No. 47, 498 pp., Geneva, 2003.

Wofsy, S. C., M. B. McElroy, and Y. L. Yung, The chemistry of atmospheric bromine, *Geophysical Research Letters*, *2*(6), 215–218, 1975.

Yung, Y. L., J. P. Pinto, R. T. Watson, and S. P. Sander, Atmospheric bromine and ozone perturbations in the lower stratosphere., *Journal of the Atmospheric Sciences*, *37*, 339–353, 1980.

# Index